UNIVERSITY OF OKLAHOMA

GRADUATE COLLEGE

QUANTIFICATION OF RECOVERY FACTORS IN DOWNSPACED SHALE WELLS

A THESIS

SUBMITTED TO THE GRADUATE FACULTY

in partial fulfillment of the requirements for the

Degree of

MASTER OF SCIENCE

By

SAURABH SINHA
Norman, Oklahoma
2016

QUANTIFICATION OF RECOVERY FACTORS IN DOWNSPACED SHALE WELLS

A THESIS APPROVED FOR THE
MEWBOURNE SCHOOL OF PETROLEUM AND GEOLOGICAL ENGINEERING

BY

_____
Dr. Deepak Devegowda, Chair

_____
Dr. Matthew J. Pranter

_____
Dr. Mashhad Fahes

To my parents, Leela and Rakesh, without their constant dedication towards my education over 25 long years it will not be possible for me to write this thesis today.

Acknowledgements

I would like to express my deepest gratitude to my advisor Dr. Deepak Devegowda for his full support and guidance throughout my study and research. I would also like to thank my thesis committee members Dr. Matthew Pranter and Dr. Mashhad Fahes for their valuable suggestions and constantly guiding me towards the right direction.

I would also like to extend my gratitude to Bhabesh Deka for his technical support for the project.

Last but not the least I would like to thank Yuliana Zapata and Javier Tellez for their help and support which made this thesis possible.

Table of Contents

List of Tables

List of Figures

Abstract

Well spacing optimization in horizontal multi-fractured wells is the center of field development. Unconventional reservoirs due to the low matrix permeability cannot produce without the help of hydraulic fracturing. Unlike the conventional reservoir where all wells draw production from a connected reservoir, an unconventional reservoir acts as an isolated reservoir for each well bounded by the transverse fracture tips.

As there is no contribution beyond the fracture tips, the best way to produce from an unconventional reservoir to place the wells close enough that no portion of the reservoir remains undrained. This optimal well spacing can be quantified in terms of recovery factor for each well. Hence to exploit the field optimally, the recovery factors needs to be maximized. But, beyond a certain well spacing placing wells further close to each other may lead to well interference and a reduction in recovery factors. This thesis seeks to find a robust well spacing workflow for unconventional reservoirs by integrating data from multiple data sources. The study area in this thesis is the rich condensate portion of Eagle Ford shale. Eagle Ford shale in this area provides maximum value for the operators due to high condensate recovery factors.

The total Eagle Ford thickness in the area of interest varies from 200-250 ft. The different sequences can be identified on the well logs in this area as: upper, middle and lower Eagle Ford. Rock typing in this area suggests 4 different rock types that could be production drivers in Eagle Ford. A 3-D lithological model is generated from well logs shows that the upper and middle Eagle Ford consists of small scale heterogeneities distributed all across the reservoir. Lower Eagle Ford however, is a more uniform and

continuous interval. From 3D model, lithology constrained porosity and water saturation show that the lower Eagle Ford comprises of high porosity and low water saturation.

Microseismic data from a PAD well is used to generate fracture networks and hence the stimulated reservoir rock volume (SRV). Microseismic data shows the growth of the fracture network and drainage areas are irregular and full 500 ft. spacing between the wells is not drained. The same is also verified after matching the historical production data.

Well spacing sensitivities on the history matched model show that 420 ft. well spacing is optimal in this area. To verify the simulation results a multivariate statistical analysis is performed on Arp's decline parameters i.e. initial production, decline and b factor on more than 1500 wells. The regression model suggests the optimal well spacing to be 400 ft. The statistical analysis hence verified the simulation results and further bolstered the conclusion that 400-420 ft. well spacing is optimal in rich condensate area of Eagle Ford shale.

1. Introduction

1.1.Problem Statement

Shale oil/gas in recent years has changed the world energy arena. Completion optimization (CO) coupled with massive hydraulic fracturing (MHF) play a key role in producing from these reservoirs.

Unlike the conventional reservoirs, shale reservoir exhibits unique features such as ultra-low permeability, hence making MHF a necessary condition to produce from these reservoirs. As the recovery in these reservoirs is dependent on flow from the fractured reservoir volume, correct estimation of stimulated reservoir rock volume (SRV) is critical (Zhang, Holland, van der Zee, & Moos, 2014).

Based on the SRV operators decide the well spacing between the wells. Incorrect estimation of SRV and hence the production from these reservoirs may lead the operator to either put the wells too far apart or place the well too close to each other.

The first scenario leads to inefficient drainage of the reservoir leaving undrained oil and gas behind. The second scenario leads to well interference leading to much less expected ultimate recovery (EUR) from each well thus decreasing the project valuation(Ri et al., 2011;Ajani and Kelkar, 2012).

1.2.Objective

The objective of this thesis is to quantify the recovery factor in the wells at different well spacing's. A three-pronged approach is adopted in this thesis to quantify the recovery factors. First is the conventional analytical models and rate transient analysis (RTA), second is reservoir simulation and the third part includes a statistical validation of results.

Data such as well logs, microseismic and composition of the reservoir fluid is incorporated in the study to characterize the reservoir and fluid properties. All data used in the study provided by a major operator in Eagle Ford Shale(EFS).

For the purpose of the study, it is assumed that a conventional reservoir simulator is sufficient to model the fluid flow i.e. Darcy's law with appropriate corrections for the non-Darcy flow (Zeng & Grigg, 2006) sufficiently models the fluid flow in the reservoir.

2. Analytical Methods

2.1. Literature Review

Analytical models in recent past have gained popularity due to inability of decline curve analysis (DCA) alone to predict the EUR's on many occasions. Analytical methods provide a mid-way between the oversimplified DCA's and over complicated numerical simulation techniques. In this chapter, a detailed account on both decline curve analysis and analytical models is provided.

Although the chapter is dedicated to analytical methods, DCA is a direct alternative to analytical methods and hence it is discussed here. DCA is also the method to forecast the EUR's in the statistical section (chapter 4) and analysis here lay the foundation for it. Originally developed by Arps (1944), DCA still is the most common method to forecast the reserves. Due to number of wells present in an unconventional asset portfolio, it is possibly the easiest method that can be applied on a well by well basis for the purpose of reserve reporting. The original equation can be summarized in a general hyperbolic form as:

$$q = q_i \frac{1}{(1 + bD_i\, t)^{1/b}} \tag{2.1}$$

Where, $q$is the production rate at time t (volume/time), $q_i$is the production rate at time zero (volume/time), b is the Arp's hyperbolic decline constant ($0 < b < 1$), D_i is Arp's initial decline rate (1/time) and t is time. The process of decline analysis consists of best fitting of the production decline trend by using three parameters (Initial production, decline and b factor) on the available production data. It then uses the

hyperbolic decline equation (equation 2.1) to forecast the production in future (Arps, 1944). Later, Fetkovich et al. (1996) described the exponential and harmonic declines forms of the equation with b values of 0 and 1 respectively.

There is certain criterion which must be fulfilled before applying decline curve analysis. Lee et al. (2010) have summarized these criterion as:

(a) The analysis is valid only for constant flowing bottom hole pressure (FBHP) conditions

(b) Stabilized flow in reservoir. In case of horizontal well with transverse fractures, stabilized flow can be seen as boundary dominated flow (BDF) or fracture interference.

(c) A fixed drainage area

(d) Unchanging skin factor

For ultra-low permeability reservoirs like shales, most of these assumptions are not valid and more often we see a best fit of the data can be obtained only by using a b factor more than 1. There are multiple reasons for this, including but not limited to the fact that reaching a stabilize flow in these reservoirs can take several years and hence in absence of a stabilized flow a constant bottom hole pressure does not exist.

Also, the operational conditions such as choke management in these wells prolong the times to see the decline, making it impossible to get a good fit on a data with conventional Arp's value.

Direct consequence of using a b value greater or equal to 1 in Arp's hyperbolic declines is the infinite cumulative volumes and hence the EUR is unbound. i.e. as the production time tends to infinity the EUR tends to infinity (Lee et al., 2010).

Different operators use different methodologies to constraint the EUR. One way to accomplish this is to use the terminal declines in the forecasting process or to just use a limiting value of the rates after which economics does not justify production rates (Lee et al., 2010;Folladori, 2014;SPE PRMS, 2007).

Other methods to bound the EUR's includes using stretched exponential declines, Duong decline curves, multi segment declines etc. (Freeborn & Russell, 2012).

However, if appropriate methodology is not applied, this can still lead to reserve overestimation (Okouma Mangha et al., 2012). The so called "best engineering judgement" or simply the best guess of declines leave a lot of uncertainty in the calculation of EUR. A rather more recent method tries to address this problem. Pressure normalized rate or PNR (Lacayo & Lee, 2014). PNR utilizes drawdown normalized rates instead rate, on a conventional rate-time decline plot. This method is very successful in dry gas reservoirs but not very accurate for other fluid types.

2.2. Methodology for Decline Curve Analysis

The workflow followed in this thesis for decline fitting of the data is summarized in Figure 2.1. shows that before using the decline curve analysis (DCA) it is important to identify the flow regimes in the well. If the well is in boundary dominated flow, then only it can be used to forecast the expected ultimate recovery (EUR) from these wells. It also shows that if there is any operation change in the well such as artificial lift installation or re-fracturing, the portion of the well history which best represents the decline behavior should be used for forecasting.

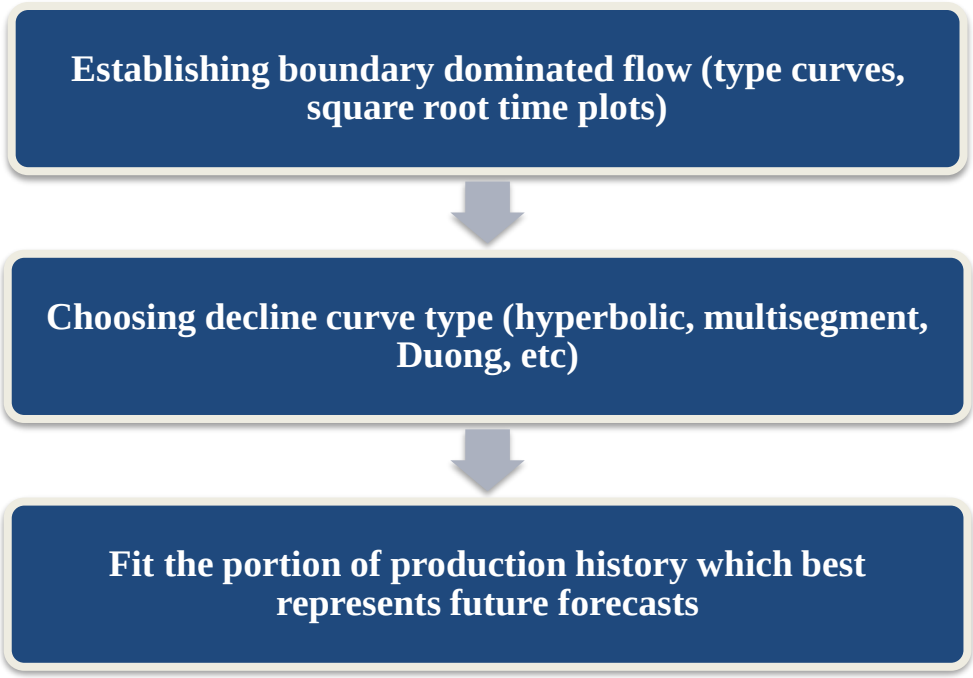

Figure 2.1. Flowchart demonstrating the process used in fitting the decline trends. Before using decline curve analysis, it is important to identify the flow regime in the wells. Multiple methods can be used to identify and confirm the flow regime in the well such as square root time plot or type curves. The choice of decline fit model depends on the user depending upon which method best represents decline trends in a field by constraining the EUR's within reasonable limits.

2.3. Methodology for Rate Transient Analysis

2.3.1. Overview of Rate Transient Analysis

An alternative of decline analysis is analytical mathematical models which are now standard in many rate transient analysis (RTA) software's. The analysis procedure includes a simultaneous match on rates transients and pressures (Ekaterina Stalgorova & Mattar, 2013).

The model utilizes the rate transient analysis plots to initialize a mathematical model such as horizontal well multi fracture composite (Brown, Ozkan, Raghavan, & Retired, 2011), horizontal multi fracture SRV with equal fracture half lengths (Ekaterina Stalgorova & Mattar, 2013) , horizontal multi fracture model with enhanced fracture

regions (E Stalgorova & Mattar, 2012) etc. A set of parameters can be set as history matching parameters in a reasonable range (more like “goal and seek”) to get a match. A forecast is then made on the history matched data.

The most important part in analytical models is the initialization of the model using the linear flow analysis (LFA) or rate transient analysis (RTA). Linear flow analysis as discussed by El-Banbi and Wattenbarger (1995). The methodology includes a combination of type curves, diagnostic plots, flowing material balance (FMB) plot and forecast plots. The process starts with identifying the flow regimes in the well. This can be established using type curves (Figure 2.7). Type curves are generally indicative of flow regimes and further confirmation can be obtained via square root time plots (Figure 2.9).

To initialize any kind of analytical model seed values for SRV geometry such as fracture half lengths, lateral lengths etc. are required (M. Nobakht, Ambrose, Clarkson, Youngblood, & Adams, 2013). To further fine tune and match the production data other reservoir characteristics important to fluid flow such as permeability, skin factor, fracture conductivity etc. are also required (Morteza Nobakht, Associates, & Clarkson, 2012).To derive these parameters a combination of flowing material balance (FMB) and square root time plot are used in this study.

Material balance, essentially mass balance are still used as a reliable conventional oil and gas resource estimation method (Hurst, 1973). Conventional material balance can only be applied to wells in pseudo steady state (Hurst, 1973). The method used in this thesis is the Agarwal Gardner (McNeil & Mattar, 1995) flowing material balance or FMB. FMB utilizes a cross plot of normalized rate and normalized cumulative. Extrapolation of this curve when well has achieved stabilized flow, provides an estimate of original gas

in place (OGIP). In absence of a stabilized flow, the curve can be extrapolated to determine contacted gas in place (CGIP) until the available production data.

In this study, the reservoir fluid is a retrograde gas condensate. As the in place fluid is gas following corrections are applied to best represent the fluid properties. All rates used are calculated by mixing the surface oil into gas (recombination) to obtain equivalent downhole gas rates. In retrograde gas condensate systems, the condensation takes place both at surface and downhole. Before the bubble point pressure, the condensation usually takes place at the surface. Hence, although the reservoir fluid is single phase gas inside the reservoir, at surface both oil and gas is obtained. To do any analysis at downhole conditions it is necessary to obtain an equivalent single phase downhole gas.

The following method described by (Imo-jack, 2010) is used to recombine the surface oil into gas phase. Using the separator pressure, separator temperature, specific gravity of primary separator gas and API gravity of stock tank oil the equivalent gas for the oil phase is calculated as:

$$V_{eq} = 635.53 + 0.36182p^{1.0544}\, G^{5.0831}\, \gamma^{1.5812}\, T^{-0.79130} \qquad (2.2)$$

Where, G is the specific gravity of primary separator gas, P is the separator pressure (Psia), T is the separator temperature (degree F), γ is the API gravity of stock tank condensate and V_{eq} is the equivalent gas volume. The recombined gas rate is then given as,

$$q_{Recombined} = q_{measured}\ \left(1 + \frac{V_{eq}}{10^6} * CGR\right) \qquad (2.3)$$

Where, $q_{recombined}$ is the recombined gas rate, $q_{measured}$ is the measured gas rate, CGR is the condensate gas ratio (bbl/MMSCF).

All pressures are converted into pseudo pressures as pseudo pressures are more reliable to calculate pressure drops in gas (Al-Hussainy et al., 1965). Use of material balance via Agarwal Gardner (Mattar & McNeil, 1998) method to approximate OGIP is elaborated in Figure 2.8.

The productivity index (PI) is also plotted along with the FMB plot. For a deep reservoir like EFS, the geomechanics effects are significant (Sone, 2012). Although, an elaborate geomechanics model is not coupled with analytical models in this study a correlation (Yilmaz and Noor) is used to adjust for the geomechanical effects.

The productivity index (PI) trend can also be used to establish the boundary dominated flow (BDF). For BDF which is fracture interference in our case, the PI should stabilize as rate transient reaches the flow boundary. If PI's are not stabilized the flowing material balance (FMB) cannot be used to predict the OGIP's, but gas volume so far contacted by the rate transient or contacted gas in place (CGIP).

Once, a trend is fitted on FMB and PI, a square root time plot is utilized to identify the flow regimes in the well. The major flow regimes encountered in a horizontal well with multiple transverse fractures is: bi-linear/ linear and boundary dominated (Callard, 2015). A detailed account of LFA is summarized by Wattenbarger and Banbi (Wattenbarger et al., 1998;El-Banbi and Wattenbarger, 1995).

2.3.2. Linear Flow Analysis

In essence LFA utilizes the linear flow equation (Equation 2.4) to identify the end of linear flow on a rate transient and into boundary dominated flow. The slope (Equation 2.5) is an indicative of permeability and fracture half lengths and intercept (Equation 2.6) is indicative of skin (or fracture conductivity in case of finite conductivity fractures). Using the SRV and fracture geometry (Figure 2.2, Figure 2.3 and Figure 2.4) and an assumption of constant FBHP, the end of linear flow period (t_{elf}) can be used to calculate $AcK^{1/2}$ (Equation 2.5). Combining this analysis with FMB (for OGIP) and using the geometry, the terms ($AcK^{1/2}$) can be resolved into fracture half lengths and permeability.

$$\frac{1}{q} = m\sqrt{t} + b' \tag{2.4}$$

$$m = \frac{315.4\,T}{h\sqrt{(\theta \mu_g C_t) i}} \times \frac{1}{P_i - P_{wf}} \times \frac{1}{X_f\sqrt{k}} \tag{2.5}$$

$$F'_{CD} = \frac{141.2\,B\mu}{b'(P_i - P_{Wf)}\ khn_f} \times \left[1 + \frac{h}{x_f}\left(ln\left(\frac{h}{2r_w}\right) - \frac{\pi}{2}\right)\right] \tag{2.6}$$

$$A_c = 2hL_e \tag{2.7}$$

Where, q is the flow rate, t is the time to production, b' is the intercept, h is the net pay thickness, μ_g is the gas viscosity, m is the intercept, Pi is the initial reservoir pressure, pseudo pressure in case of gas, P_{wf} is the flowing bottomhole pressure, pseudo pressure in case of gas, C_t is the total compressibility, X_f is the fracture half length, K is the matrix permeability, F_{CD}' is the dimensionless fracture conductivity, Nf is the number of fractures, and r_w is the wellbore radius.

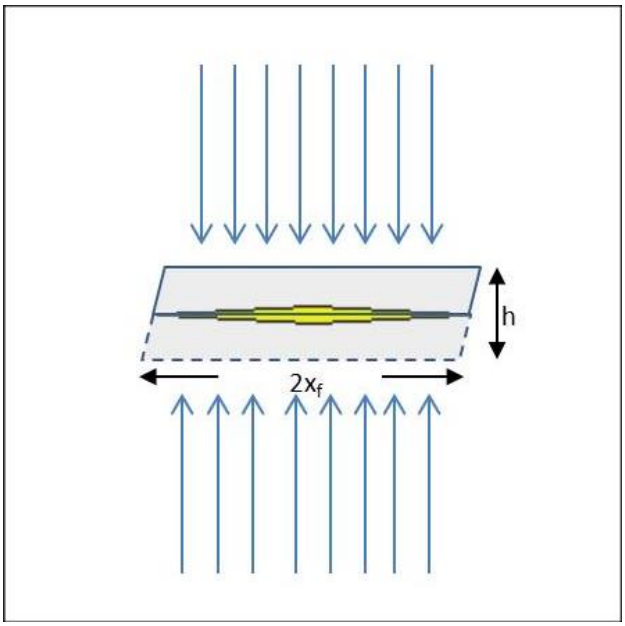

Figure 2.2. Fracture geometry used in the analysis and the nomenclature. X_f is the fracture half-length and h is the fracture height. (Liang et al., 2012). The model assumes a wellbore with transverse fractures of same fracture half lengths.

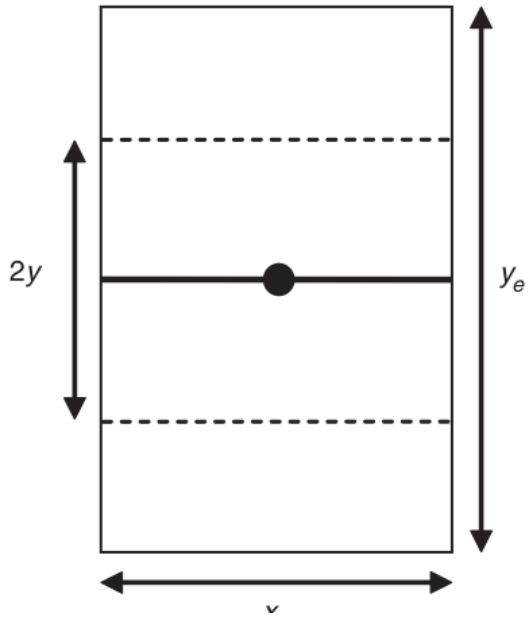

Figure 2.3. Fracture geometry (top view). Y_e is the well perforated lateral is the length of the reservoir and $X_e = 2 \times X_f$ is the width of the reservoir. (Morteza Nobakht et al., 2012).

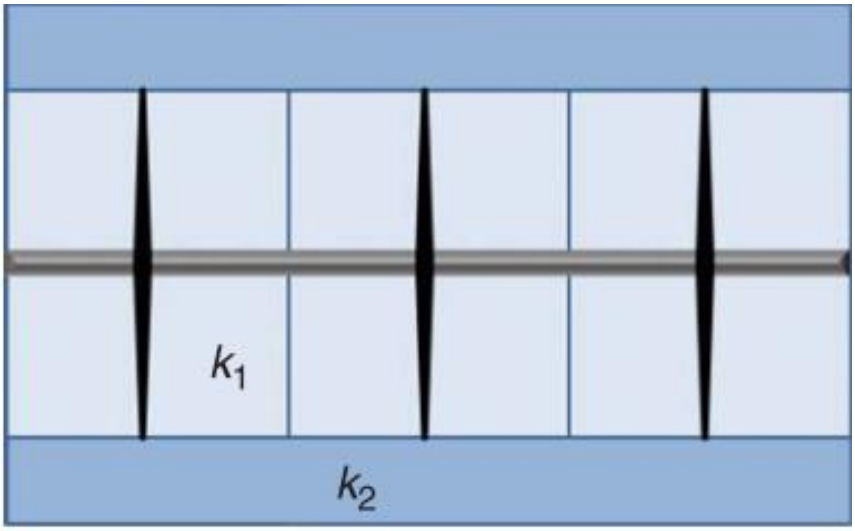

Figure 2.4. Rectangular reservoir with multiple transverse fractures (Ekaterina Stalgorova & Mattar, 2013). The figure shows the permeability's inside and outside the SRV. K1 is the permeability inside SRV which is enhanced due to hydraulic fracturing and K2 is the permeability outside SRV. Fractures are shown in solid black. Due to ultra-low permeability of shales there is little to no contribution outside SRV.

2.3.3. Workflow for Rate Transient Analysis

The workflow adopted in this for RTA is summarized in

Figure 2.5. The process includes using petrophysical data (from well logs) to initialize the analysis. The production data (both rates and pressures) is used for LFA as discussed in section 2.3.2. The RTA is then performed along with LFA and forecast plots.

In theory, the process may yield non-unique results if more than one history matching parameter is used. However, for experienced reservoir engineers familiar with the range of parameters like porosity, fracture half lengths, permeability's etc. derived from other sources such as well logs, microseismic, tracer data, interference tests etc. it can bound the EUR's within reasonable limits with more confidence.

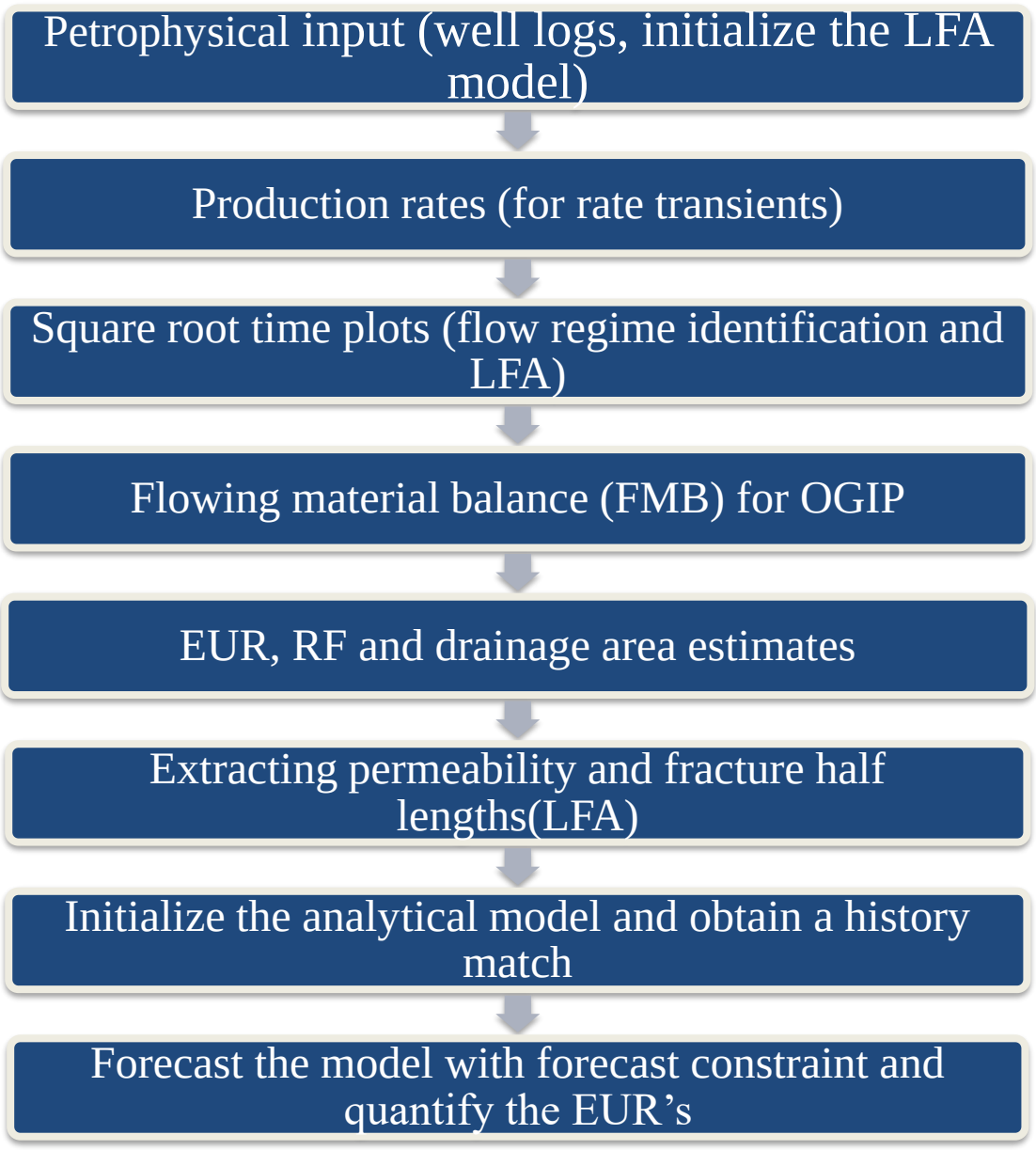

Figure 2.5. Workflow followed for RTA. First step is to calculate the pay from well logs followed by rate transient analysis. Flowing material balance(FMB) is used to calculate OGIP. With OGIP from FMB and assumed geometry of uniform transverse fractures, EUR, fracture half length, permeability and recovery factors are calculated. These base values are used to initialize analytical models and get a history match.

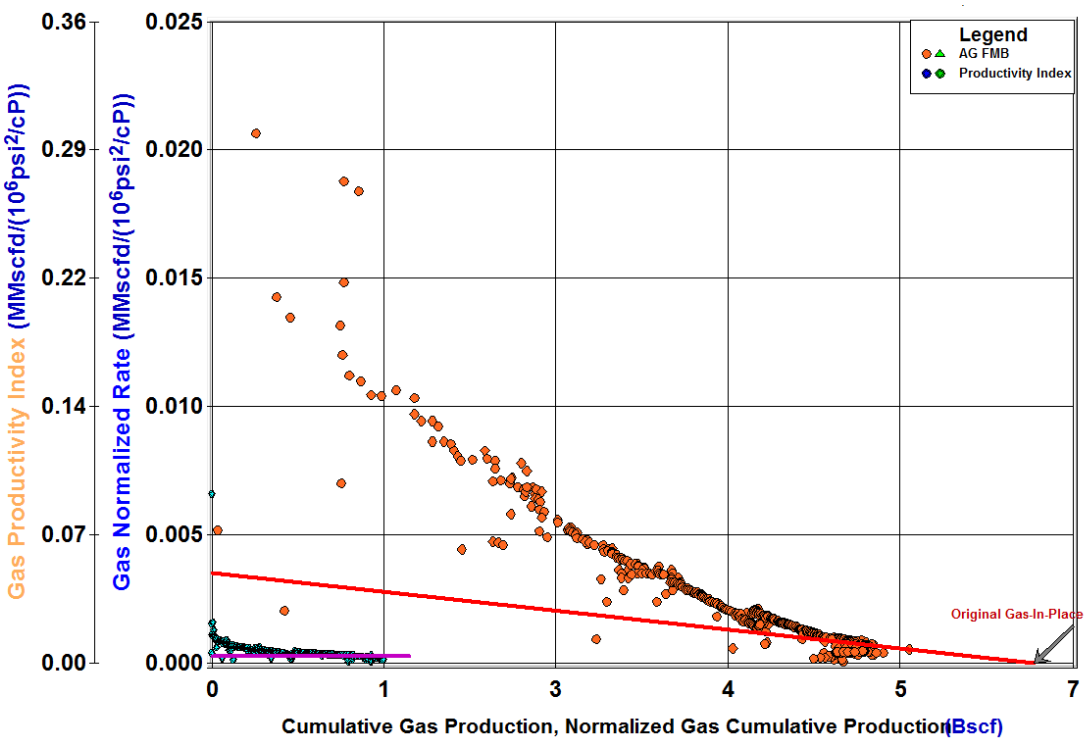

Figure 2.6. Flowing material balance and productivity index for well 2. Flowing material balance (in orange) shows a well-developed trend which can be used to extrapolate OGIP. Calculated OGIP is shown by green arrow on the right. OGIP is about 6.8 BSCF. The productivity index (in cyan) shows that the productivity index is stabilized. This is an additional confirmation in addition to type curves and square root time plots that the well is in BDF.

2.4. Results

The following sections of this chapter describe the application of DCA, analytical models and the reserves estimate comparisons between the two. Later, the corollaries are derived from the results and interpreted with respect to well spacing's.

2.4.1. Decline Curve Analysis

In this study three wells are considered for the decline analysis. The decline is fitted by using an industry standard software FEKETE HARMONY ®. Decline analysis is performed on rate time and rate cumulative plots. First step in decline fitting is to establish the wells that are in boundary dominated flow. This is accomplished by using type curves and square root time diagnostic plot. Figure 2.7 show an example normalized pressure integral (NPI) type curve (Blasingame et al.,1989) for well1 indicating it is in BDF. Red part of the type curve indicates the boundary dominated stem. Same can be seen on the beta derivative plot where beta derivative is 1.

Figure 2.8 is the square root time plot for the same well where rate normalized pseudo pressure is plotted against square root of time. The initial flow is linear as the data falls on the half slope line. Half slope line is shown in marron on the plot. After ~ 70 days' wells shift to a boundary dominated flow. The end of half slope line(t_{elf}) is shown by a solid blue line in the figure.

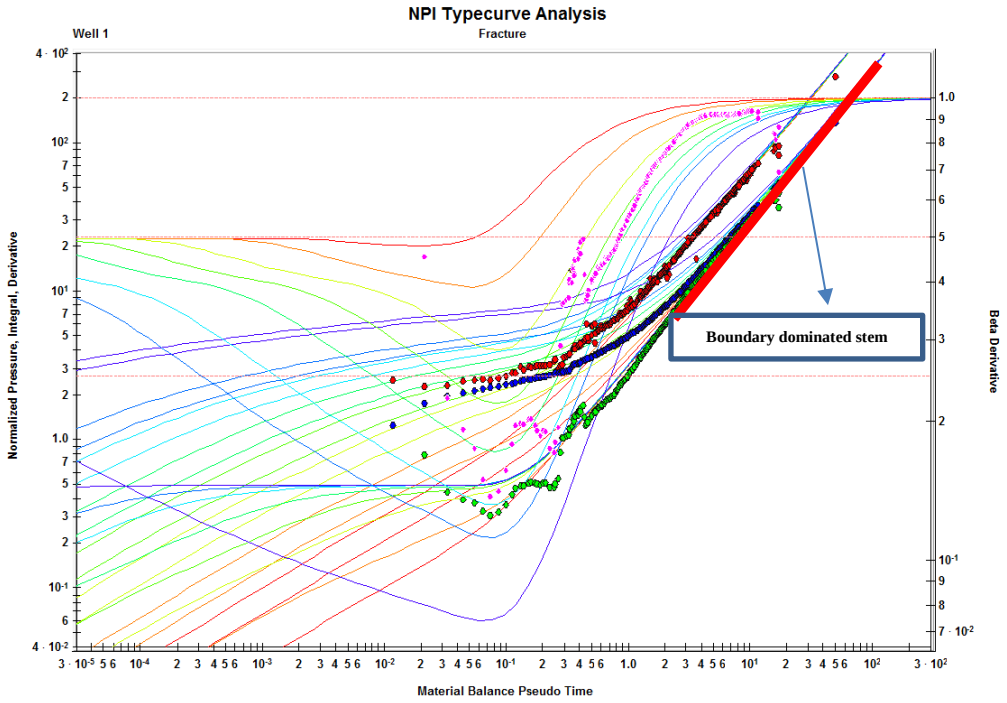

Figure 2.7. NPI type curve analysis (well 1) along with beta derivatives. Well in BDF. Pressure integrals are used to reduce noise in the dataset. Analysis indicates the well is in boundary dominated flow. Discontinuous curve represents the actual dataset while the continuous curves indicate the type curves. It can be seen that the well has moved from the initial transient stem of the type curves to the boundary dominated stem (shown in red).

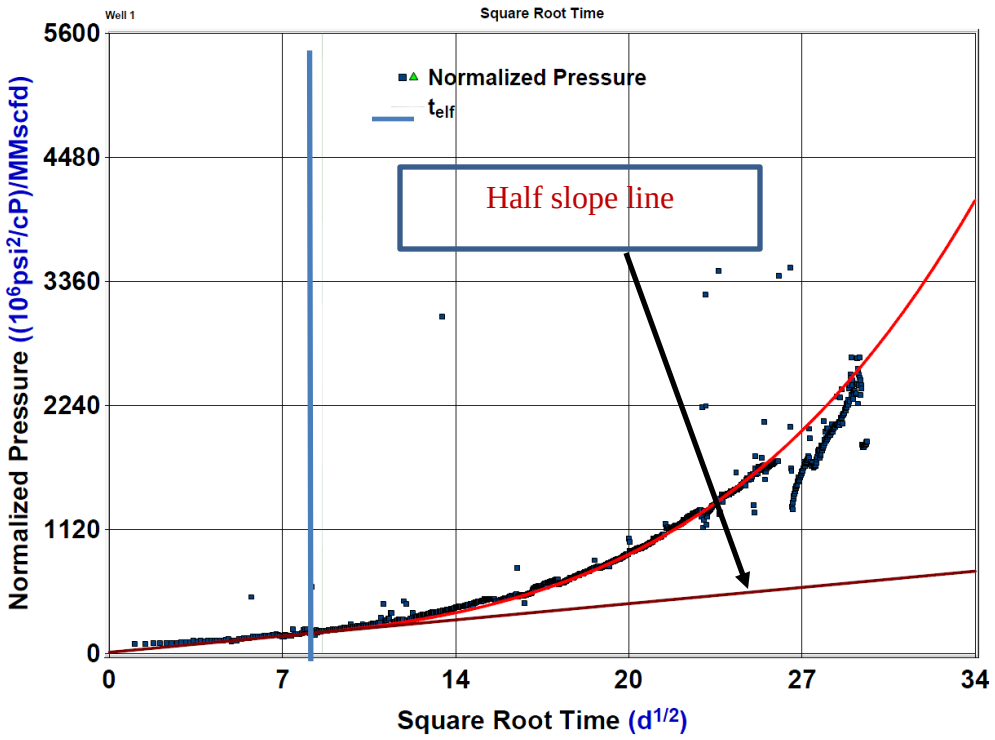

Figure 2.8. Square root time plot (well 1). On X axis is the square root of time and on Y axis is the rate normalized pseudo pressure. Time end of linear flow is determined from the deviation from linear flow behavior. The marron trend is the half slope line of the linear flow. Clearly, the well has gone from linear flow to boundary dominated flow. Blue line is time end of linear flow (~70 days). Red curve shows the overall data trend and the dataset is shown by dotted black lines.

Declines are then fitted on gas phase which is the major phase. An example fit for well 1 (single b, rate cumulative) plot is summarized in Figure 2.9. In figure 2.9 a best fit is obtained on rate-cumulative decline analysis on the gas phase of well 1. Forecast is made after the production history. The EUR is bounded by setting a limit on gas production, which in this case is 1 MSCF/D.

Table 2.1 summarizes the overall DCA EUR comparison. In general, both the rate – time and rate cumulative plots are optimistic. Duong decline analysis and stretched exponential decline analysis yields pessimistic EUR's. Multi segment decline analysis is

performed by using two different b factors in two different flow regimes. A b factor of 2 is used in the linear flow and a b factor between 0.3-0.75 is used in the boundary dominated flow depending on the best fit of the dataset. Time of linear flow vs. boundary dominated flow is determined from square root time plot described before.

Table 2. 1. Gas EUR comparisons from different decline methods. Five methods i.e. rate-time, rate-cumulative, multi segment, Duong and Stretched exponential are compared against each other. Rate time and rate cumulative plots give similar results and are on an optimistic side. Duong and stretched exponential are on a lower side. Multi-segment lies between these two extremes.

Well	Method	Gas EUR (BSCF)
Well 1	Rate time (modified hyperbolic, single b)	2.1
	Rate cumulative (modified hyperbolic, single b)	2.0
	Multisegment (rate-time)	1.6
	Duong	1.5
	Stretched exponential	1.2
Well 2	Rate time (modified hyperbolic, single b)	2.4
	Rate cumulative (modified hyperbolic, single b)	2.6
	Multisegment (rate-time)	2.1
	Duong	1.9
	Stretched exponential	1.5
Well 3	Rate time (modified hyperbolic, single b)	2.5
	Rate cumulative (modified hyperbolic, single b)	2.6
	Multigene (rate-time)	2.0
	Duong	1.8
	Stretched exponential	1.6

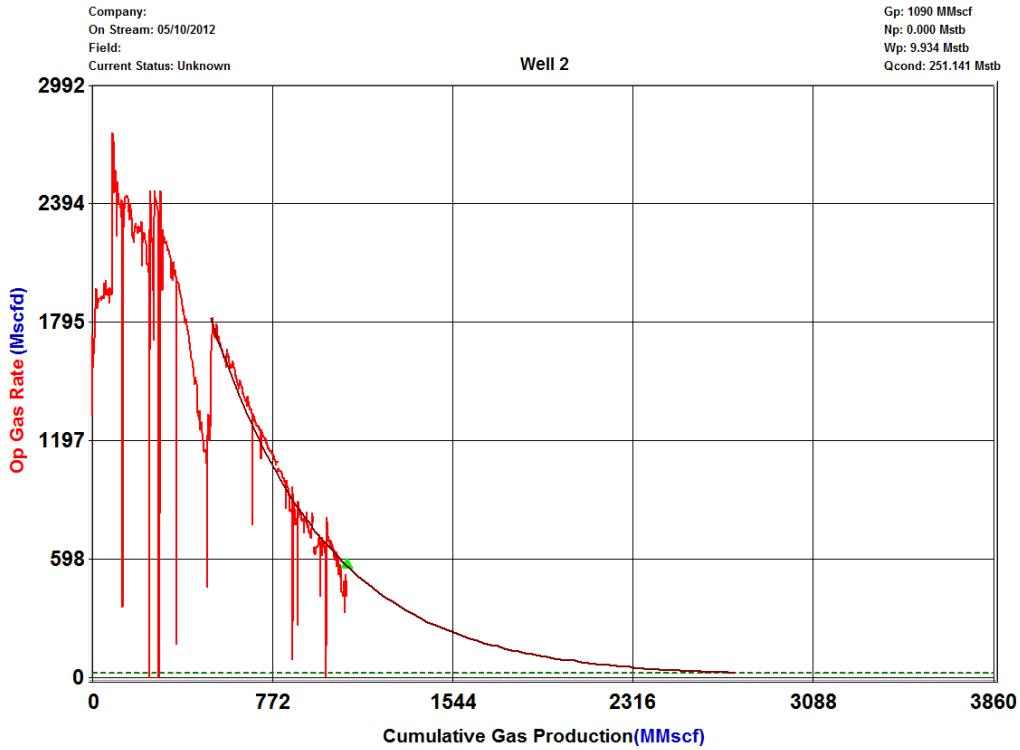

Figure 2.9. Decline summary for gas phase (well 1) on a rate-cumulative plot. Y axis show the surface gas rates (MSCFD) and the X axis shows the cumulative production. The decline is fitted until production history (green arrow) and forecast is made afterwards. The EUR's are bounded by specifying at rate cutoff of 1 MSCF/D.

2.4.2. Rate Transient Analysis

Unconventional RTA in this study uses a combination of square root time plot and flowing material balance (FMB). The platform utilized in this analysis is FEKETE Harmony®. Data required for RTA and the source of the data is summarized in Table 2.2.

Table 2.2. Input data summary for RTA

Data	Source
Oil, gas and water rates	Daily production report
Downhole gas rates	Single phase gas in reservoir assumption (oil volumes recombined into gas)
FBHP	Calculated from FTHP using Hagedon and Brown (all pressures converted to pseudo pressures for analysis)
Initial reservoir pressure	Post fracture report
Reservoir temperature	PVT report
Porosity, pay thickness, water saturation	Well logs
CO2, N2 for gas properties correction	PVT report (BWR)
Gas viscosity correlation	Carr et al.
Casing, tubing size, wellbore jewelry	completion report
Well profile	Deviation survey
Perforations	completion report

The plots used in RTA are:

a. Rate normalized pseudo pressures (FBHP) vs square root time
b. Flowing material balance
c. Forecast plot

The material balance plot is used to approximate the OGIP and the square root time plot is used for flow regime identification and fracture parameter derivations. These two plots are used in conjunction with each other. Moving the end of linear flow line also moves the FMB plots exaggerating OGIP's.

Hence, a control over time end of linear flow, t_{elf} (and hence permeability and fracture half lengths) is also obtained in the analysis. An example analysis for well 2 is summarized in Figure 2.10. Time end of linear flow is determined from the square root time plot. OGIP is determined from flowing material balance plot. Along with type curves a best fit on production data is obtained and used for forecasting production.

The same analysis is repeated for well 1 and well 3. The results are summarized in table 2.3. From table 2.3 it can be seen that, well 2 shows highest recovery factors which may be attributed to zipper fracturing effect (Sierra & Mayerhofer, 2014) as well 2 is the middle well.

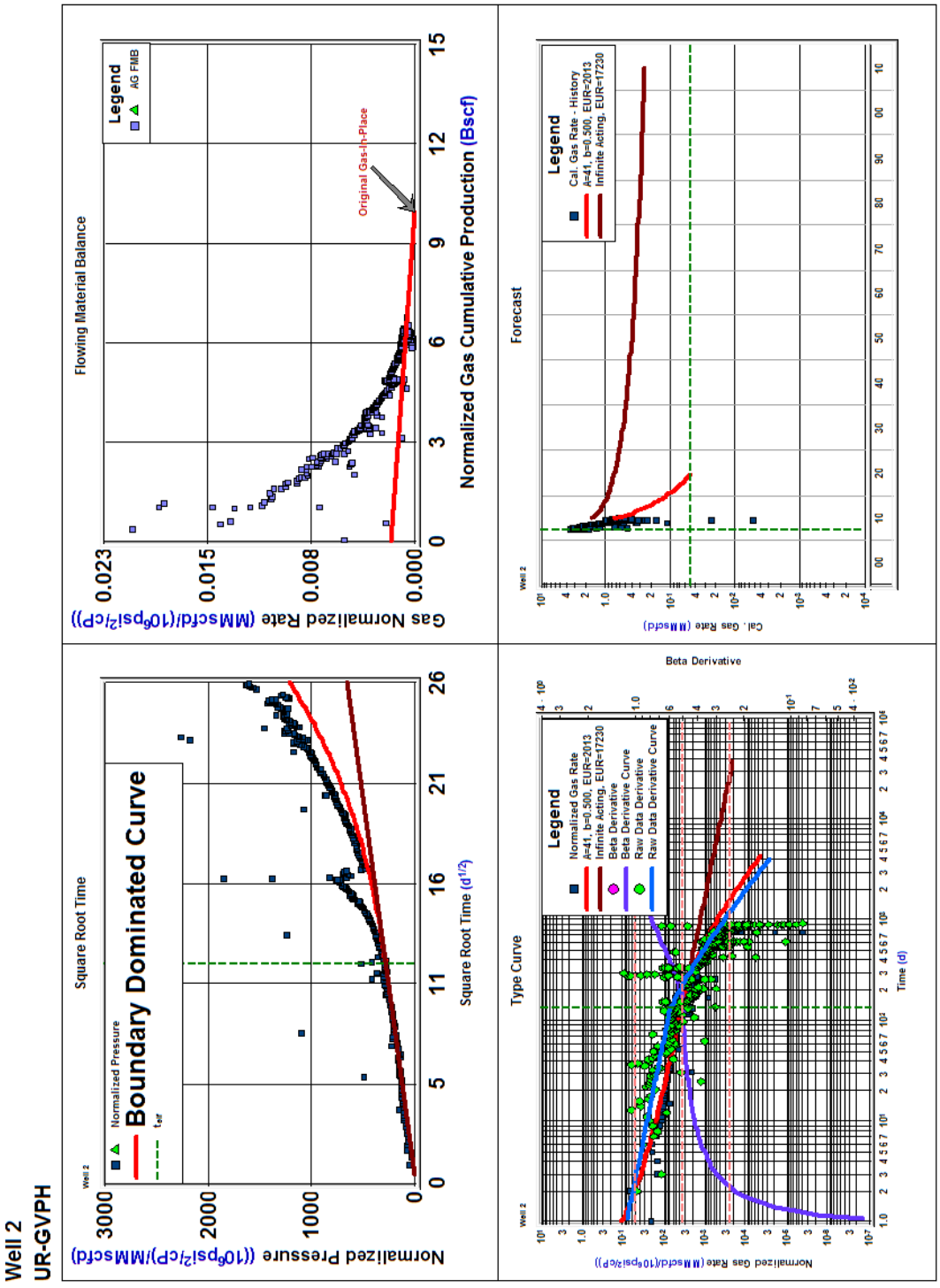

Figure 2.10. Example LFA summary (well 2). From left to right first plot is square root time plot used to identify end of linear flow and calculate time end of linear flow (t_{elf}). Second plot is the flowing material balance plot used to calculate original gas in place(OGIP). Plot on bottom left is the normalized gas rate (forecast plot) along with type curve. Last plot (bottom right) is the forecast plot.

Table 2.3. Results summary from RTA (the values are used in analytical models as seed value)

Parameter	Well1	Well 2	Well 3
Time end of linear flow (t_{elf}), days	70.0	135.0	142.0
Dimensionless fracture conductivity(F_{cd})	896.6	1000.0	533.9
Product of drainage area and square root permeability ($A_c k^{1/2)}$, $md^{1/2}$	83510.0	71893.0	70411.1
Matrix permeability (k), md	5.19E-05	1.18E-05	1.16E-05
Fracture half length (X_f), ft.	186.0	227.0	248.0
Expected ultimate recovery (EUR), gas BSCF	1.5	2.1	1.9
Original gas in place (OGIP), gas BSCF	8.1	10.7	10.1
Recovery factor (RF), gas percentage	19.0	19.7	18.4
Drainage area (A_{srv}), Acres	37.0	44.0	51.0

2.4.3. Analytical Mathematical Models

Analytical models are an effective way for independently matching pressure and rates simultaneously to gain more confidence on EUR's (Ekaterina Stalgorova & Mattar, 2013). The choice of the model is still argued and it mainly depends on the personal preference of the interpreter. Samandarli et al. (2014), have argued in the favor of using enhanced fracture zone model. Samandarli et al. (2014) and Suliman et al. (2013) observed multiple straight lines on the flowing material balance plots as well as square root of time plot indicating presence of zones of varying permeability or enhanced fracture zones.

Similar results were observed in the current dataset as well (Figure 2.11). In figure 2.11 multiple trends can be observed on the flowing material balance plot suggesting the rate transient moving from the inner more stimulated SRV (near wellbore) to another less stimulated SRV (away from the wellbore).

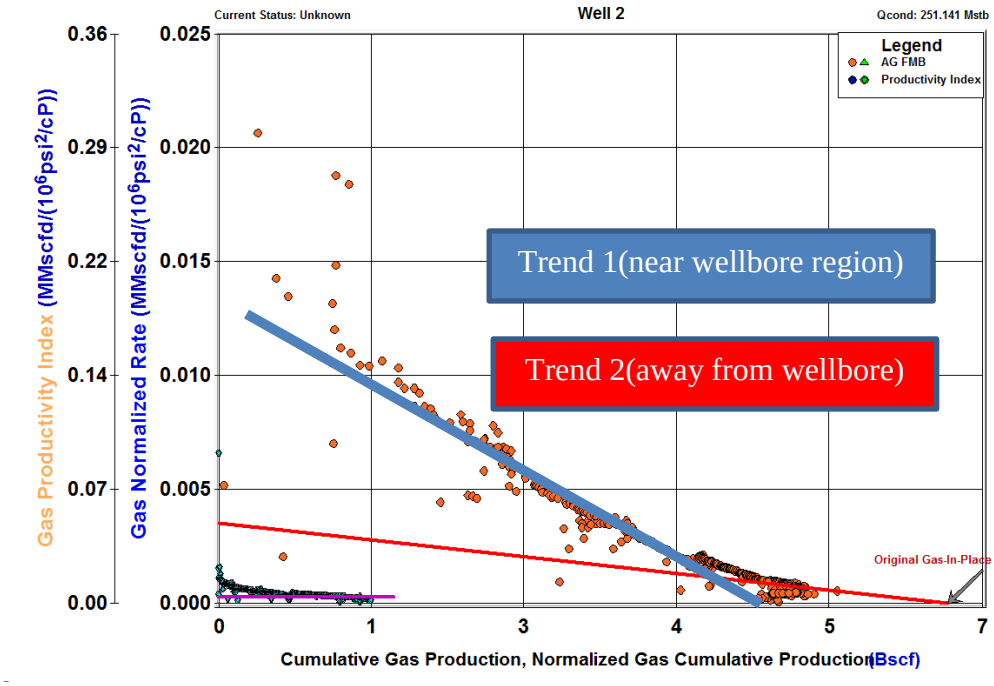

Figure 2.11. Multiple trends on FMB plots (indicating regions of variable permeability). First trend is shown by the solid blue line which extrapolates to a lesser OGIP value. The OGIP calculated from FMB increases as the transient moves from a more stimulated high permeability zone (near wellbore) to a less stimulated less permeable zone (away from the wellbore). The later trend and hence an insinuation of second SRV is seen by red line. Short term production is affected by the near wellbore highly permeable SRV and later trends can be explained by the outside or less permeable SRV.

In the current study following models are used and a comparative analysis of the results (EUR's, fracture half lengths and permeability's) are presented:

(a) Horizontal Multifracture SRV (Uniform fracture) Model: All the fractures are of equal length (Figure 2.12). Figure 2.12 demonstrates the geometry of this model is the most simplistic model which assumes all fractures are of equal fracture half lengths. The same fracture conductivity is assigned to all fractures.

(b) Horizontal Multifracture Enhanced Fracture Region Model: A region of high permeability near wellbore and then secondary permeability away from wellbore (Figure 2.13). Figure 2.13 demonstrates this model where it is assumed that the near wellbore area is more stimulated and the permeability diminishes away from the wellbore.

(c) General Horizontal Multifracture Model: Fractures varying half lengths and irregular geometry (Figure 2.14). Figure 2.14 shows the model with uneven fracture half lengths. This model can incorporate the uneven fracture half lengths if they are supported by some other dataset such as microseismic. However, varying permeability cannot be accounted in this model.

All the models are first initialized from RTA inputs and then a history match is attempted on gas phase and bottom hole pressures. Although, the model is not as rigorous as a full numerical simulation, analytical model can give a fair idea about fracture half lengths and matrix permeability's to further bolster the confidence in RTA. Figure 2.15 demonstrate the geometry and a match obtained from given well data on enhanced

fracture zone model. Table 2.4 summarizes the overall results. In figure 2.15 it can be seen that a good history match is obtained on both gas rate and pressure.

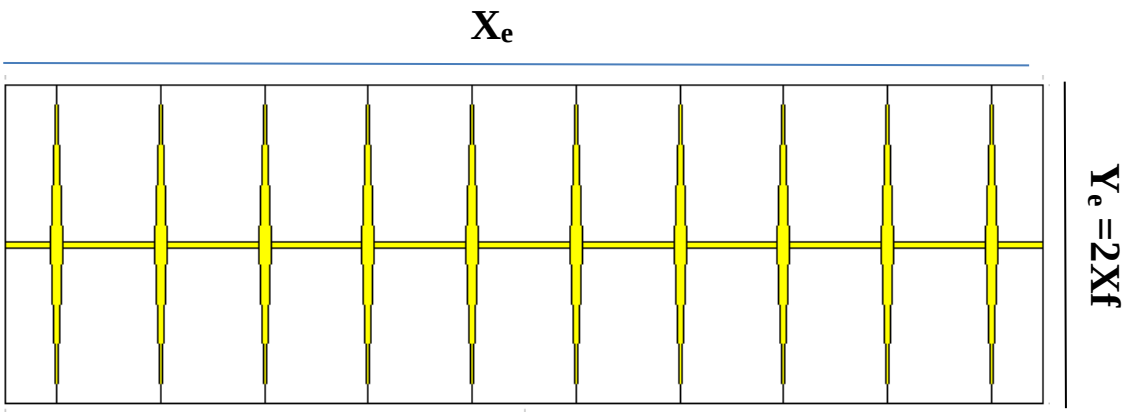

Figure 2.12.Example configuration for uniform fracture model (Ekaterina Stalgorova & Mattar, 2013). All fractures are of equal fracture half lengths. Ye = 2 X_f. Where X_f is the fracture half length. X_e is the perforated lateral length of the well.

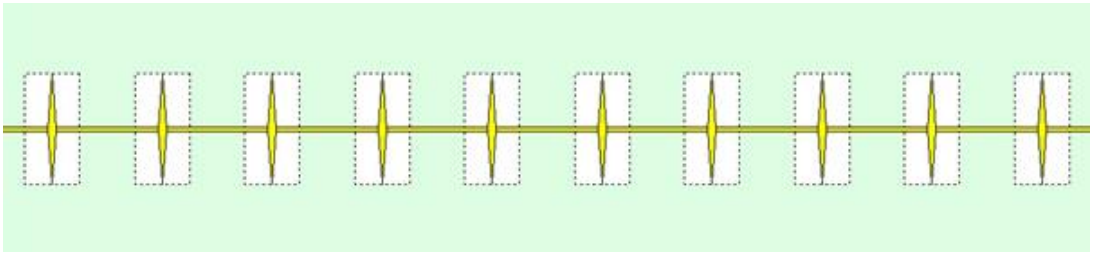

Figure 2.13. Example configuration for enhanced fracture zone model (Ekaterina Stalgorova & Mattar, 2013). Area in white around the fractures is the enhanced permeability zone around the fractures. Permeability decreases away from the wellbore which is the area in green.

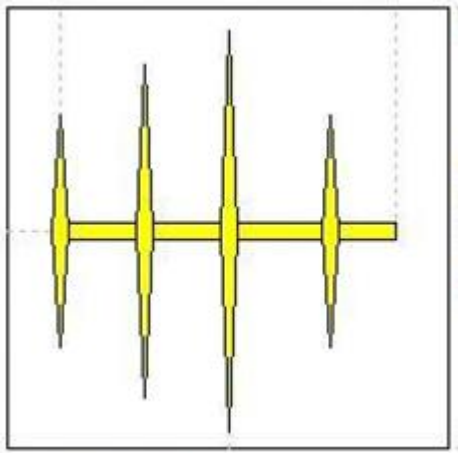

Figure 2.14. Example configuration of general multi fracture model (Ekaterina Stalgorova & Mattar, 2013). The diagram shows an instance where the fractures are of uneven fracture half lengths. Some fractures are longer than the others.

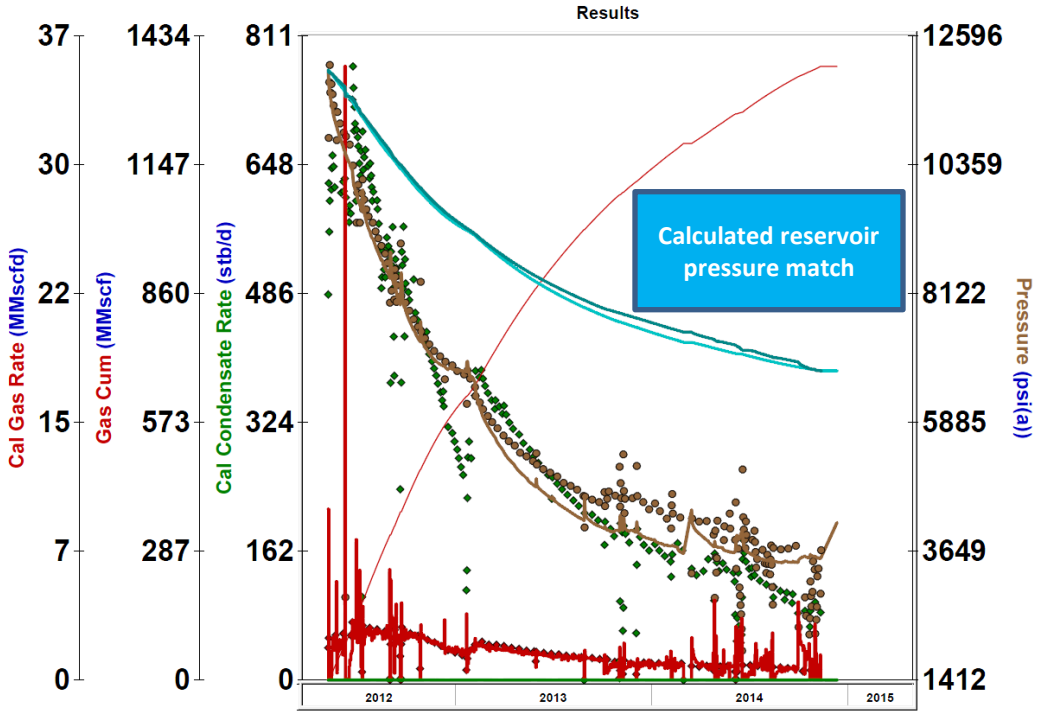

Figure 2.15.Results of history matching from enhanced fracture zone model. Plot shows the actual and predicted rates, cumulative and pressure. Red curve is the gas rate and brown curve is the calculated bottom hole pressure. Continuous curves are the simulated rates and pressure while the discontinuous curves are the actual data. The cyan curve is the recombined downhole gas rate. Dark green curve is the oil rate. The solid red, monotonically increasing line show the calculated gas cumulative. It can be seen a good history match is obtained in this case on all parameters.

From table 2.4 it can be seen that the EUR's obtained from all models are conformal. The dimensionless fracture conductivity(FCD) lies between 1000 – 1300 for all models. The fracture half lengths from 100-135 Ft. depending on the choice of the model.

All models are run with a gas rate control for the history match. After the history match a forecast is made by exit rates of gas i.e. the gas rate at the last production date. For the limiting condition a constraint is put on bottom hole pressure as well as well as gas rate. For bottomhole pressure a constraint of 800 PSI is used while for gas rate a constraint of 7 MSCFD is used. This implies if either of these constraints are reached the model will stop running and cumulative volumes till that date will be assumed to be the EUR.

Table 2.4. Results summary of analytical models								
Well	**Model**	**Gas EUR (BSCF)**	**Condensate EUR (MSTB)**	**History matched Xf (ft.)**	**F_{CD}**	**Forecast constraints (after history matched)**		**Well life**
						FBHP (Psia)	**Min. rate (MSCFD)**	
1	Enhanced fracture	2.1	431	116	1276	800	7	30 yrs.
	General multifracture	1.5	335	100	1276	800	7	30 yrs.
	Horizontal multifracture SRV (uniform fractures)	1.3	310	125	1066	800	7	30 yrs.
2	Enhanced fracture	1.2	268	135	1000	800	7	30 yrs.
	General multifracture	1.1	275	120	1000	800	7	30 yrs.
	Horizontal multifracture SRV (uniform fractures)	1.1	251	93	1000	800	7	30 yrs.
3	Enhanced fracture	1.6	384	118	1000	800	7	30 yrs.
	General multifracture	1.8	413	125	1000	800	7	30 yrs.
	Horizontal multifracture SRV (uniform fractures)	2.1	424	135	1000	800	7	30 yrs.

2.4.4. Discussion of Results

A comparison of EUR's between analytical models and DCA show the EUR's reported by analytical models are on a pessimistic side. It is a good workflow to perform the LFA /RTA first before moving to analytical models. Without performing the LFA/RTA and using analytical models do not provide results which are substantiated and are essentially a history match with arbitrary values.

The range of fracture half lengths derived from analytical models show that the area of SRV (Asrv) is different for all wells on the same PAD. Hence, the fractures grow unevenly for three wells on same PAD with same completions. Also, there is not a significant difference in key parameters with the choice of the model.

None of the wells show the fracture half lengths in order of 250 ft. and hence the 500 ft. spacing between the wells is not optimal. The mean fracture half lengths for all the wells ~ 118 ft., suggesting the well spacing should be ~ 250 ft. between the wells.
With current well spacing of 500 ft. a significant area is remained undrained in the lease. This scenario is demonstrated in figure 2.16 where the yellow portion of the reservoir show the drained reservoir area and blue represents the undrained portion of the reservoir.

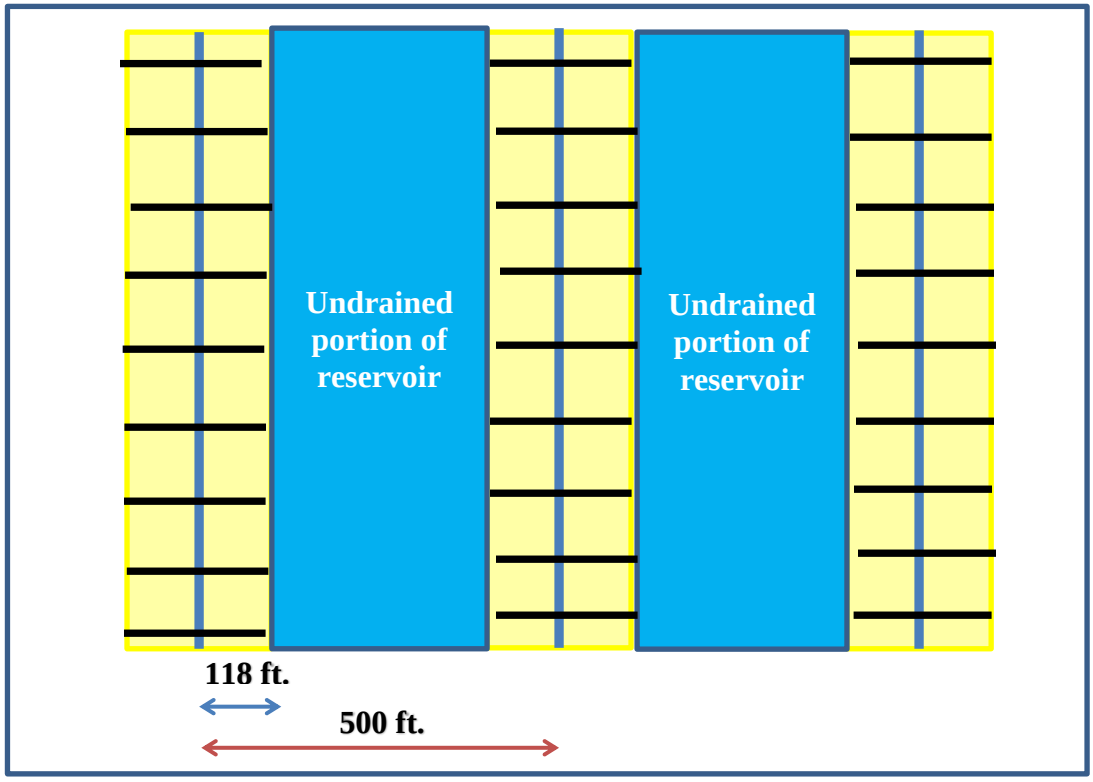

Figure 2.16.Drainage pattern based on uniform fracture geometry and rectangular SRV. The area in yellow is the drained portion of the reservoir while the area in blue is the undrained portion of reservoir. Sticks in blue represents the perforated lateral lengths of the wells while sticks in black represent the transverse fractures. The current well spacing between the wells is 500 ft.

3. Reservoir Simulation

3.1.Literature Review

Reservoir simulation is a sophisticated tool which can be used to quantify the reserves in unconventional reservoirs. However, its applicability to unconventional reservoirs are limited due to several factors (Andrade, Civan, Devegowda, & Sigal, 2010). From a practical point of view, following are the major setbacks for using reservoir simulation as a history matching tool:

(a) Due to enormous number of wells in the unconventional reservoir portfolio, it is enormously difficult if not impossible to build a full field scale model.

(b) It is commonly agreed that due to low permeability of shale reservoirs, if properly spaced they do not draw production from each other. In other words, if the wells are spaced properly, there is no rate interference. Hence, as the reservoirs are independent entities in itself (SRV, defined by transverse fracture tips) the EUR's can be forecasted by much simpler methods such as DCA.

(c) The basic assumption of conventional simulators i.e. gravity capillary equilibrium is not valid (Andrade et al., 2010). The capillary forces are dominant (also the definition of unconventional reservoirs) and hence water saturations are inaccurate.

(d) As the time of this study, the relative permeability curves for shales are not established and hence has to be used as history matching parameters in simulation study.

(e) Geomechanics plays an important role in deep shale reservoirs. Incorporating a fully coupled geomechanical solution, along with flow and composition (Minkoff et al., 1999; Settari and Walters, 2001;Dean et al., 2006) is a tedious task and is of questionable accuracy in case a full dataset for the study is not available.

(f) Well bottom hole pressures (especially in case of condensate and light oil fluid type) are not reliable as a permanent downhole gauge is rare in shale wells. Even the initial reservoir pressures are not reliable due to supercharging effect in the reservoir after hydraulic fracturing (Chang, Hammond, & Pop, 2005).

With above arguments, it is clear that a meaningful simulation study requires enormous amount of dataset and is a time consuming process. Hence, a simulation study is not justified for every well in the field. Often a compromise is thus, made by carrying out alternate studies. On the other hand, even with limitations with respect to intrinsic assumptions inside a conventional simulator, reservoir simulation can be a very powerful tool if used in properly with appropriate dataset.

The importance of reservoir simulation cannot be stressed enough especially for results on a field scale basis (surface rates, EUR's, condensate banking etc.). It can help visualize the SRV along with microseismic data, quantify the condensate dropouts in the reservoir with the help of a compositional model and along with several other applications it can help for a "what if" kind of sensitivities which is not possible by any other method.

For the purpose of this study a conventional simulator is used with an underlying assumption of Darcy's law for fluid flow with appropriate corrections applied for non-Darcy flow. To incorporate fluid properties an equation of state model is used. To

characterize the reservoir rock types well logs in conjunction with geostatistics is used in this study.

3.2. Methodology

In this study a three well PAD simulation is carried out. First, fine scale geo-cellular model is created. Then a compositional model is incorporated in the static model. Wells are coupled explicitly in the model. The bottom hole pressures are calculated same as in analytical model, with the help of wellbore jewelry and appropriate correlations (in our case, Hagedorn and Brown). Daily production data from individual wells is then history matched. Once a match is made, the same model is used to carry out different sensitivities with well spacing's. Based on the EUR's obtained by simulation and the OGIP's calculated using volumetric, recovery factor for each scenario is quantified.

3.3. Dataset Available for Simulation Study

For analysis, following data was providing by the operator. The dataset is divided into two parts: Wells under observation and offset wells. Observation wells are the wells used for simulation and offset wells are the neighboring wells used for static modeling. Following data is available from observation wells:

(a) Daily production history (surface oil, surface gas, surface water, flowing tubing head pressure) and operational history (choke info, shut in's, re-fracturing etc.) for three wells on a PAD. The wells are referred as well 1, well 2 and well 3 respectively. The same convention is held throughout the study

(b) Location and datum information (surface and bottom hole)

(c) Directional Surveys

(d) Completion reports

(e) Re-fracturing report from one of the wells

(f) Micro- seismic data (during fracturing)

(g) Flowback data

(h) Full compositional PVT from one of the nearby well with similar condensate gas ratio (CGR)

Following dataset is available from the offset wells:

(a) 5 Pilot well logs in vicinity of the PAD wells

(b) Location and datum information (surface and bottom hole) of offset and PAD wells.

3.4. Reservoir and Fluid Characterization

3.4.1. Petrophysical Analysis

Five pilot wells in the vicinity of the area were provided by the operator for the petrophysical modeling. The location of the wells relative to the location of actual wells is shown in **Error! Reference source not found.**1. From figure 3.1 it can be seen that t he observation wells (wells to be modeled) lie in the center surrounded by the pilot wells. As the wells are horizontal they show up as stick map on the diagram.

3.4.1.1. Well Log Processing

To process the logs, first the formation temperature gradient and pressure gradient are calculated. Using the bottom-hole temperature and surface temperature from PVT report, and an average formation temperature gradient is established. This temperature gradient

is used to calculate the bottom-hole temperatures in all the logs and subsequently used in different calculation to apply the temperature correction.

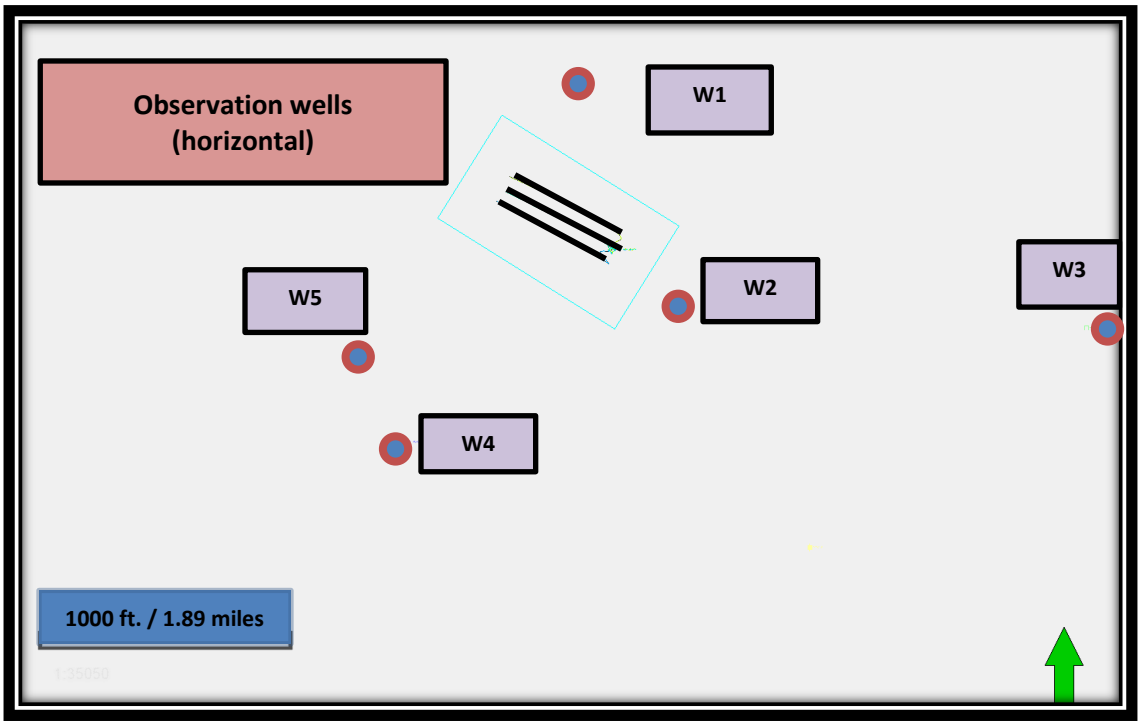

Figure 3.1. Observation wells and offset pilot well location (W1 to W5). Three wells on a PAD are shown in the figure as the stick maps (enclosed in a cyan polygon). These wells are referred as observation wells in the study (well 1, well 2 and well 3). Five wells in the vicinity are the pilot wells for which a full log suit is available. All petrophysical properties are calculated on pilot wells and are later interpolated for observation wells using geostatistics.

3.4.1.2. Pressure and Temperature Calculation for Well Logs Processing

Post fracturing reports are used to calculate the post fracture pressure gradient and hence to calculate the bottom hole pressure for all the wells. It is important to note here that, there are 5 offset wells, which are pilot wells and full log suit is available from all of them. These are used to model 3 horizontal wells surrounded by these wells (Error! Reference source not found.**). Fracturing reports are available for the 3 h orizontal wells which are fractured in a multi-stage fracturing fashion. Post fracturing reports of these wells are used to approximate reservoir pressure of the pilot wells. temperature gradient by TVD. Calculated formation temperatures can be seen in red.**

2 shows an example calculation of formation temperature.

To calculate formation temperature a linear model is used. First a temperature gradient is established using surface temperature (60-degree F) and bottomhole temperature (330-degree F) and well TVD (12864 Ft.). Then the gradient of 0.0254 degree F/ ft. is used to calculate bottomhole temperatures using well TVD's.

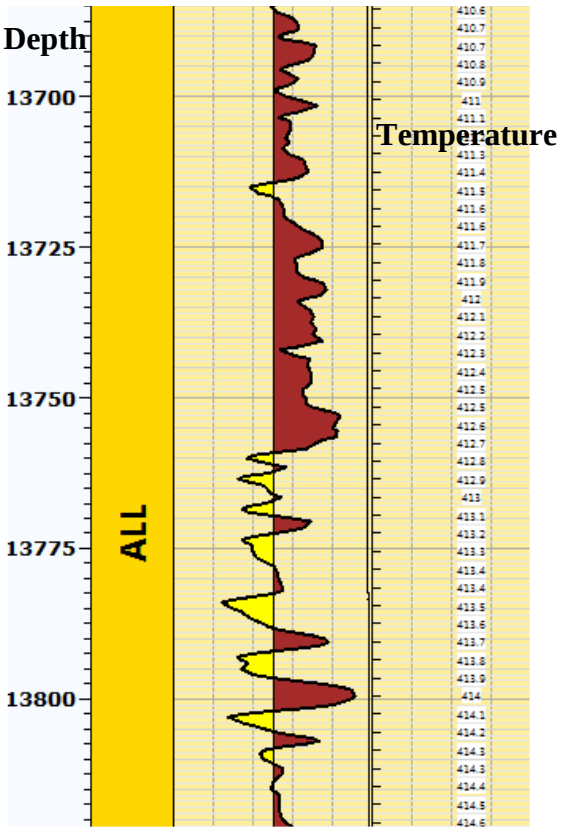

Figure 3.2. Example calculation of formation temperature for one of the offset pilot wells. First a temperature gradient is established from the PVT report. Then this gradient is used to calculate the temperature for all pilot well logs by simply multiplying temperature gradient by TVD. Calculated formation temperatures can be seen in red.

3.4.1.3.Calculation of Shale Volume (Vsh)

Next step in well log processing was to calculate the shale volumes (V_{sh}). Vsh volumes are necessary to apply appropriate corrections in the calculation of porosity. To calculate the shale volumes, many methods are used conventionally and is documented in detail by (Bassiouni, 1994). Out of many methods available for analysis, following methods are used and compared against each other.

(a) ***Gamma Ray***

Gamma ray method is the most common method to compute shale volumes. The gamma rays are emitted from the radioactive minerals present in the rock. Shale is usually rich in radioactive minerals and has a high gamma ray count. Sand on the other hand has a low gamma ray count due to absence of radioactive elements. The response from a formation is recorded on a detector which in most cases is a scintillation counter or a Geiger-Muller counter. Based on the radiation counts received, the formation is defined as a shale or a sand formation. In oilfield units, this gamma ray response is reported in API (Crain, 2016a)

Gamma ray response is available from all 5 offset wells in this study. These gamma ray responses and frequency are plotted for all wells in Figure 3.3. Plotting all the wells together helps in data visualization and fixing the limits for gamma ray count response for matrix and shale.

Although standard values are available for sandstone and carbonate, these values can be set manually by looking at the curves and simultaneously picking up responses, which are most likely to be matrix and shale. This is a critical step as these values are replaced

in the formulas used in calculation of V_{sh}. For calculation of V_{sh}, first the gamma ray index (GR_{index}) is calculated as:

$$GR_{index} = \frac{GR - GR_{matrix}}{GR_{shale} - GR_{matrix}} \tag{3.1}$$

Where, GR is the gamma ray count, GR_{matrix} is the gamma ray count of matrix set from Figure 3.3, GR_{shale} gamma ray count of shale, set from Figure 3.3. Once GR_{index} is calculated, Clavier equation is chosen to calculate V_{sh}. Clavier equation is chosen as it is a good compromise between tertiary and older rock equations (Saputra, 2008). Vsh volumes from Clavier equation is given as,

$$V_{sh} = 1.7 - \sqrt{3.38 - (GR_{index} + 0.7)^2} \tag{3.2}$$

An example of Vsh volumes calculated from this methodology is demonstrated in Figure 3.4 along with Vsh calculated from resistivity log only. It can be seen that the shale volumes calculated from resistivity logs is on a higher side and shale volumes calculated from gamma ray log are on a more realistic side.

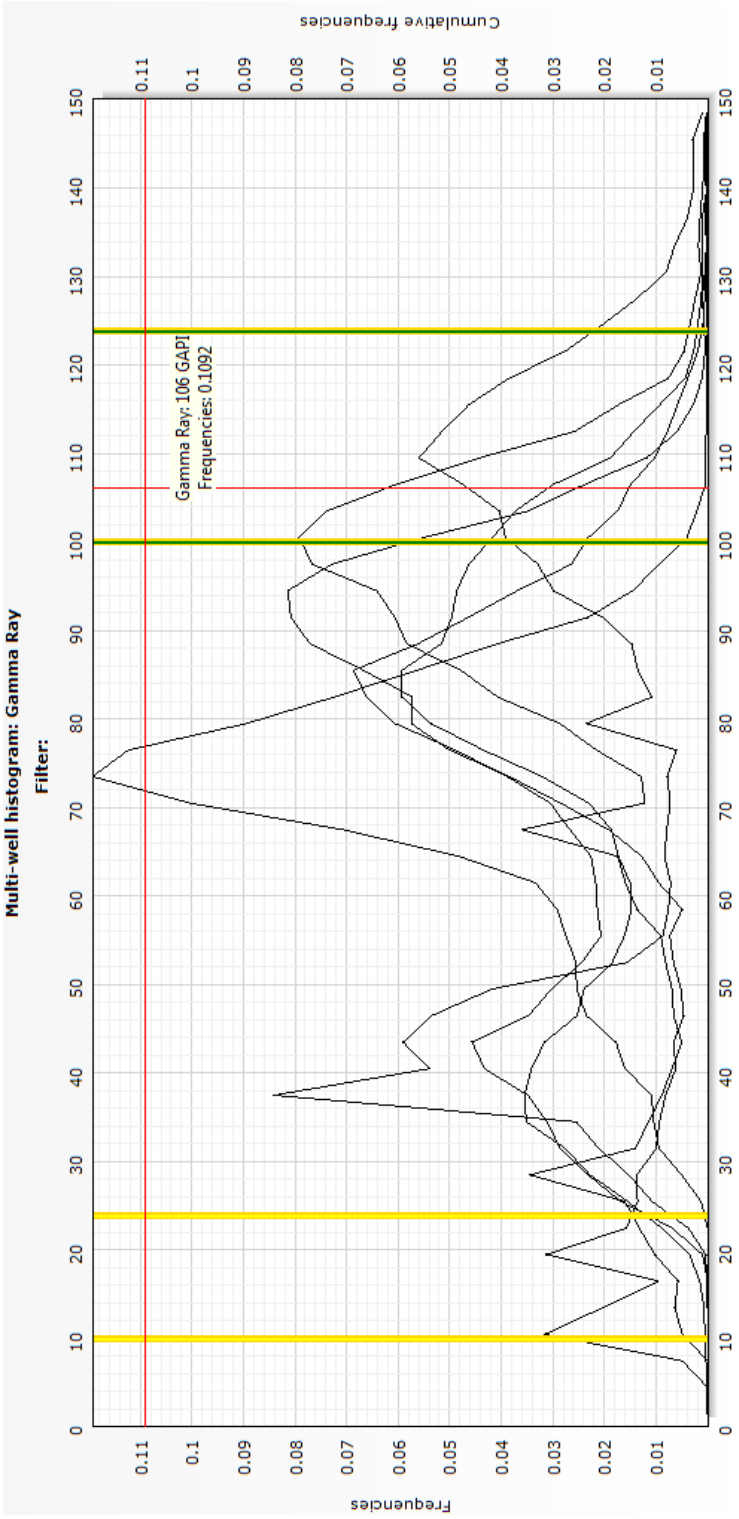

Figure 3.3. Gamma ray response from all five pilot well logs. On X axis is the gamma ray count and on the Y axis is the frequency of the count. Cutoff range for sand and shale is shown by yellow lines. Limit for shale is set off at higher gamma ray count (extreme right) while sand is set at low gamma ray count (extreme left).

(b) Neutron-Density method

V_{sh} volumes can also be calculated from neutron density crossplots. The separation between neutron and density log is an indicator of shale volumes (Adeoti, Ayolabi, & James, 2009). Response equations for density and neutron logs are summarized as (Crain, 2016b)

$$PHID = PHIe(Sxo)PHIDw + PHIe(1 - Sxo)PHIDh + Vsh(PHIDsh) + (1 - Vsh - PHIe)[Sum(Vi * PHIDi)] \quad (3.3)$$

Where, PHI_{Dh} is the log reading in 100% hydrocarbon, PHI_{Di} is the log reading in 100% of the ith component of matrix rock, PHI_D is the log reading, PHI_{Dsh} is the log reading in 100% shale, PHI_{Dw} is the log reading in 100% water, PHI_e is the effective porosity (fractional), S_{xo} is the water saturation in invaded zone (fractional), V_i is the volume of ith component of matrix rock, and V_{sh} is the volume of shale (fractional). Similarly, the response equation for neutron porosity is given as:

$$PHIN = PHIe * Sxo * PHINw + PHIe * (1 - Sxo) * PHINh + Vsh * PHINsh + (1 - Vsh - PHIe) * Sum(Vi * PHINi) \quad (3.4)$$

Where, PHI_{Nh} is the log reading in 100% hydrocarbon, PHI_{Ni} is the log reading in 100% of the ith component of matrix rock, PHI_N is the log reading, PHI_{Nsh} is the log reading in 100% shale, PHI_{Nw} is the log reading in 100% water, PHI_e is the effective porosity (fractional), S_{xo} is the water saturation in invaded zone (fractional), V_i is the volume of ith component of matrix rock, V_{sh} is the volume of shale (fractional). The following assumptions are made:

$$PHIDw = PHIDh = PHINw = PHINh = 1.0,$$
$$PHIDi = PHINi = 0, \quad (3.5)$$
$$Sxo = 1.0$$

Subtracting equation 3.5 from equation 3.4 we get equation 3.6. It is clear that to get the values of Vshxnd from a crossplot a linear interpolation is required. The crossplot between the neutron and density porosity used for this purpose. It is possible to plot multiple wells simultaneously and same is done in this thesis.

$$Vshxnd = (PHIN - PHID) / (PHIN_{Sh} - PHID_{Sh}) \quad (3.6)$$

Although, this method was developed to work on a sand matrix, it does work very well in our case as well. Figure 3.5 shows a crossplot of Vsh volumes calculated from gamma ray and from that of neutron density show they both yield identical results. Hence, in our area of interest both can be used to calculate shale volumes.

(c) Resistivity (uses deep resistivity logs)

Another attempt to calculate V_{sh} is made using the deep resistivity log alone. Resistivity log is generally useful for calculating Vsh volume in low salinity reservoir and in tar sands. The methodology works very well in reservoirs with formation water salinity < 10,000 ppm. I case of water salinity more than 10,000 ppm this method overestimates the shale volumes. In case of most reservoirs the formation water salinity is more than this thus limiting its use to tar sands.

Nonetheless, V_{sh} volumes are also calculated by using resistivity logs. The equation used in calculation of V_{sh} from deep resistivity log is:

$$V_{sh} = \frac{(log10(R_t) - log10(R_{ma}))}{(log10(R_{sh}) - log10(R_{ma}))} \quad (3.7)$$

Where, Vsh is the calculated shale volume, Rt is the deep desistivity, Rsh is the shale resistivity, and Rma is the matrix (sand) resistivity.

The shale volumes calculated from resistivity logs is plotted along with those calculated from gamma ray in Figure 3.4. It can be observed that in our case resistivity overestimates the shale volume. Final shale volumes are then taken from gamma ray logs as it is available in all the wells.

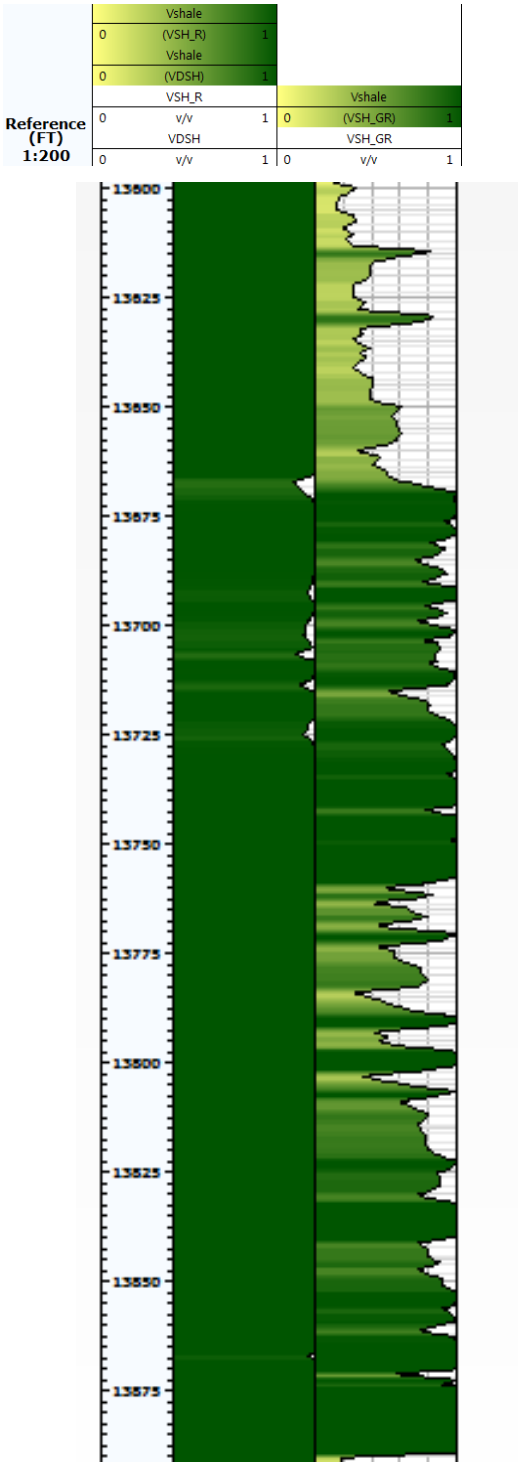

Figure 3.4. Vsh comparison between resistivity and gamma ray in EFS zone. Left is resistivity and right is gamma ray shale volume respectively. Shale volumes calculated from resistivity overestimate shale volumes. Scale for shale volumes is set from 0-1.

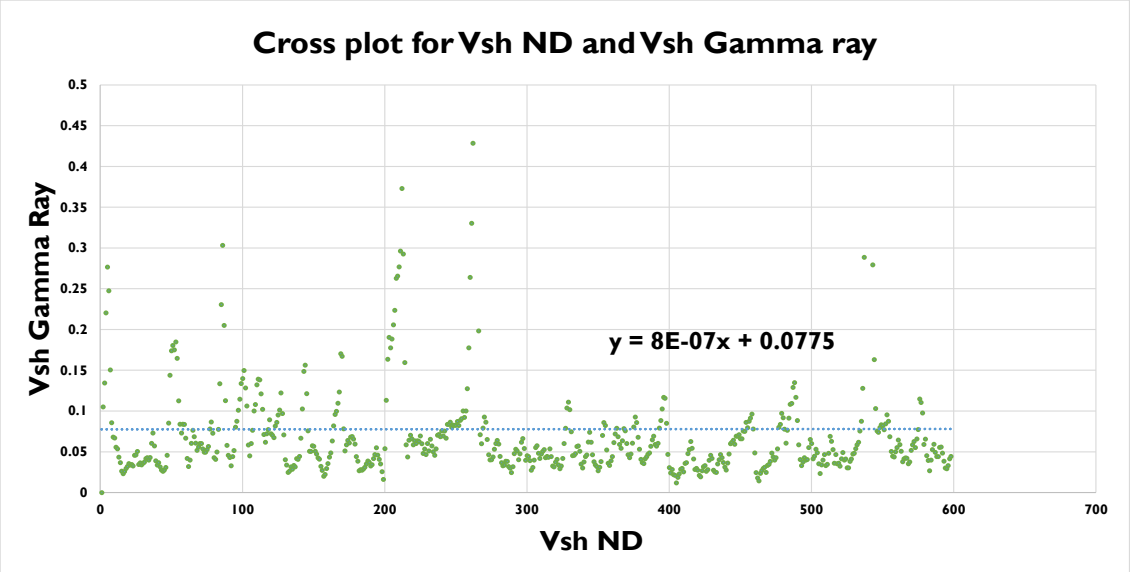

Figure 3.5. Vsh comparison from gamma ray and neutron density. Both methods yield similar results. In case one is not available other can be used using the regression equation.

3.4.1.4.Calculation of Porosity

Next step in the analysis was the porosity calculation. As the ultimate aim of this study is to use the model parameters in simulation, effective porosities along with total porosities are calculated to justify both reservoir characterization and simulation aims. A series of methods were used in this study to calculate the total and effective porosity such as Neutron –Density crossplot, density log, neutron log and sonic log.

A series of pre-computations were done before the porosity calculation. A complex lithology model is assumed for these models. Use of simpler models such as shaly-sand (Crain, 2016b) is avoided. Simpler models do not represent the lithology of Eagle Ford shale and a separate discussion on the mineralogy of the EFS.

Overall representative mineralogy is summarized in figure 3.7. Sondhi (2011) has documented the mineralogy of EFS from Fourier transform infrared spectroscopy (FTIR)

analysis of core samples. From figure 3.8 it can be seen that the formation mainly consists of carbonate and clay with a little feldspar, quartz and clay. Hence, a complex lithology model is appropriate for the calculation of porosity. Using simpler models such as shaly-sand (Crain, 2016b) can result in serious errors.

Calculation of water resistivity (R_{mf}) and mud filtrate density (ρ_{mf})

Before computing porosity from any of the methods above, it is important to calculate water resistivity and mud filtrate density as these values are used in the calculation of porosity from well logs. Calculation of R_{mf} and P_{mf} is done inside Techlog® using the formation water salinity first parameter, mud filtrate resistivity at room temperature, R_{w75} is calculated as (Schlumberger, 2016):

$$Rw_{75} = 0.0123 + \frac{3647.5}{(salinity)^{0.955}} \tag{3.8}$$

Where, Rw_{75} is water resistivity at room temperature, salinity is the salinity of formation water. Once R_{w75} is calculated, temperature correction is applied to mud filtrate resistivity using following equation:

$$R_{mf} = Rw_{75} * \frac{(75 + 6.77)}{temp + 6.77} \tag{3.9}$$

Where, R_{mf} is mud filtrate resistivity, and *temp* is the formation temperature (F). A formation temperature of 330°F from the PVT report is used to calculate the mud filtrate resistivity. Formation salinity of 80,000 ppm is assumed for the calculation.

Once, resistivity of mud filtrate is calculated and adjusted for reservoir temperature, the density of mud filtrate can be calculated as,

$$\rho_{mf} = 1 + \frac{(0.73 * salinity)}{10^6} \tag{3.10}$$

Where, ρ_{mf} is the mud filtrate density. Using, these parameters, the porosity of flushed zone is calculating. Flushed zone is an area directly surrounded by the wellbore. As the well is drilled with overbalanced scheme, the immediate area around wellbore contains mud filtrate and not the formation fluid. This effect in porosity and saturation calculations is corrected by using flushed zone porosity. The flushed zone saturation can be calculated as:

$$S_{xo} = \frac{(a * Rmf)^{1/n}}{(Rxo * \varphi^m)} \tag{3.11}$$

Where, S_{xo} is the saturation of the flushed zone, Rxo is the resistivity of the flushed zone, Rmf is calculated in the previous step using the formation salinity. To calculate the resistivity of the flushed zone, shallow resistivity log (RT30) provide by the service provider is used.

Correction for neutron and density logs

The neutron and density logs provided by the service provider have to be corrected before using for any analysis. Correction to these logs have to be applied on the account of effect of hydrocarbons on these log readings. A detailed account of the correction procedure theory is out of scope of this thesis (Gaymard & Poupon, 1968; Hester, 1999;

Schmidt, Land, Kilgore, & Yunker, 1971). A brief discussion is presented in this thesis on the major corrections applied.

Correction for neutron porosity

(a) Correction for presence of Hydrocarbons:

Fist the hydrogen index (hydrogen content per unit volume of hydrocarbons) of hydrocarbons is calculated and then transformed into a hydrogen index alpha as:

$$\alpha = 9 * \rho_{HC} * [0.15 + 0.2(0.9 - \rho_{HC)})^2 \quad (3.12)$$

Where, α is the hydrogen index factor and ρ_{HC} is the density of hydrocarbon. Then a factor alpha is defined (Gaymard & Poupon, 1968) to adjust the neutron density log with hydrogen index (HI) as well as salinity of mud filtrate and density of hydrocarbon. The specific gravity of the recombined gas from PVT analysis is taken as density of hydrocarbon. Salinity of mud filtrate is taken as that of fresh water (35 ppm). Using these values, the correction factor is used as:

$$B = \frac{[\rho_{mf} * (1 - S_{mf})] - \alpha}{\rho_{mf} * (1 - S_{mf})} \quad (3.13)$$

This correction factor is then applied to the porosity values.

(b) Correcting for excavation effect

The resultant porosity obtained after applying the hydrocarbon correction is the liquid filled porosity. This equivalent liquid filled porosity however shows a very low value as the gas filled porosity is treated as matrix in the calculation (Hester, 1999). Hence, "excavating" this matrix from the calculation gives the corrected neutron porosity.

This is corrected first by calculating SHC and then calculating the neutron density correction factor as:

$$S_{HC} = HI * (1 - S_{xo}) + HI_f * S_{xo} \tag{3.14}$$

Where, S_{HC} is the hydrocarbon saturation, HI_f is the hydrogen index fluid, Sxo is the saturation in flushed zone, HI is the hydrogen index of 100% saturated sample. After that the correction factor ΔNPI(excavation effect correction factor) is calculated as,

$$\Delta NPI_{EX} = 0.2731 * (\rho_{ma})^{2.1} * (1 - S_{HC}) * (0.02 * \varphi + \varphi^{1.8} * S_{HC} * (0.6493 + 0.2149 * S_{HC})) \tag{3.15}$$

Where, ρ_{ma} is the density of matrix, φ is the neutron porosity. The final corrected neutron density is then given as:

$$NPHI_{HCC} = NPI + (B * \emptyset * S_{hr} + \Delta NPHI_{EX}) \tag{3.16}$$

Where, $NPHI_{HCC}$ is the excavation effect corrected neutron porosity

Bulk density correction

Procedure explained by (Gaymard & Poupon, 1968) is followed in correcting the bulk density log. First hydrogen weight fraction in hydrocarbons is calculated as:

$$N_h = 0.15 + \frac{(0.9 - \rho_{HC})^2}{5} \tag{3.17}$$

Where, ρ_{HC} is the density of hydrocarbon, and N_h is the hydrocarbon weight fraction. Then electric density of hydrogen is calculated as:

$$C_h\rho_h = \rho_{HC} * (1 + N_h) \quad (3.18)$$

Where, $C_h\rho_h$ is the electric density. A factor is then required to correct the bulk density log in presence of hydrocarbons and also corrects for the mud salinity and density of hydrocarbons. This factor referred as A and calculated as:

$$A = 1.07 * \left[\left(1.11 - 0.15 * S_{mf}\right) * \rho_{mf}\right] - C_h\rho_h \quad (3.19)$$

Where, S_{mf} is the saturation in mud filtrate zone, ρ_{mf} is the mud filtrate density, and $C_h\rho_h$ is the electric density calculated in previous step. The final corrected density log is given as:

$$RHOB_{HCC} = RHOB + (\emptyset * A * S_{hr}) \quad (3.20)$$

Where, $RHOB_{HCC}$ is the corrected bulk density.

Porosity calculation results

A comparison of the porosity results can be seen in **Error! Reference source not found.**6 after applying correction to the porosity log in one of the wells. It is clear that sonic is too optimistic in estimating the porosities and ND and density give almost the same porosities. Hence, an average of these two porosities is taken for the calculation.

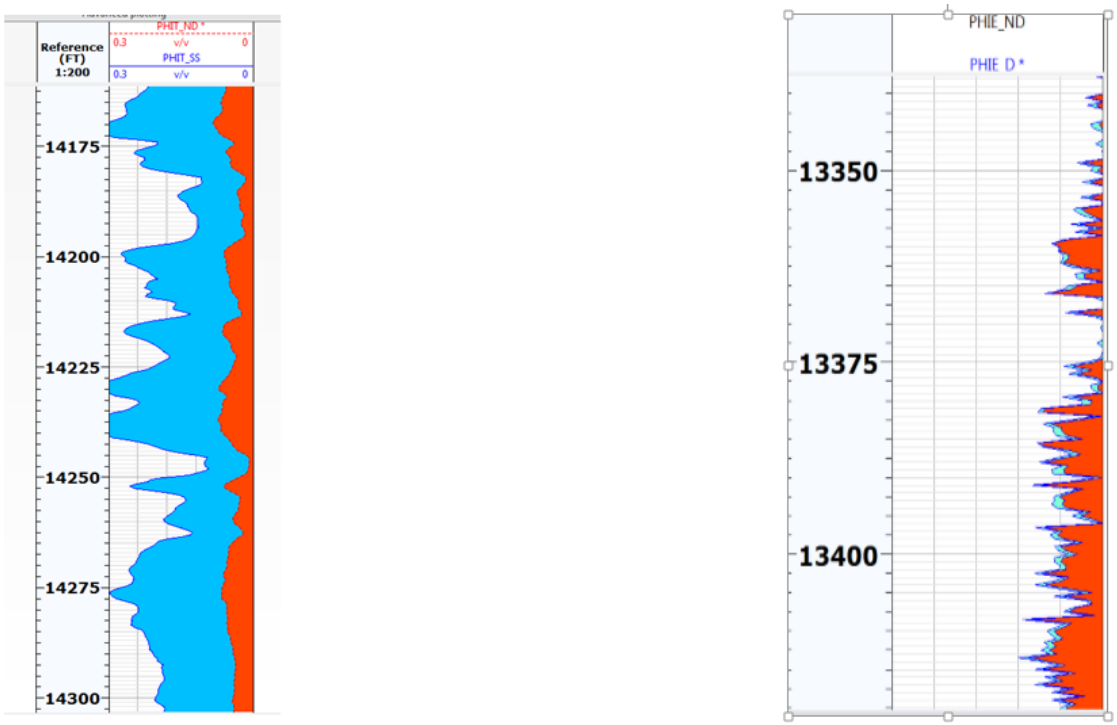

Figure 3.6. Overlay of sonic (blue) vs neutron –density (ND) is on the left and overlay of density porosity(cyan) and neutron –density(red) is on the right. It can be observed sonic overestimates the porosity while density porosity and ND are conformal.

3.4.1.5. Calculation of Saturation

Saturation calculation for shales has always been a controversial issue and different methods have different advantages and limitations (Rosepiler, 1982). In this study the following methodology was used:

(a) To fix the, m and n parameters first the mineralogy was fixed.

(b) Once the mineralogy is fixed, appropriate a, m and n parameters for the mineralogy is selected

Calculation of mineralogy

For the calculation of mineralogy two methods of mineralogy calculation are used. First is the Fourier Transform Infrared Spectroscopy (FTIR) and second is the mineralogy log. Although a mineralogy log is available from one of the well logs usually it is not a good practice to fix the mineralogy from well logs alone. There are no core samples available in this study to calibrate the well logs. Hence, work done by Sondhi (2011) is used. Sondhi (2011), documented the Fourier Transform Infrared Spectroscopy (FTIR) mineralogy from core samples of EFS.

A comparison is made to choose between the two methods (logs and FTIR) by computing the bulk density log. Mineralogy from mineralogy log (photoelectric) and FTIR was used to assign weighted averages from individual mineral density. Then this weighted averaged density was computed and compared against the density from the density log.

The weighted average of density from mineralogy was computed as 2.5 gm/cc. However, the weighted average density computed from the mineralogy (**Error! R eference source not found.**) given by Sondhi (2011), generated a value of 2.71 gm/cc. The bulk density results are shown in **Error! Reference source not found.**, it can be s een that the bulk density is closer to 2.71 gm/cc. So FTIR predicts the density better than mineralogy log. Hence, FTIR mineralogy is considered as best approximation for choosing a, m and n parameters.

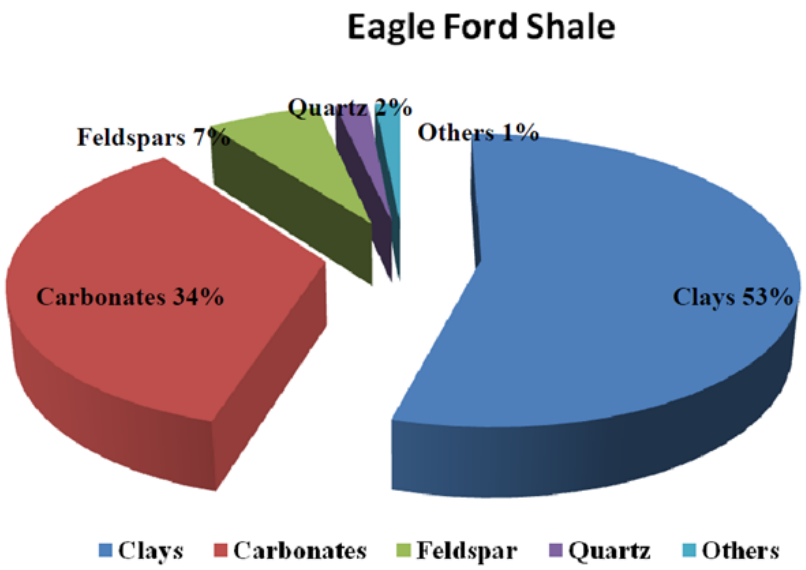

Figure 3.7. FTIR mineralogy given by Sondhi (2011). Eagle Ford mineralogy consist of mainly carbonate and clay with minor percentages of feldspar, quartz and other minerals.

Calculation of a, m and n parameters

Once, the mineralogy is fixed, a rigorous previously validated methodology for water saturation calculation was needed. In this thesis, from the mineralogy (**Error! Reference source not found.**) it is clear that our formation is majorly calcite and clay. A comprehensive analysis of usage of Archie's equation on carbonate matrix is done by Hamada et al. (2010).

The study includes three methods to calculate water saturation values on carbonate matrix: conventional, core Archie's parameter estimates (CAPE) and 3D. The same methodology is adopted in this thesis to obtain optimal Archie's parameters for water saturation calculation.

The process is repeated and compared with a, m and n parameters described by Hamada et al. (2010) with different water saturation calculations equations such as: Archie's, Simandoux, Total Shale, Waxman Smits and Indonesian Shale.

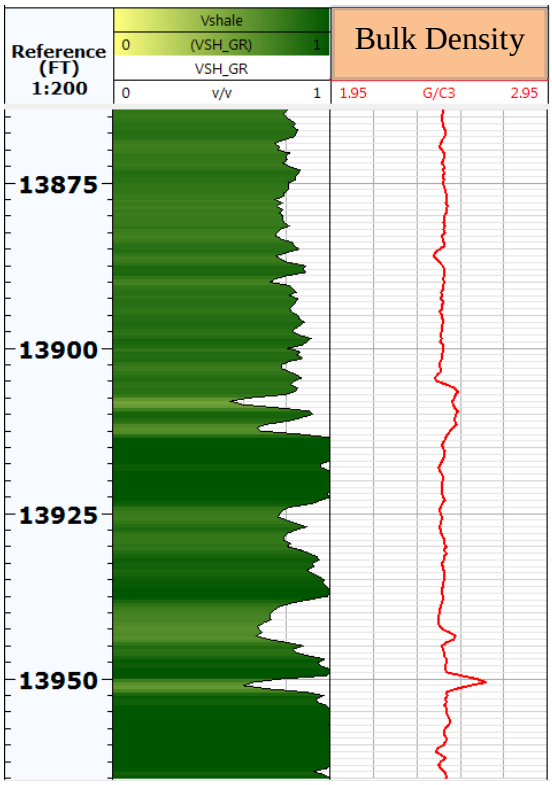

Figure 3.8. Bulk density and gamma ray log. Bulk density in the EFS zone ~ 2.71 gm/cc. The FTIR mineralogy conforms with the density log. However, the weighted average density from mineralogy log underestimates the density.

The analysis yielded best results for a, m and n parameters of 0.28, 2.34 and 2.87 respectively with Simandoux equation (Figure 3.9). Equation 3.21 shows the usage of Simandoux equation(Doveton, 2001). It is a linearized equation porosity term is replaced by $(1 - V_{sh}) * S_w/F$ and the equation is set up in terms of conductivity instead in terms of resistivity. This guarantees the equation falls back to Archie's equation when V_{sh} (calculated previously) when $Vsh = 0$ (Crain, 2016c).

$$S_{wa} = (A * Rw@/(PHIe^{M})/RESD)\text{^}(\frac{1}{N}) \quad (3.21)$$

Where, PHIe is the effective porosity, Rw is the Water resistivity, F is the formation factor of clean rock, RESD is the deep resistivity, A, M, N are the Archie's parameters, and Vsh is the shale volume previously calculated by gamma ray log.

Figure 3.9 shows that Archie's over predicts (nearly all water saturation made to 100%) the water saturation and cannot be used optimally to calculate water saturation in this case. Simandoux equation on the other hand gives reasonable results with parameters described by Hamada et al. (2010).

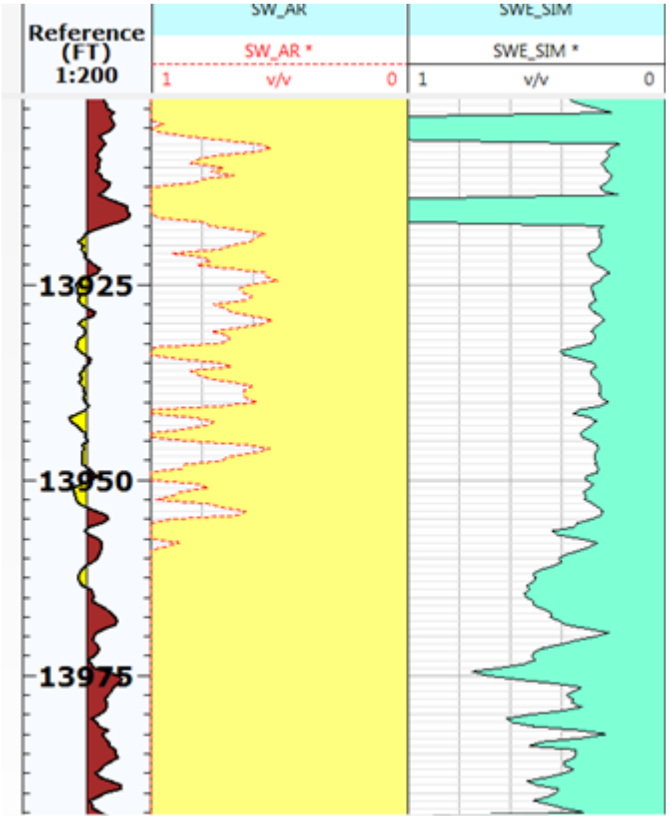

Figure 3.9. Water saturation calculation. (Left to right on track: GR, Sw-Archie's and Sw- Simandoux). It can be seen that using Archie's equation logs predict almost 100% water saturation while with Simandoux equation predicts reasonable results for water saturation.

3.4.2. Rock Typing and Well to Log Correlation

Rock typing is done to identify rock types which can affect production performance from the wells. These rock types are later incorporated for static modeling. As only well logs are available for analysis these well logs have to be calibrated with core data before arriving on rock types. As no core data is available a previous study done in EFS by (Workman, 2013) is used.

Workman, 2013 documented a detailed lithology model and workflow for EFS. He identified eight lithology in EFS based on core data available from 4 pilot wells. Figure 3.10 shows the lithology of carbonates as documented by (Dunham, 1962) and used later by (Workman, 2013).

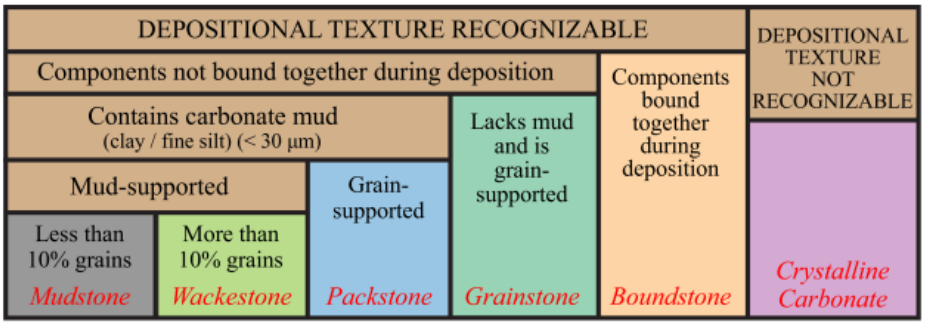

Figure 3.10. Diagramatic representation of the Dunham (1962) classification of carbonate rocks according to depositional textures and whether a rock is matrix or framework supported. Based on (Workman, 2013)

	Facies	Color	Dominant Mineralogy (Avg. %)			Sedimentological Character	Primary Grain Constituents	TOC	Matrix Permeability	Gas-Filled Porosity	Gas Saturation	No. of Samples
			Clays	Quartz	Calcite			(Avg. %)	(nD)	(%)	(%)	
1	Laminated Argillaceous Mudstone	Dark Greenish Black to Black	42.71 (n=14)	20.54 (n=14)	25.21 (n=14)	Fissile, Planar Laminated (mm), Localized Burrowing	Planktonic Foraminifera	3.29 (n=8)	1.94	2.61	26.11	10
2	Weakly Laminated Calcareous Foraminiferal Mudstone	Brownish Black to Olive Black	20.32 (n=51)	13.25 (n=51)	57.60 (n=51)	Planar, and truncated and wavey Ripple Laminae (mm), Erosive Bases, Localized Burrowing	Globigerinid Foraminifera, Fragmented Inoceramid Bivalves	3.71 (n=38)	2.35	3.28	32.02	25
3	Laminated Foraminiferal Wackestone	Light- to-Medium Grey	11.80 (n=27)	9.19 (n=27)	71.47 (n=27)	Planar and Ripple Laminae, Localized Burrowing	Globigerinid Foraminifera	2.46 (n=12)	1.70	2.67	49.49	15
4	Bioturbated Skeletal Lime Wackestone	Light Bluish Grey to Medium Dark Grey	5.37 (n=17)	4.59 (n=17)	86.04 (n=17)	Bioturbated, Mineralized Fractures	Bivalve Fragments and Undifferentiated Skeletal Material	0.82 (n=16)	5.85	4.46	54.11	2
5	Laminated Inoceramid and Foraminiferal Wackestone to Packstone	Black to Medium Bluish Grey	16.50 (n=2)	12.50 (n=2)	64.00 (n=2)	Imbricated- and Cross-Bedded Skeletal Debris (mm-cm), Planar Laminae (mm)	Fragmented Inoceramid bivalves, Globigerinid Foraminifera, Peloids, Phosphatic Grains	1.89 (n=1)	1.11	2.77	47.73	2
6	Skeletal Packstone to Wackestone	Medium- to-Light Grey	11.73 (n=11)	4.73 (n=11)	78.15 (n=11)	Cross Laminated and Imbricated bedding, Scour Surfaces, Fining Upward Sequences (cm)	Globigerinid Foraminifera, Fragmented Inoceramid Bivalves, Ostracods, Phosphatic Grains	0.98 (n=13)	0.24	2.19	46.74	4
7	Foraminiferal Packstone to Grainstone	Light Grey	4.63 (n=15)	7.56 (n=15)	84.19 (n=15)	Planar and Ripple Laminae (mm), Recrystallized, Mineralized Fractures	Planktonic Foraminifera	0.57 (n=2)	1.18	2.10	32.68	7
8	Massive to Bioturbated Claystone (Volcanic Ash)	Greenish Grey to Pale Olive	43.83 (n=4)	6.38 (n=4)	30.98 (n=4)	Massive Bedded, Localized Bioturbation	NA	NA	NA	NA	NA	0

Figure 3.11. Facies identified on Eagle Ford Cores including sedimentological characteristics, grain constituents and average total organic carbon (TOC) associated with each facies. All properties are based on average of measured properties obtained from 4 wells (Workman, 2013).

Figure 3.11 shows the facies identified by Workman, 2013 in the cores obtained from these wells based on the texture, grain types, sedimentary structures, diagenetic features, biotic content and color. They then correlated these facies based on changes in sea level.

Facies	Bulk Density	Matrix Permeability	Gas-filled Porosity	Gas Saturation		TOC	
#	(g/cc)	(nD)	(%)	(%)	No.	(%)	No.
1	2.51	1.94	2.61	26.11	10	3.29	8
2	2.43	2.35	3.28	32.02	25	3.71	38
3	2.55	1.70	2.67	49.49	15	2.46	12
4	2.52	5.85	4.46	54.11	2	0.82	16
5	2.57	1.11	2.77	47.73	2	1.89	1
6	2.61	0.24	2.19	46.74	4	0.98	13
7	2.56	1.18	2.10	32.68	7	0.57	2

Figure 3.12. Primary facies classification based on density, permeability, porosity and total organic carbon from core analysis. Facies with high porosity, permeability and TOC are has high reservoir potential (Workman, 2013)

Figure 3.12 shows the succession of these facies after accounting for uniform sedimentation/subsidence. autogenic sedimentation influences These facies succession is later correlated on well logs. Figure 3.13 shows the sequences identified on well logs. Sequences show a progressive decrease in gamma ray and density porosity towards the top of sequences; whereas bulk density increases upwards.

Workman, 2013 have used density porosity curves (a decreasing upward trend) and gamma ray log to identify the sequences (Figure 3.14). High cyclic packages are identified with the help of spikes in gamma ray and the sequences are identified with low gamma ray and high density values.

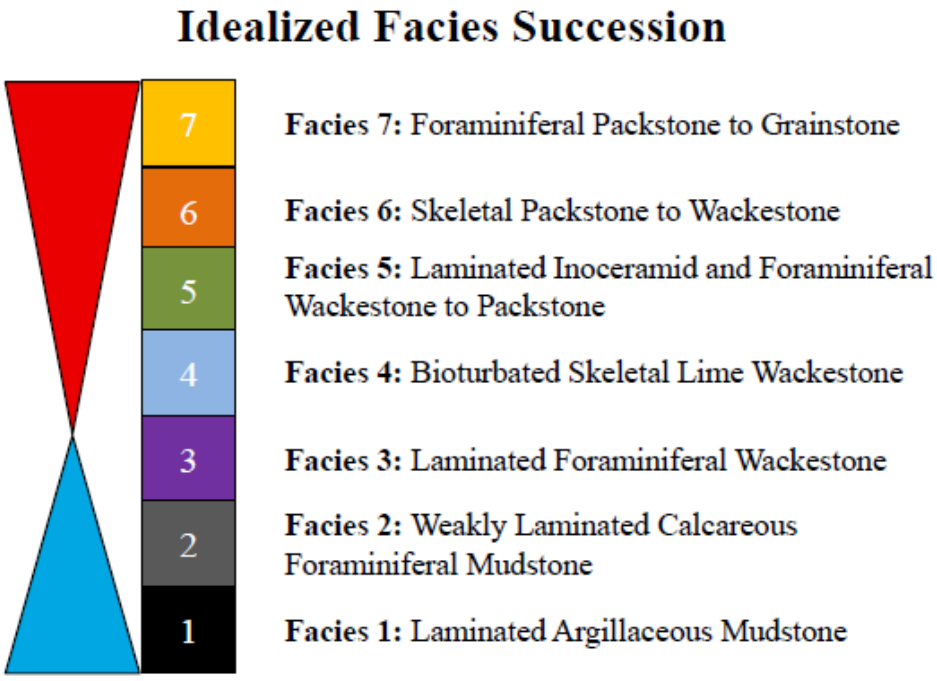

Figure 3.13. Idealized shallowing-upward facies succession observed in Eagle Ford section. Shown are the anticipated facies stacking patterns giving uniform sedimentation/subsidence, changes in relative sea level, and not accounting for autogenic sedimentation influences (Workman, 2013).

Here, sequences are identified with the help of gamma ray, density porosity and bulk density logs. The Sequences show a progressive decrease in gamma ray and density porosity towards the top of sequences; whereas bulk density increases upwards (Figure 3.14). A total of 3 sequences are identified within the EFS section and are referred to as S1, S2 and S3 or lower, middle and upper EFS respectively. This is further discussed in detail in the stratigraphic and structural framework section of this chapter of the thesis (section 3.4.3).

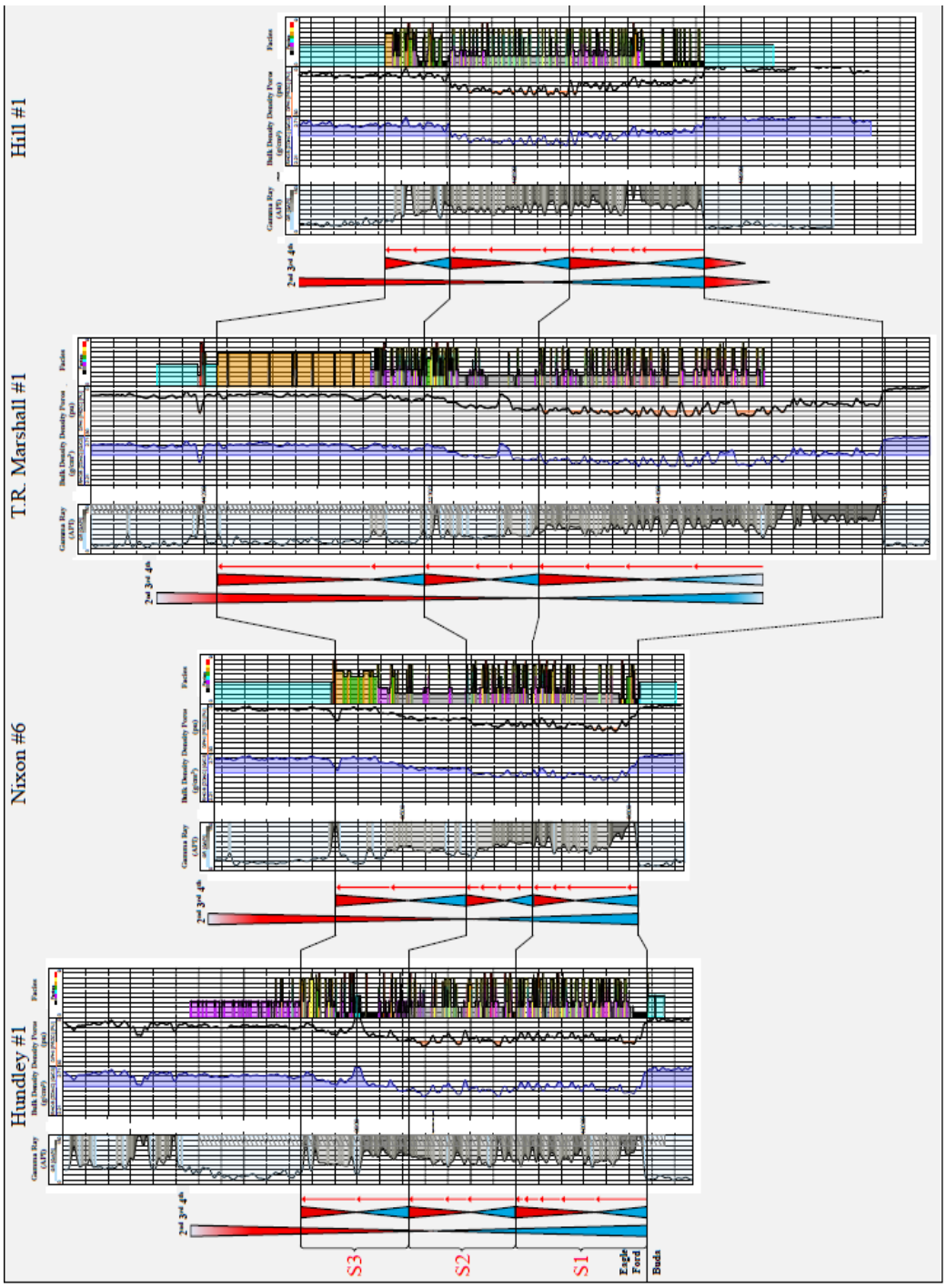

Figure 3.14. Cross section of 4 cores used for analysis. Cross section of all cores show 3rd order sequences (S1, S2 and S3) and second order high frequency (4th order) sequences on conventional wireline logs (gamma-ray, bulk density and density porosity). Sequences show a progressive decrease in gamma ray and density porosity towards the top of sequences; whereas bulk density increases upwards. On track from left to right (gamma ray, bulk density, density porosity and facies). (Workman, 2013)

Figure 3.12 summarizes the final facies based on bulk density, matrix permeability, porosity and total organic carbon (TOC) by (Workman, 2013). A total of 7 facies are identified. Facies with higher measured porosity, permeability and total organic carbon (TOC) are identified as productive facies.

Similar to the methodology described by Workman, 2013, an attempt is made in this thesis to identify the rock types in the area of interest. However, all the values used by (Workman, 2013) are based on core analysis. As no core data and correlation with depositional environment is made, and the classification is based solely on the basis of well logs, instead of facies, term rock types is used.

Table 3.1. Bulk density and density porosity ranges for 4 rock types defined in the thesis. Rock type 1 shows a high porosity moderate density implying a porous but less brittle rock. Rock type 2 shows high density moderate porosity. Rock type 3 and 4 show very low porosity and are possibly nonproductive intervals sandwiched inside the productive intervals.

Rock Type (RC)	Bulk Density (gm/CC)	Density Porosity
1	2.50-2.64	2.2-6.5
2	2.64-2.682	0.6-3.0
3	2.68-2.72	0-0.8
4	2.6-2.7	0-3.5

To identify different rock types a cross plot of density porosity and bulk density is made. Only bulk density and density porosity curve is used because the matrix permeability used by Workman, 2013 is core derived. As no permeability log is available, matrix permeability is not used to identify the rock types. Also, gas saturation used by

Workman, 2013 is core derived. The gas saturation values in the core experiments are on a higher side as the sample is crushed during the experiment. Hence, gas saturation is also not used to classify the wells.

Figure 3.15, shows the results of bulk density and density porosity cross plot. All data points in the zone (EFS top to EFS bottom) are used for analysis. It can be seen from the cross plot 4 different clusters can be identified on the cross plot. The range of values of bulk density and density porosity of these clusters is summarized in Table 3.1.

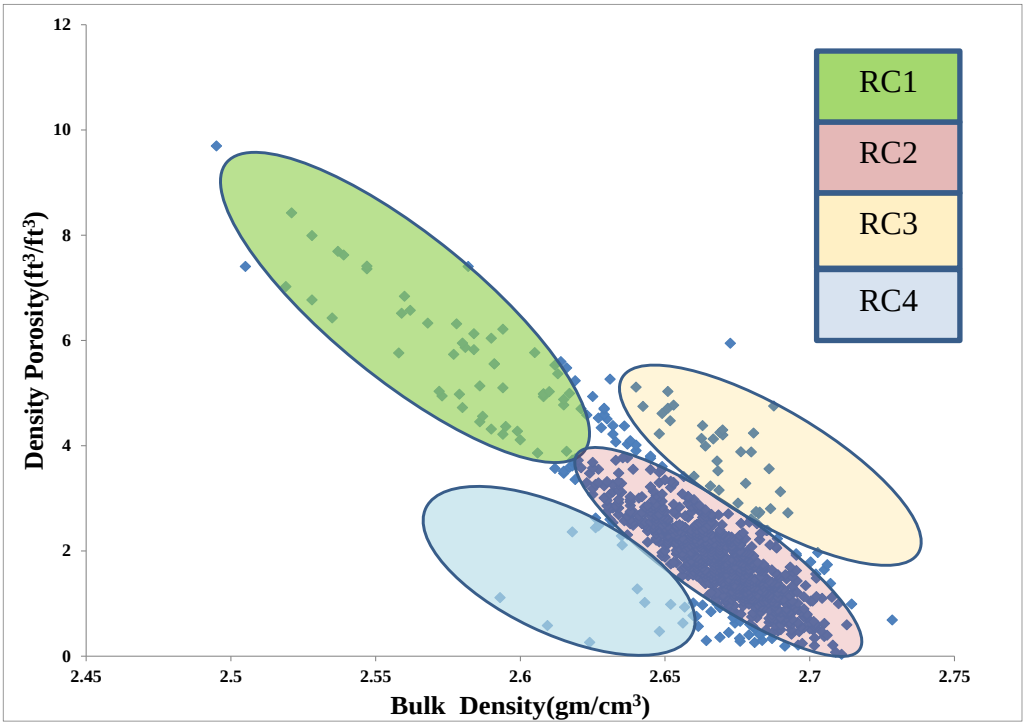

Figure 3.15. Cross plot for density porosity vs bulk density. A total of 4 clusters can be identified on the plot and are referred as rock type 1-4 in this thesis. Rock type 1 and 2 are most prominent in the dataset. Density porosity and bulk density values from all wells in Eagle Ford section is used to make the cross plot.

From the cross plot it can be observed that rock type 2 is predominant rock type followed by rock type 2. Rock type 3 and 4 occur as small scale heterogeneities all across the reservoir. These rock types are also represented in the rock type log identified on our 4 pilot well logs. Figure 3.17 shows a cross section of these rock types in the wells. It can be seen that only rock type 1 and 2 are continuous and can be observed on all wells. Rock type 2 and 3 exist as small scale heterogeneities across all wells in all zones. This can also be seen on both the cross plot as well has the rock type distribution histogram (Figure 3.16).

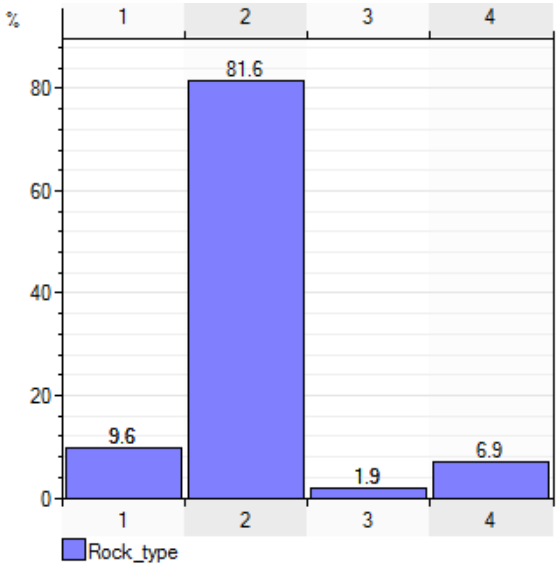

Figure 3.16. Rock type distribution across the reservoir. Rock type 1 and 2 are prominent and rock type 3 and 4 exist as small scale heterogeneities.

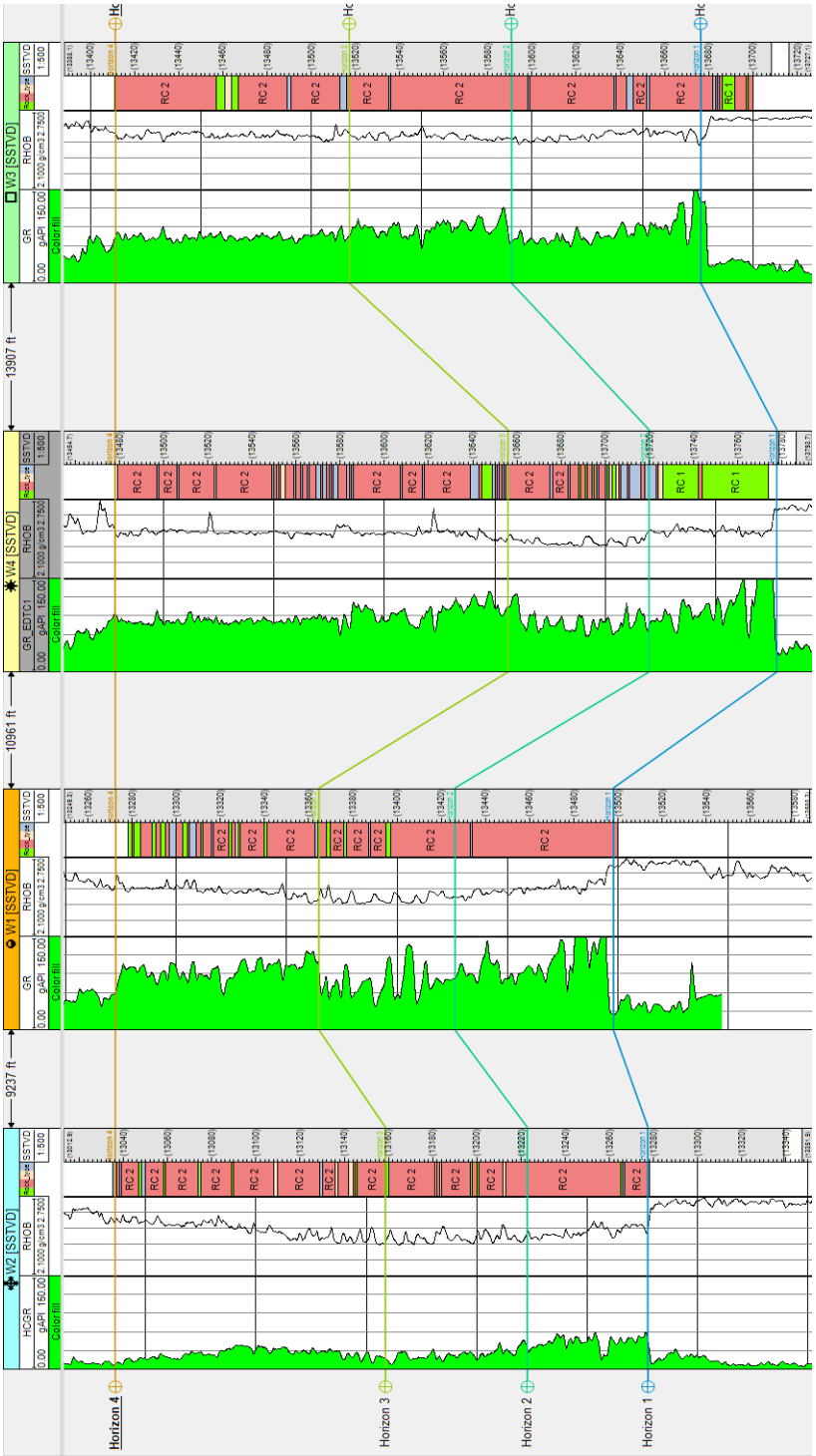

Figure 3.17. Cross section for 4 pilot well logs in the study. It can be observed from the cross section that rock type 1 and 2 are more continuous and are observed on all the wells in all zones. However, the rock type 3 and 4 occur as small heterogeneities across all well logs. From left to right on the plot: Gamma ray log (0-150 API), bulk density (2.1-2.75 gm/cc) and rock types. Color associations for the rock type is same as figure 3.15.

Well 3 and 4 show a significant amount of rock type 1 in lower EFS but same is not observed in well 1 and well 2. In general, all wells are show a highly heterogeneous rock type distribution in upper and middle EFS but lower EFS is less heterogeneous in nature.

From previous experience in the field, it is known that the lower EFS is more prolific than upper and middle EFS in this area of the field. This suggests that small scale heterogeneities may be a major production bottleneck in EFS. Also, the heterogeneity is introduced by rock type 2 and 3 which are most likely the non-productive rock types. This also suggests that a small amount of nonproductive rock types may affect the production considerably.

3.4.3. Stratigraphic and Structural Framework

To model the structural characteristics and variability of the lithology across the area of interest (AOI) a detailed 3D lithological model is built. For the purpose of modeling, only well logs are available.

Out of 5 pilot wells, detailed well log suit is available only for 4 wells in the section. Figure 3.18 shows the gamma ray log and the bulk density plots from 4 pilot well logs provided by the operator. Three sequences S1, S2 and S3 or lower, middle and upper EFS can be identified on the gamma ray and bulk density logs. Bulk density first decreases and then increases from top of EFS (horizon 4) towards bottom of EFS (horizon 1). Sharp spikes in gamma ray values indicate high cyclic packages (Workman, 2013).

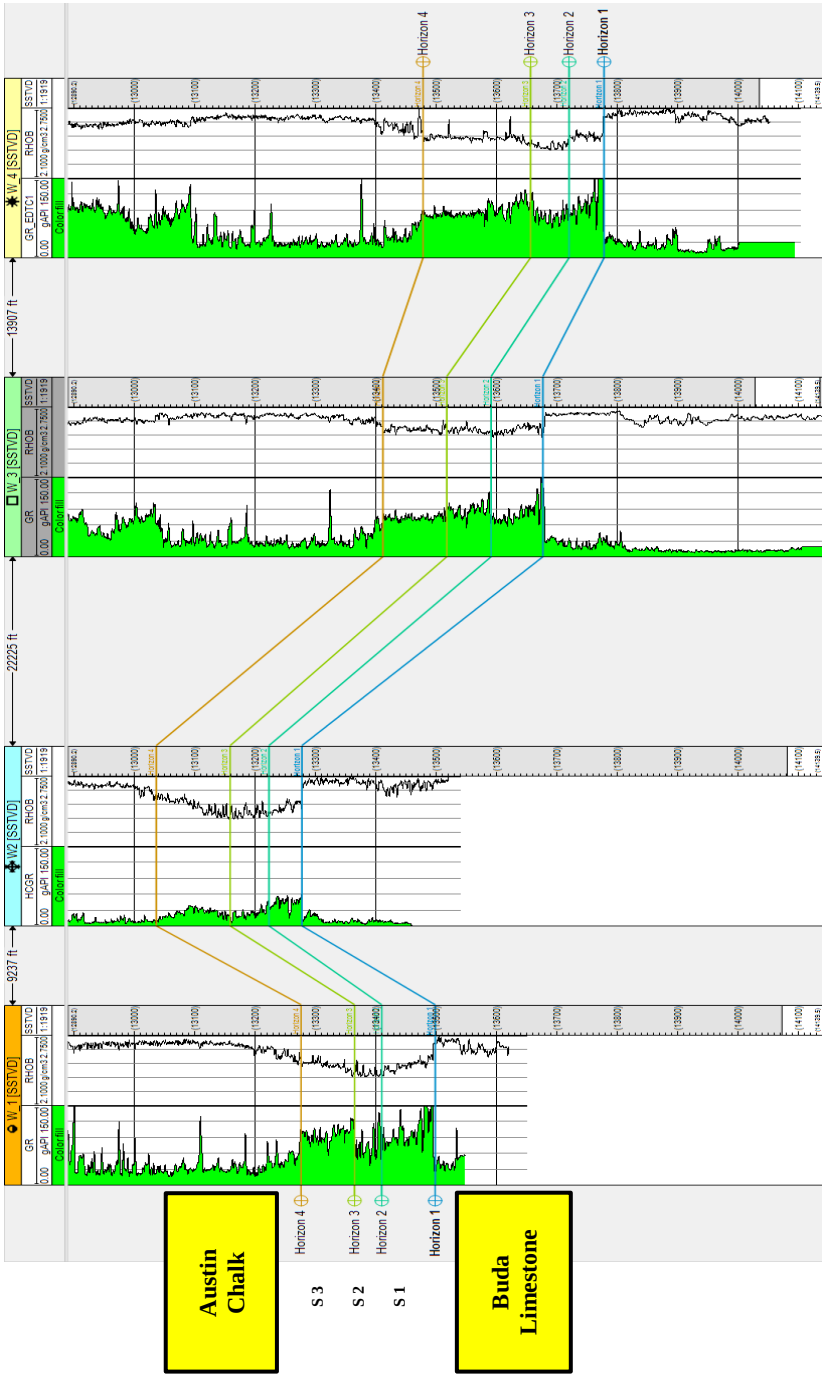

Figure 3.18. Cross section of 4 wells (W1-W4) on gamma ray and bulk density. Sequence 1(S1), Sequence 2(S2) and sequence 3(S3) can be identified on the gamma ray and bulk density log. Bulk density first decreases (transgressive phase) and then increases (regressive phase) from top of EFS towards bottom EFS. Spikes in gamma ray suggest High cyclic packages. Horizon 1 is the top of Buda limestone and Horizon 4 is the top of EFS. From left to right on track: Gamma ray (0-150 API), Bulk Density (2.1-2.75 g/cm^3).

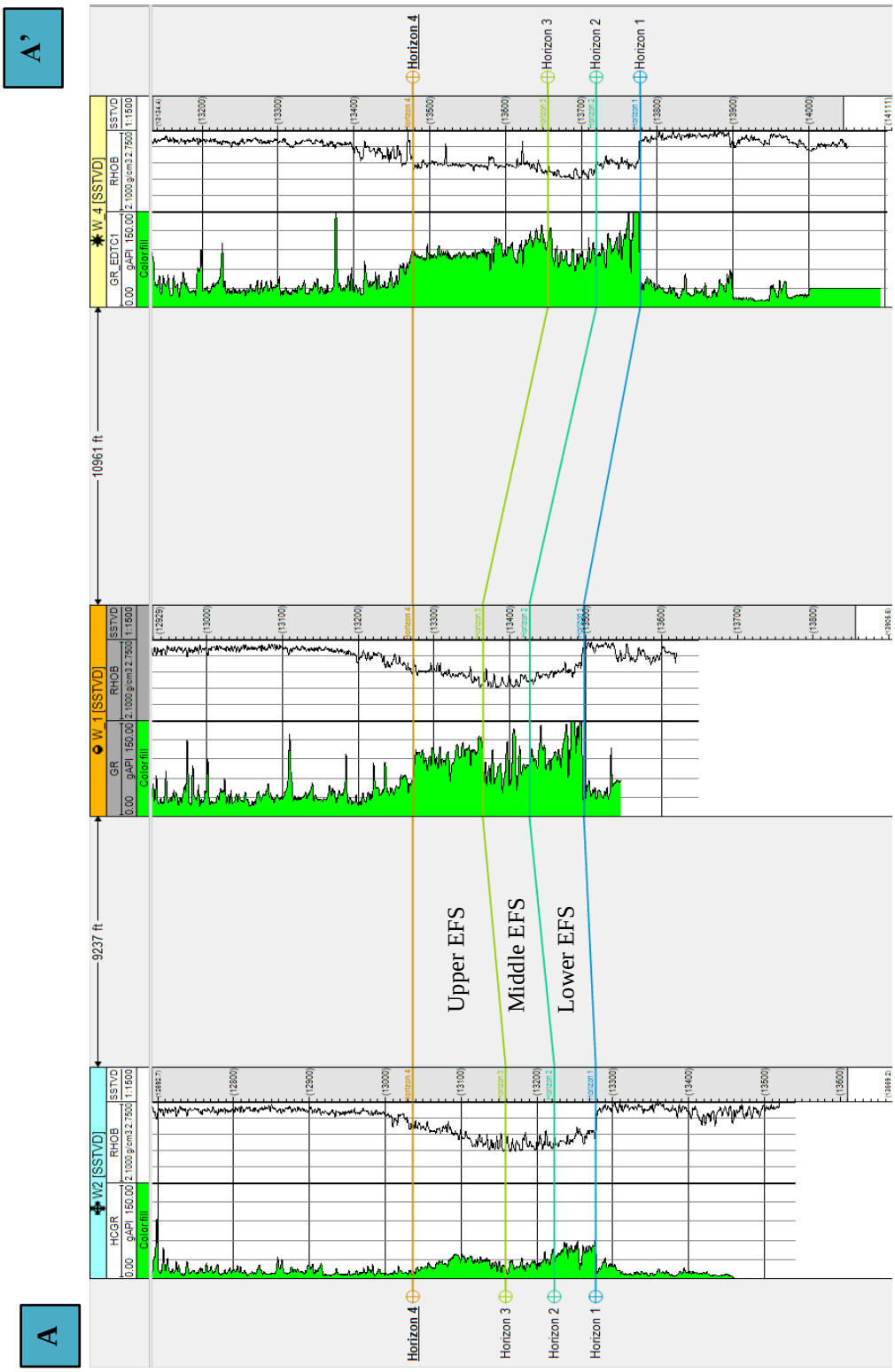

Figure 3.19. Stratigraphic cross section A to A' (north to south) flattened on the top of EFS. Well logs suit consists of gamma ray and bulk density logs. Upper Eagle Ford gets thicker towards south however thickness of lower and middle Eagle Ford remains fairly consistent.

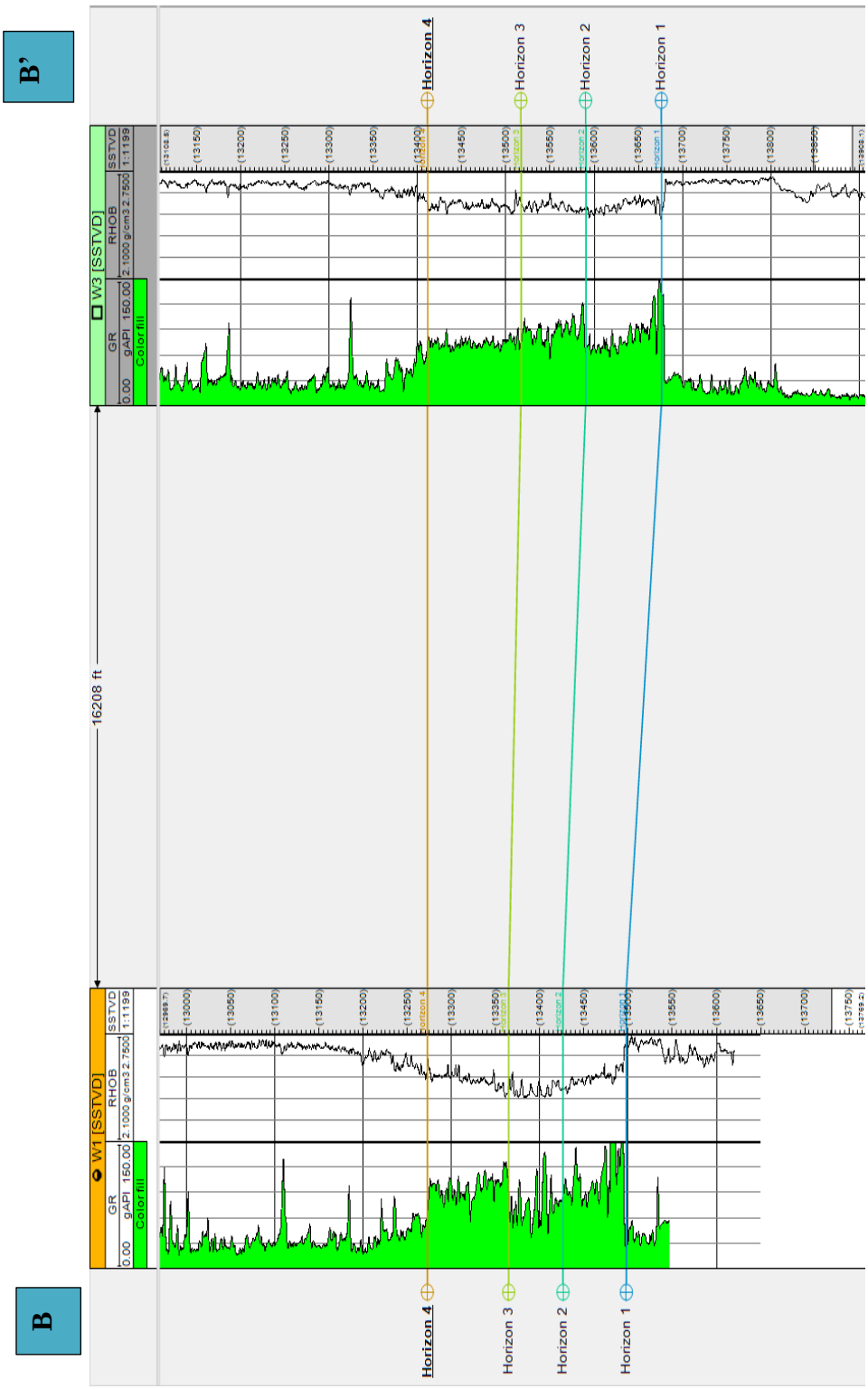

Figure 3.20. Stratigraphic cross section B to B' (West to East) flattened on the top of EFS. Well logs suit consists of gamma ray and bulk density logs. Thickness of the formation is fairly consistent.

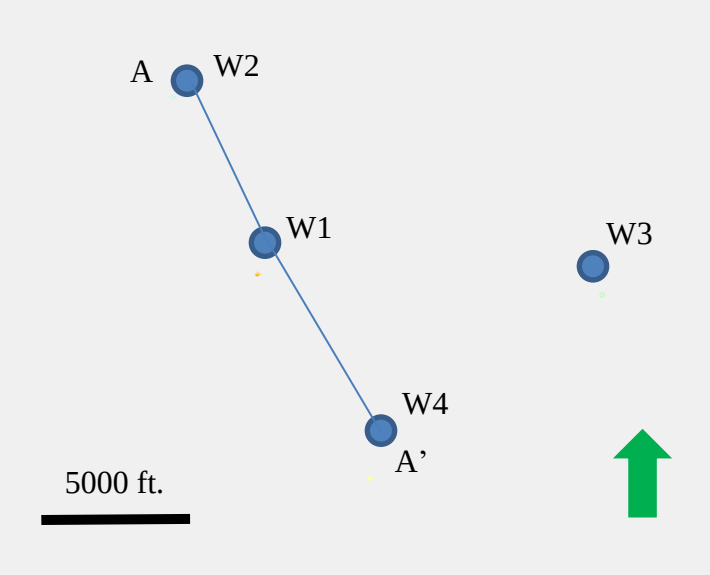

(a)

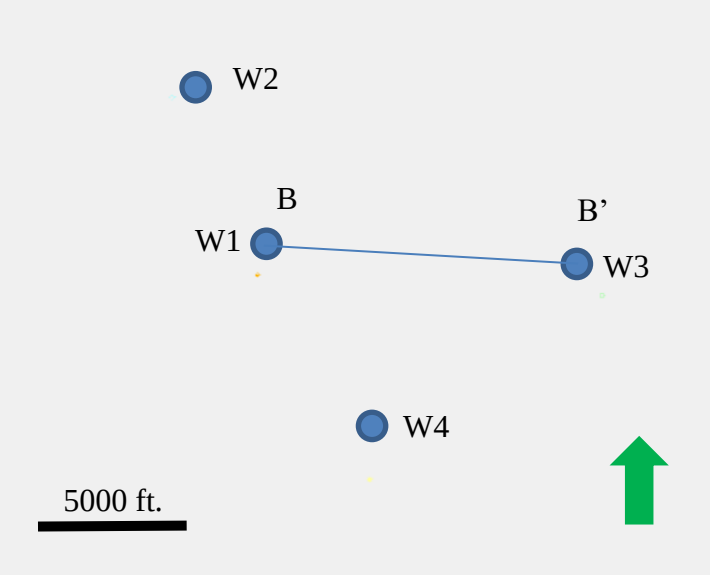

(b)

Figure 3.21. Well selection for stratigraphic cross-sections (a) A-A’ (N-S), and (b) B-B’ (W-E)

Generating probability maps for rock types

As no 3D seismic data is available for analysis, to generate the probability maps for all the rock types following procedure is followed:

(a) First the thickness of all rock types (RC1- RC4) is mapped in all intervals (upper, middle and lower EFS). This is done in Petrel® by attribute operation. The results are illustrated in Figures 3.22 and 3.23. The figures show the thickness of all rock types in all zones. The thickness in every zone is averaged using the method "most of".

(b) These averaged thickness of all rock types in different intervals are mapped across the reservoir. This is done by taking the thickness of every rock type in every zone and then converting them to points. This thickness is then used to make a rocktypewise thickness probability map in each zone.

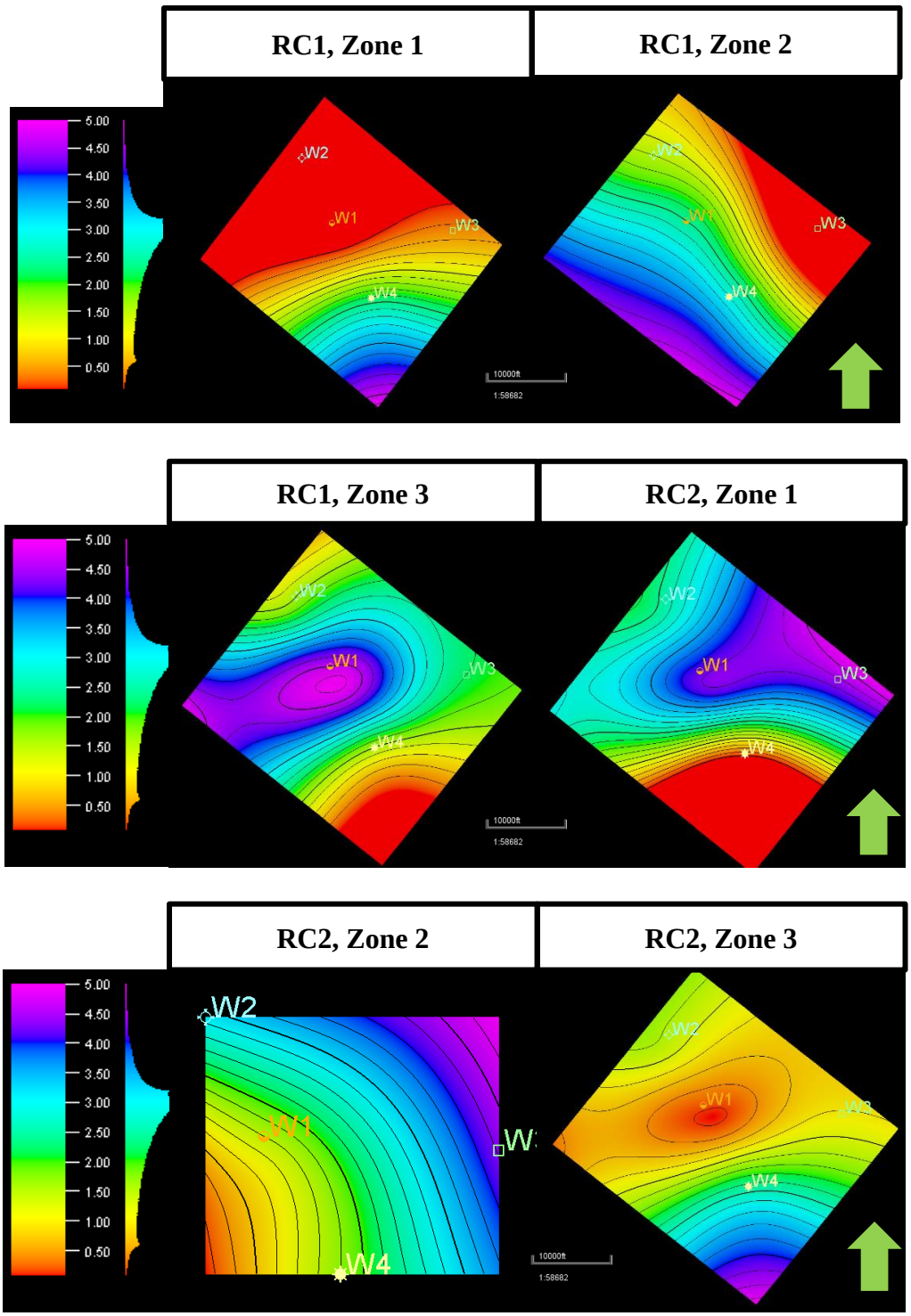

Figure 3.22. Rocktypewise thickness probability map for rock types 1 and 2 in all zones. Rock type 1 and 2 are predominant, a trend can be observed and hence variograms are assigned in the direction of the maximum heterogeneity.

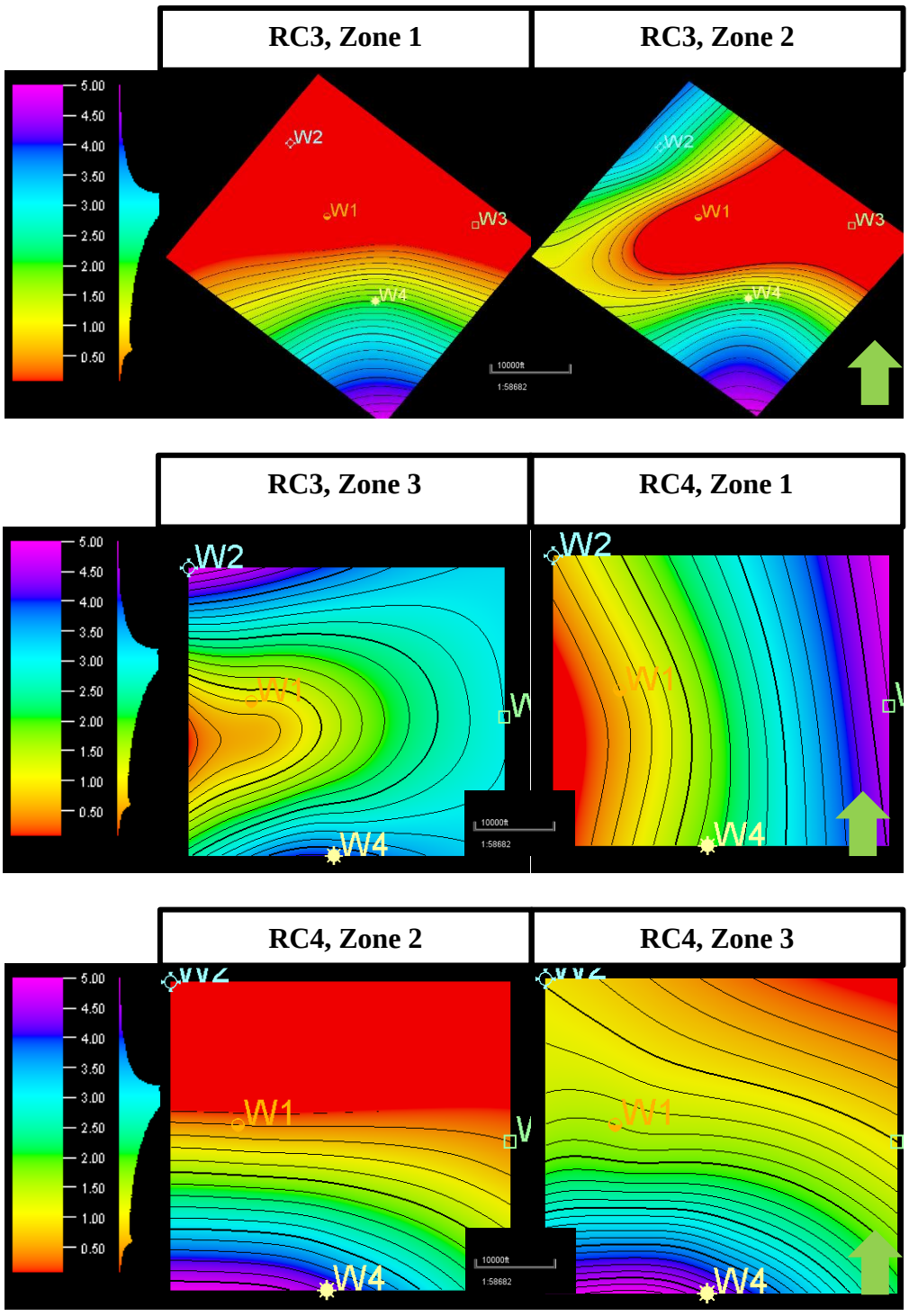

Figure 3.23. Rocktypewise thickness probability map for rock types 3 and 4 in all zones. For discontinuous rock types i.e. rock type 3 and 4 a trend is not observed and it is more difficult to assign the variograms. All variograms are assigned in the direction of the maximum heterogeneity.

Assigning Variograms

Based on the probability maps generated previously, variograms are assigned in horizontal and vertical directions. An example variogram in horizontal direction for rock type 1 (RC1) in zone 1 is demonstrated in Figure 3.24. Variogram is assigned in the direction of maximum variability. All rock types are modeled with the help of exponential variograms.

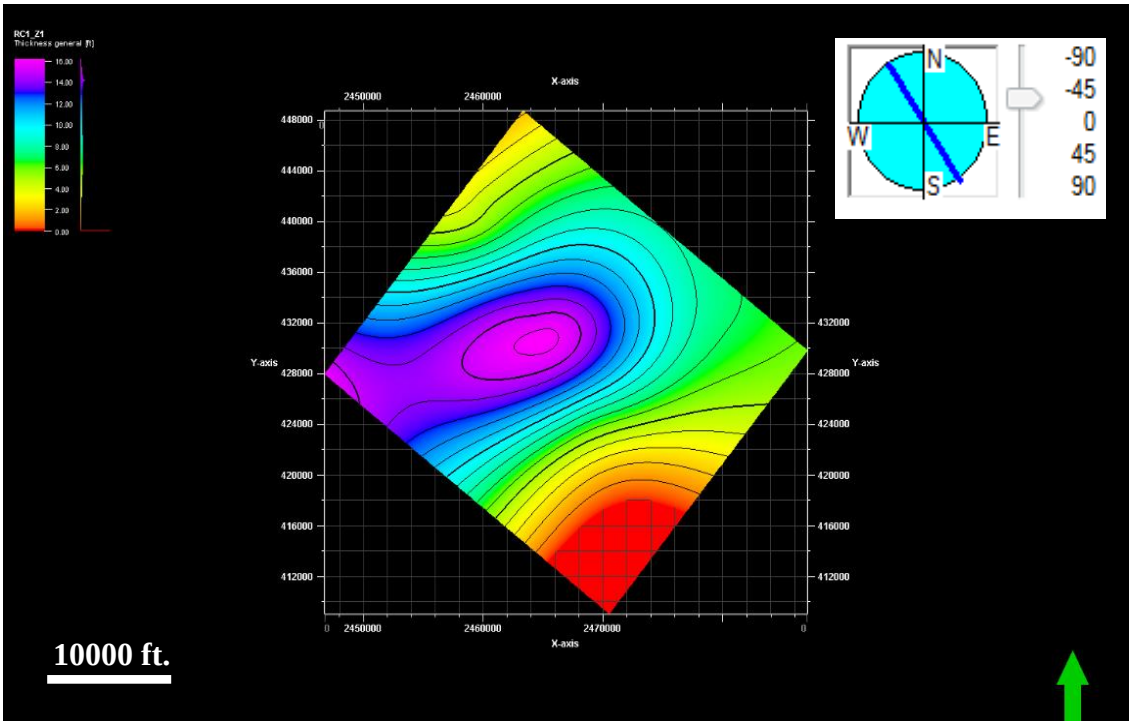

Figure 3.24. Example variogram for rock type 1 in zone 1. The direction of variability is represented by the azimuth. Variograms in this particular case is set as major=minor = 4227 Ft. with a sill of 1.0048.

Vertical variograms are assigned with the help of the well logs and an example for RC1 in zone 1 is demonstrated in Figure 3.25 for all zones and all rock types.

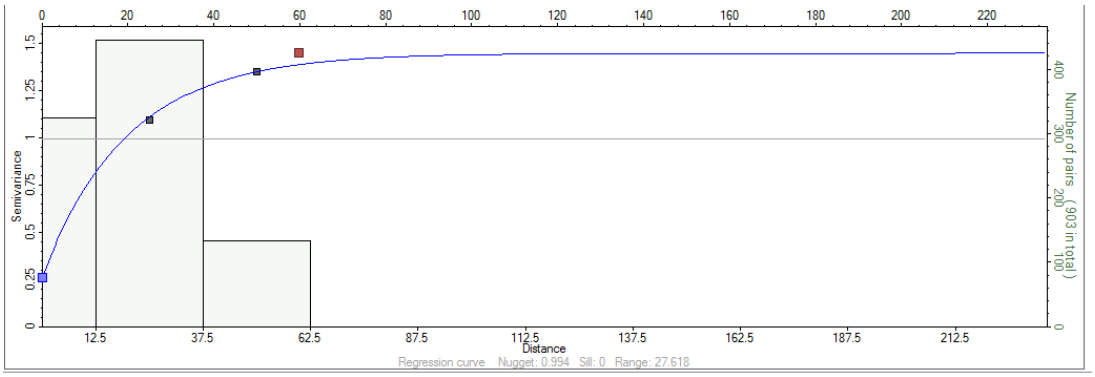

Figure 3.25. Vertical variogram for RC 1 in zone 1. Exponential variograms are used for modeling. Nugget= 0.994, Range=27.6.

Table 3. 2. Variogram selection on the basis of probability maps for all zones and rock types. For rock type 3 and rock type 4, in some zones a default value of 500 ft is given as these rock types do not show any trend in some zones.

Zone	Rock Type	Variogram Model Type	Major Range(ft)	Minor Range (ft)	Vertical Range(ft)	Azimuth (deg)	Sill
1	1	Exponetial	4227	4227	27.6	-32	1.06
	2	Exponetial	5654	5654	49.563	-22	1.02
	3	Exponetial	563	563	24.53	0	1.16
	4	Exponetial	500	500	48	0	0.95
2	1	Exponetial	500	500	76	0	1.07
	2	Exponetial	6700	6700	51.251	0	1.17
	3	Exponetial	500	500	32.754	0	0.95
	4	Exponetial	600	600	51.13	0	1
3	1	Exponetial	1000	1000	49.66	0	0.31
	2	Exponetial	5500	5500	33.264	0	0.18
	3	Exponetial	500	500	39.8	0	1
	4	Exponetial	500	500	38.53	0	0.27

Spatial distribution of lithology

To distribute the rock types across the reservoir, Sequential Indicator Simulation (SIS) is used to construct the 3D lithological model. Corner point gridding is used for the gridding purpose to honor the geometry of the problem. A grid size of 70 ft. is chosen to honor the completions as perforation cluster spacing is 70 ft. This way one perforation can be inserted every grid block later for simulation purpose. Also, the minimum well distance is 500 ft. hence the grid size is optimally able to model the lithology (2*70 =140 Ft. < 500 Ft.)

Based on the 4 rock types first three zones are made inside the Eagle Ford interval as; upper, middle and lower EFS respectively. The zones are made by the Zone-Index method in Petrel®.

The middle Eagle Ford is the thinnest interval followed by the upper and lower EFS. The zones are then subdivided into sublayers such that the smallest rock type in every zone can be represented in the final model. Figure 3.26 demonstrates the process of layering in each zone. First the initial rock type log is upscaled using the “most of” scheme and then an iteration on number of layers is carried out. Figure 3.26 shows the results of layering scheme of 50, 25 and 50 layers each in upper, middle and lower EFS which is obtained after multiple iterations on number of layers which preserves the smallest scale heterogeneity.

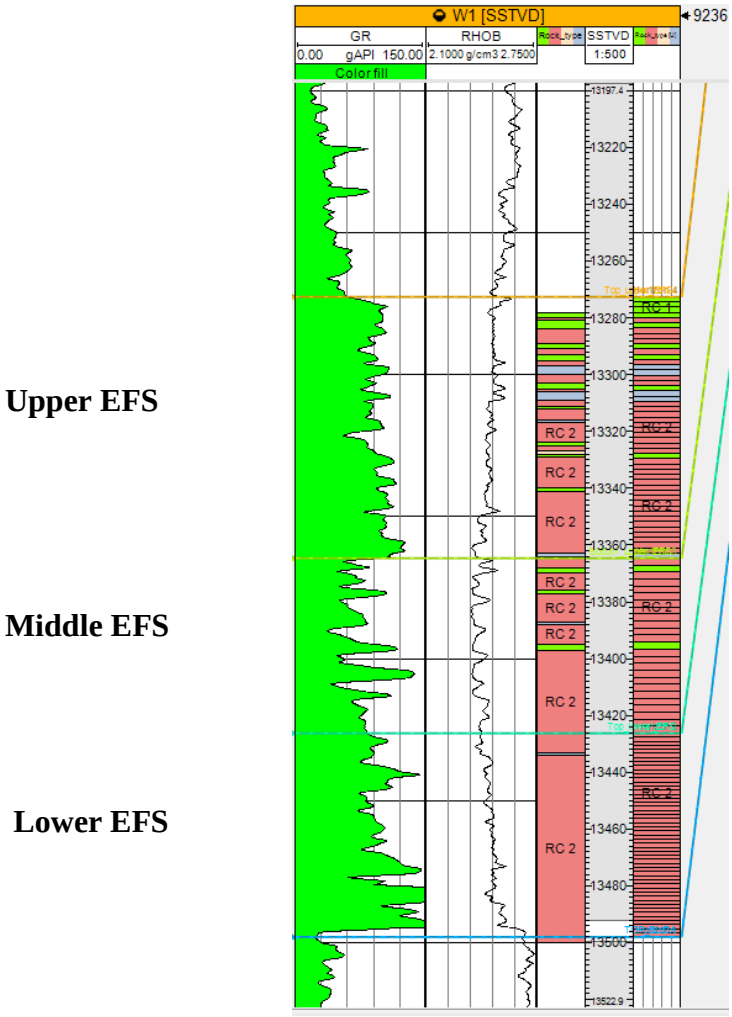

Figure 3.26. Final layering scheme for one well (W1) used after multiple iterations. From left to right on track: gamma ray, bulk density, initial rock type log, upscaled rock type log. It can be observed that using the layering scheme of 50, 25 and 50 proportional layers in upper middle and lower EFS, all rock types can be observed in the upscaled log.

Once, the layering is fixed all zones are modlled with sequential indicator simulation (SIS). The final model is shown in figure 3.27.

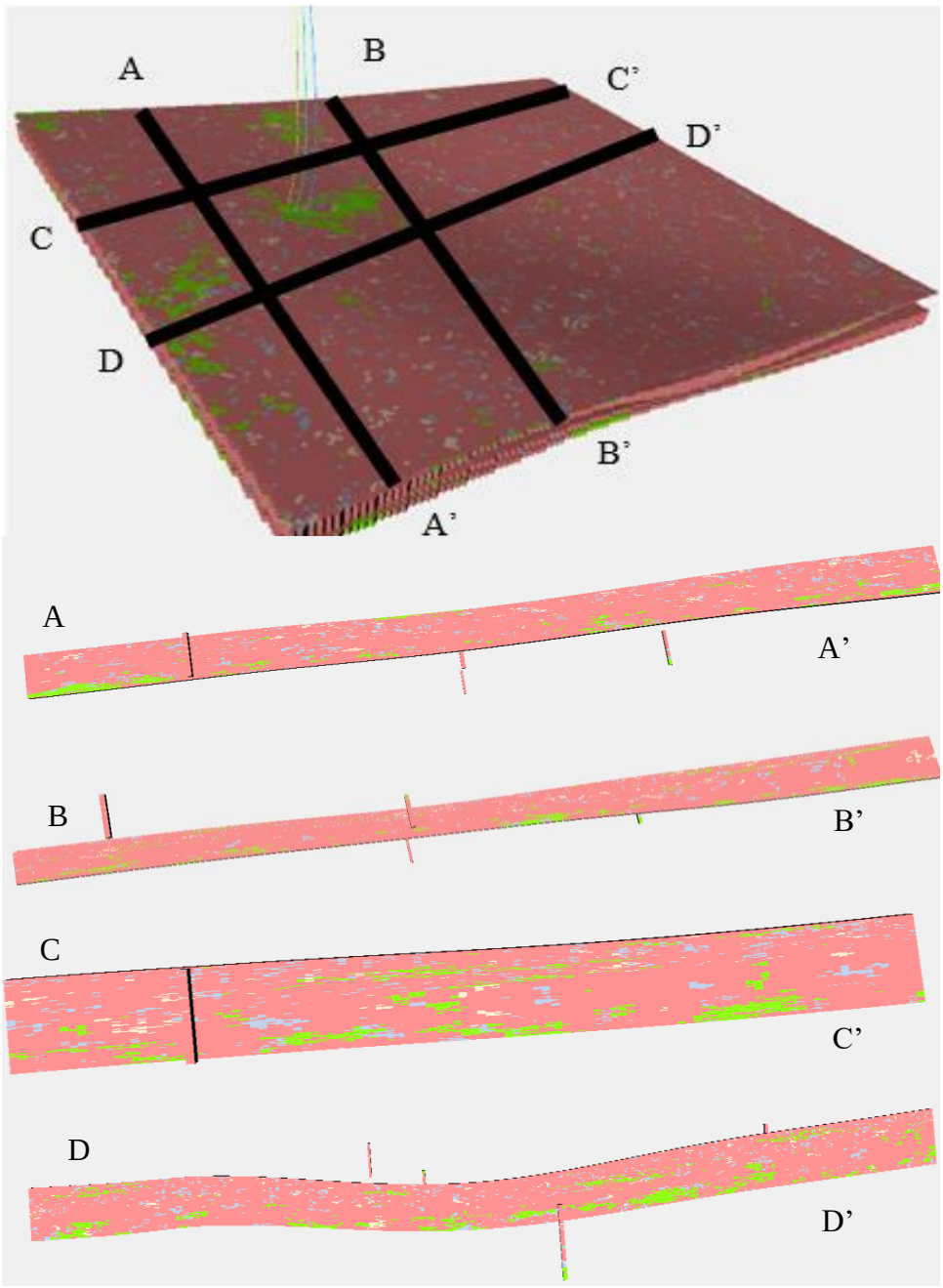

Code	Name	Parent	Background	Lines	Pattern
1	RC 1				
2	RC 2				
3	RC 3				
4	RC 4				

Figure 3.27. 3D lithology model with north-south and east-west cross section. Rock type 1 and 2 are predominent in lower Eagle Ford. Non- productive rock types (RC3 and 4) are present in middle and upper Eagle Ford. Color associations are consistent with the rock typing from the previous section.

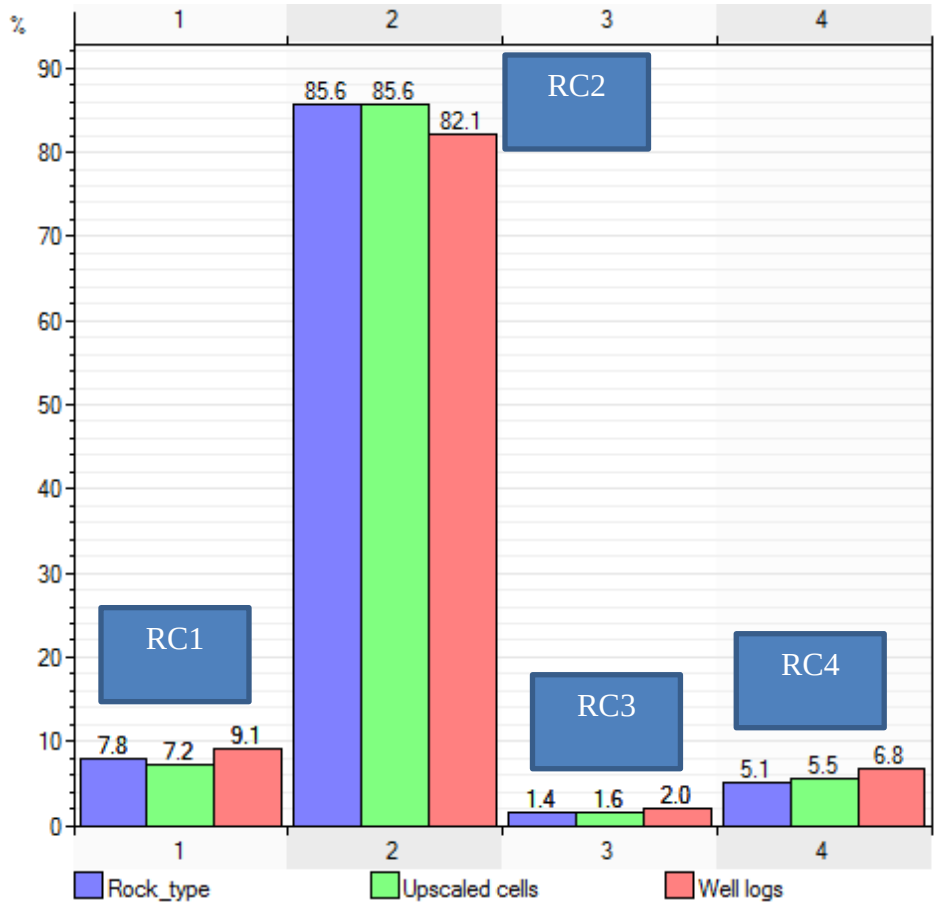

Figure 3.28. Percentage of ech rock type from the original well logs and the sequential indicator simulation with the layering scheme of 50, 25 and 50 proportioanl layers in upper, middle and lower Eagle Ford. It can be seen that the percentage of facies is preserved.

3 D distribution of porosity, permeability and water saturation

The porosity, water saturation and permeabilty logs are then upscaled. All logs are upscaled based on the rock types using the arithmatic average. Figure 3.29 shows the upscaled porosity and water saturation and original well logs. It can be observed that the upscaled well logs represent the original properties very well.

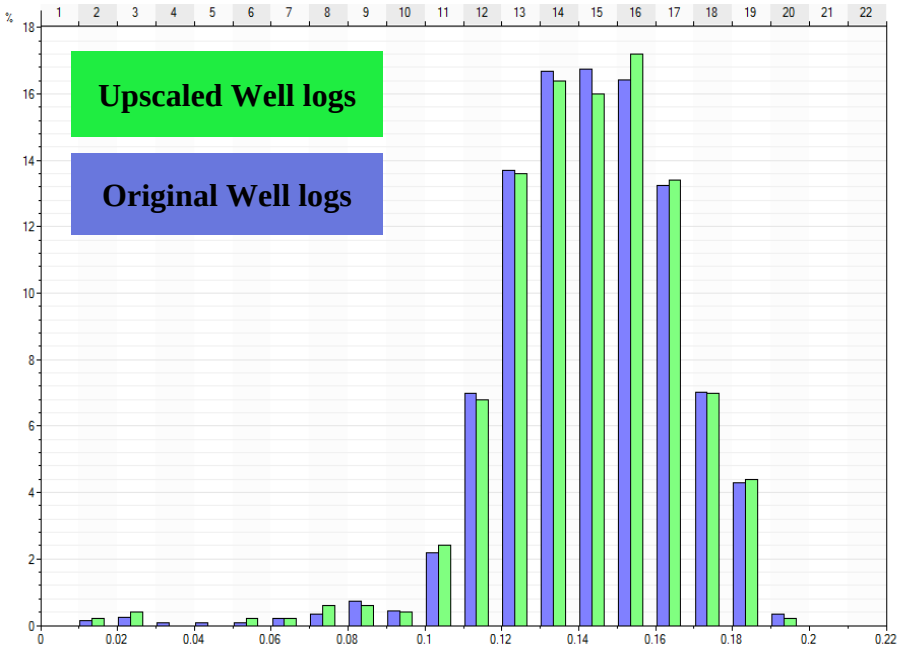

(a)

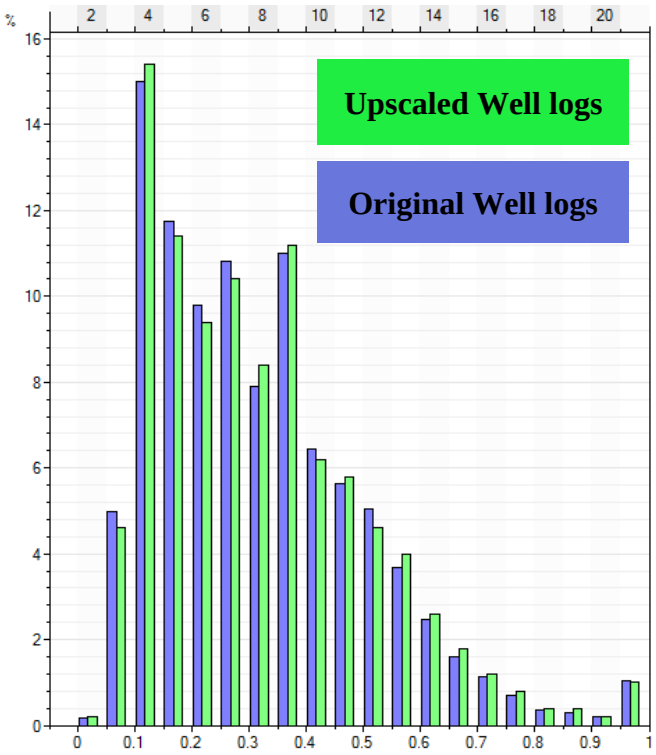

(b)

Figure 3.29. Upscaled and orginal well logs from using "arithmatic average" upscaling. On the left is the porosity (in fraction) and on the right is the water saturation. It can be seen that the upscaled values match the original well logs closely.

The upscaled well logs are then used to populate the porosity and water saturation in the lithology model. Sequential Gaussian Simulation (SGS) is used for this purpose to honor the upscaled well logs. The variograms are kept the same as the variograms for the rock types (Table 3.2). Therefore, the ranges of the porosity and water saturation remains same as those of the rock types. Figure 3.30 and figure 3.31 shows the 3D lithology constrained porosity and water saturation models.

3.4.4. Final Model Details

The final static model contains 10 million grid cells with a grid cell size of 70 ft. each in x and y direction. Final number of zones are kept at 3 to model upper, middle and lower Eagle Ford Shale (EFS) respectively. Upper and lower EFS zones have 50 layers each and the middle EFS has 25 layers as middle EFS is thinner than upper and lower. With this scheme, we are effectively able to model all small scale heterogeneous rock types present in the reservoir.

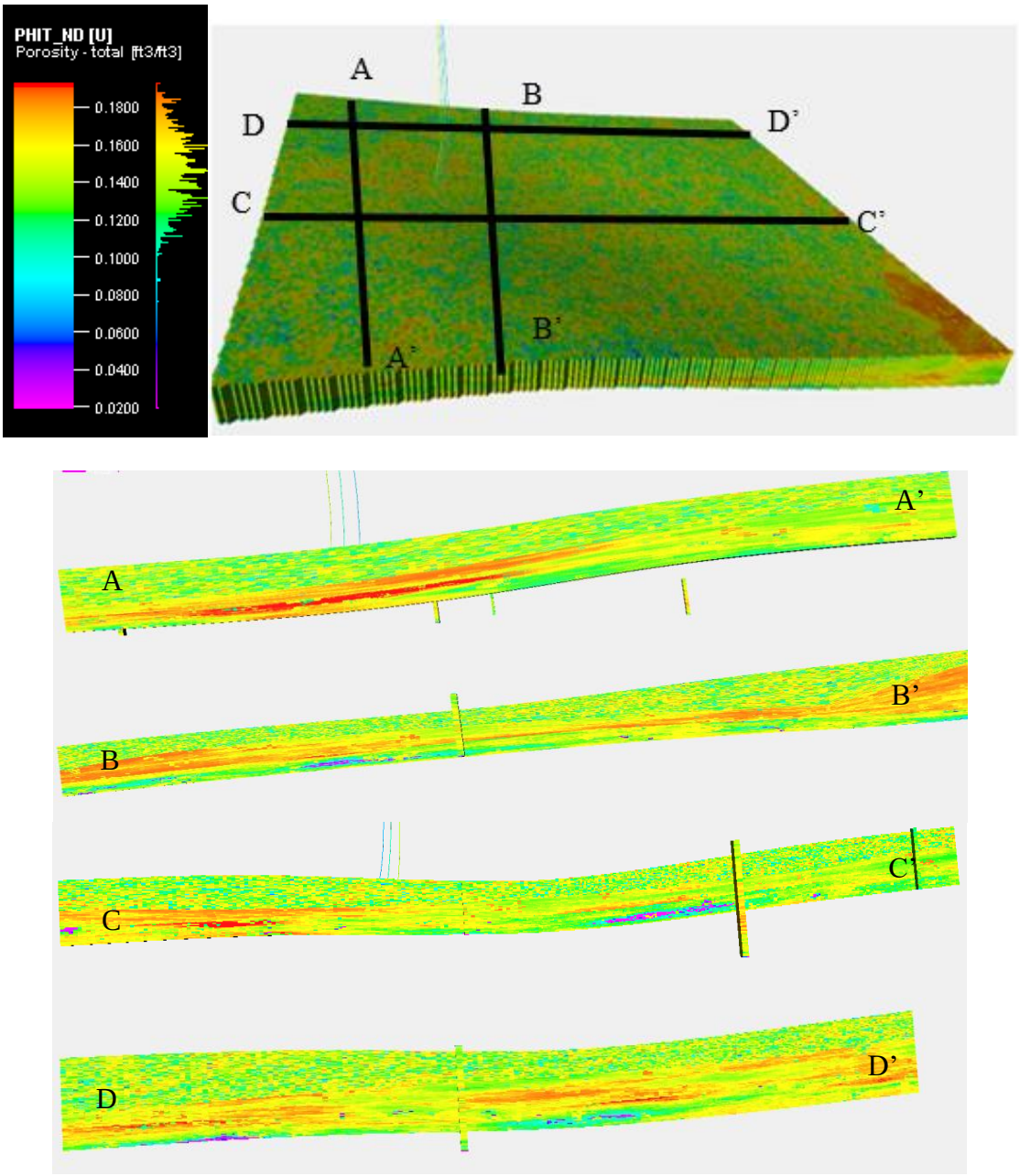

Figure 3.30. Lithology constraint porosity model. Separate cross sections in east west and north south direction show the porosity distribution around the PAD wells in upper, middle and lower Eagle Ford. It can be observed that the lower Eagle Ford shows higher effective porosity than the upper or middle Eagle Ford in the area of interest.

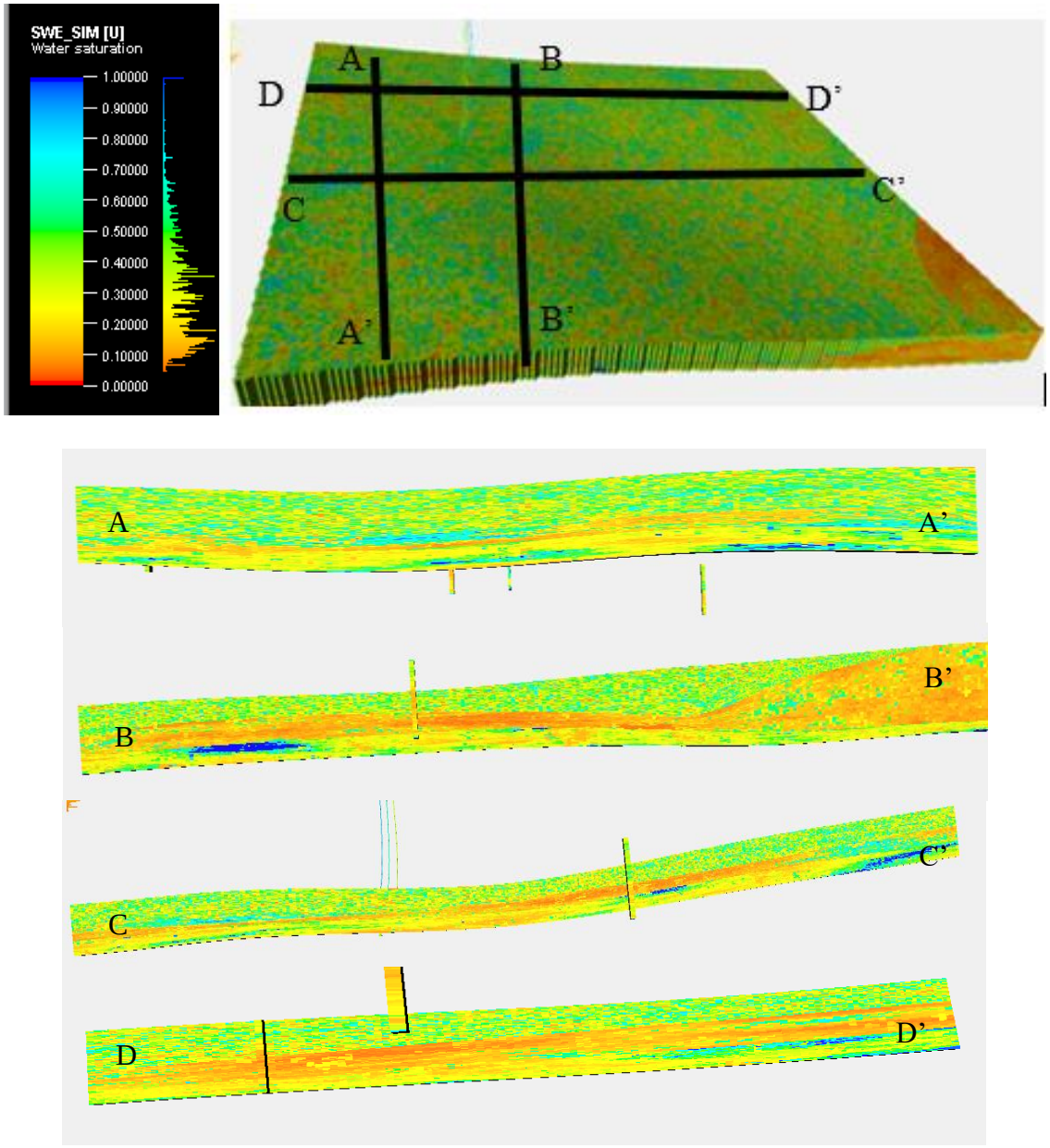

Figure 3.31. Lithology constraint saturation model. Separate cross sections in east west and north south direction show the saturation distribution around the PAD wells in upper, middle and lower Eagle Ford. It can be observed that the lower Eagle Ford shows higher effective porosity than the upper or middle Eagle Ford in the area of interest. Middle Eagle Ford shows especially high water saturation in few areas.

3.5.Fluid Modeling

Once the reservoir characterization was complete, fluid characterization was done. A full pressure, volume, temperature (PVT) study was provided by the operator. Platform used for fluid modeling is PVTP®. Due to confidentiality of the dataset a full composition is not published in this thesis. However, the workflow and the key results are described in the following sections.

Fluid modeling dataset components

(a) Full Composition (separator oil and gas) and mathematically recombined composition

(b) Separator liquid Flash

(c) CCE (pressure, relative volume, density, Y function, retrograde liquid volume, gas deviation factor)

(d) Reservoir gas (recombined) depletion study at reservoir temperature (330˚F)

Equation of state modeling procedure

(a) Data quality check

(b) Basic matching like phase envelope and saturation pressure by using 6 pure components and 1 plus fraction

(c) Characterizing the plus fraction under different characterization schemes

(d) Matching lab data with characterized (full) composition

(e) Design the lumping scheme and lumping the characterized sample to preserve the match on lab data

(f) Selecting the final lumped composition with binary interaction coefficients

3.5.1. Data Quality Check

Data QC of the sample is done by using Hoffman plots (Hoffmann, Crump, & Hocott, 1953).The plot utilizes of log (KP) vs with a characterstic b function. Equation 3.22 shows the expression used in Hoffman plot Where K is the equilibrium constant and b is a characteristic Hoffman factor. Equation 3.23 describes the b factor calculation for equation 3.22. T_{ci} and P_{ci} are critical temperatures for every component at initial conditions.

$$\log K_i = A_0 + A_i b \tag{3.22}$$

$$b_i = \left(\frac{\frac{1}{T_{bi}} - \frac{1}{T}}{\frac{1}{T_{bi}} - \frac{1}{T_{ci}}} \right) \log\left(\frac{P_{ci}}{P_{sc}}\right) \tag{3.23}$$

From Equation 3.22 it can be observed that on a semilog plot Ao and Ai are the intercept and the slope of Ki vs b plot. The plot should be more or less a straight line for components C1 to C6. Any gross deviation from the plot implies the X and Y fraction i.e. percentage of the component in liquid and gas phase respectively is suspected and the recombination has to be revised.

Error! Reference source not found.32 summarizes the results from Hoffman plot f rom the recombined sample. From Hoffman quality plot it can be observed that the data points lie more or less on the straight line and hence fluid passes the QC.

The equation of state (EOS) used in the model is Peng Robinson 1978 or PR-78 with volume shift. Volume shift parameter used alongside with PR-78 is a preferred method for modeling gas condensate reservoirs (Izgec & Barrufet, 2005). Equation 3.24 shows the Peng-Robinson EOS used in this thesis to match the experimental data.

$$P = \frac{RT}{v-b} - \frac{a(T)}{v(v+b0+b(v-b)} \tag{3.24}$$

Where, P is the pressure, v is volume $a(T)$ is the attraction term between the molecules which in turn depends on acentric factor. T is the temperature and R is the gas constant.

3.5.2. Tuning of Molecular Weight and Specific Gravity of Plus Fraction

For the purpose of this study 6 pure components and 1 plus fraction(C_{7+}) is used for analysis. The exact composition of the fractions is not published in this thesis. Most common source of error in a PVT report is the plus fraction molecular weight. Hence, even before characterizing the plus fraction into finer components the molecular weight of the plus fraction and /or the specific gravity of the plus fraction needs to be adjusted to match the bubble point pressure and phase envelope.

The fluid saturation pressure could not be replicated with the initial given specific gravity (SG) and molecular weight (MW) of the plus fraction. Hence, the molecular weight of the plus fraction is reduced to match the dew point pressure. It is a general practice to allow 10% deviation from reported MW and/or SG to match the bubble point pressure.

A match in this case obtained by reducing the molecular weight of the fluid by 7 percent keeping the specific gravity of the fluid same. The match obtained and the resultant phase envelop can be seen in Figure 3.33. It is observed that the bubble point pressure of the reported fluid is 4284 Psi which matches well with the adjustment of the molecular weight of the plus fraction.

It is clear from the phase envelope that the at dew point pressure of 4284 Psia, the fluid is a retrograde condensate system as the reservoir conditions lie between critical

point and cricondentherm. This sample is flashed to get an initial match on the separator gas oil ratio's (GOR's) and separator specific gravities (SG's) (exact values of the SG's and separator conditions are not published in this thesis).

Once, the phase envelope is fixed, and an initial match on separator GOR's and SG's is made, plus fraction characterization of the fluid is carried out in the next step.

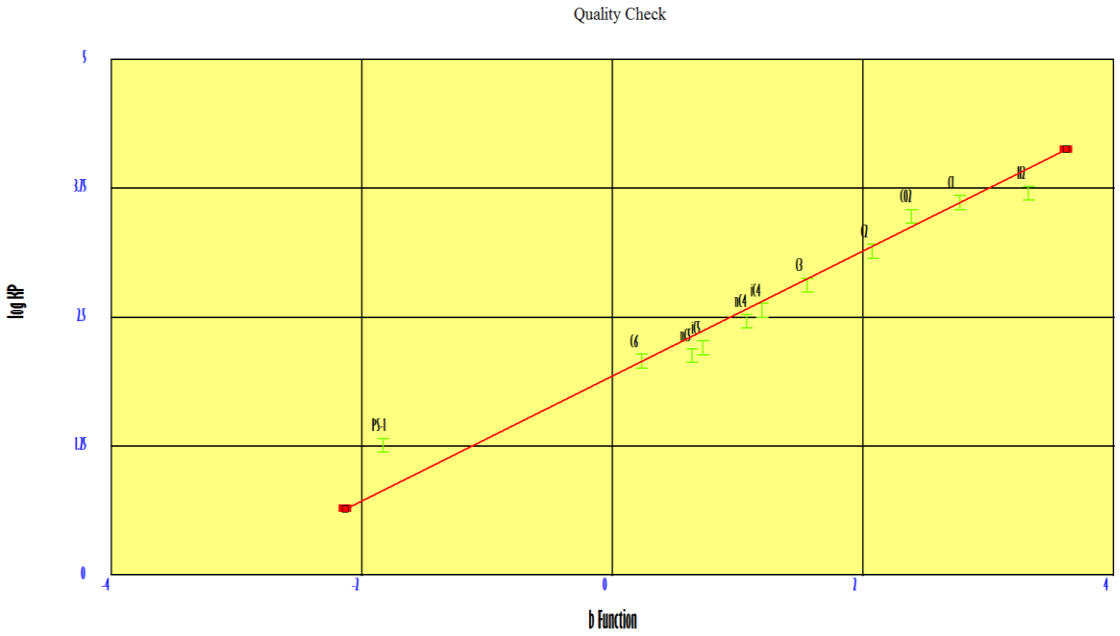

Figure 3.32. Hoffman quality plot. The green markers represent different components from the PVT report and the red curve represents the ideal curve. It can be observed that the components honor the ideal curve and hence fluid passes the quality check.

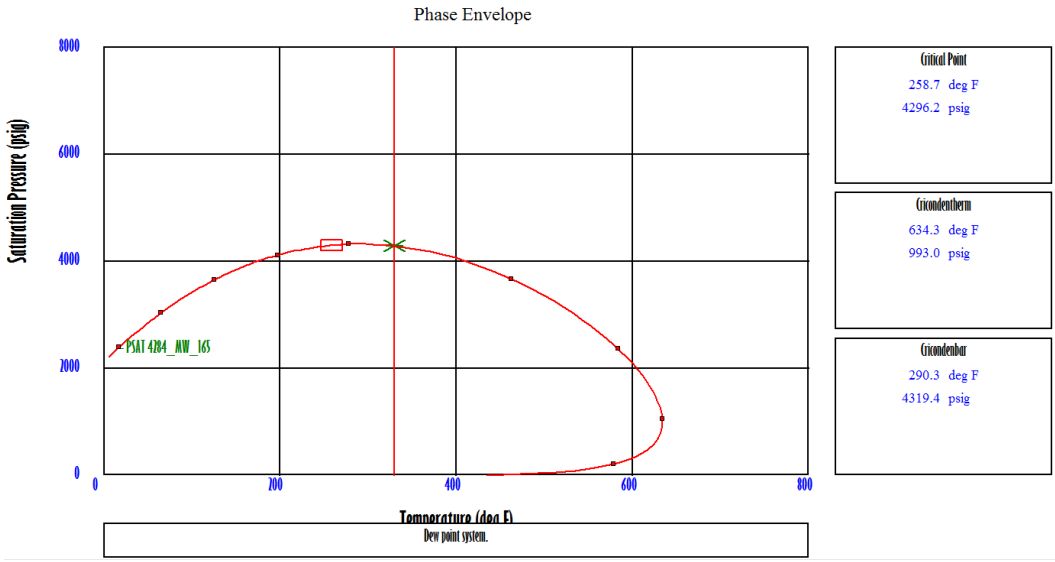

Figure 3.33. Initial phase envelope with 6 pure components and 1 plus fraction. Red curve shows the phase envelope of the fluid system after reducing the molecular weight. On X axis is the reservoir temperature and on the Y axis is the reservoir pressure. Solid vertical red line represents the reservoir temperature of 330-degree F. Green symbol represents the dew point pressure of 4284 Psi and the red symbol represents the critical point of the symbol. As the reservoir temperature lies between critical point and cricondentherm, the reservoir fluid is a retrograde gas condensate system.

3.5.3. Plus Fraction Characterization

After an initial match is obtained on dew point pressure and an initial phase envelope is defined the C_{7+} fraction is splitting is carried out. Plus fraction splitting or plus fraction characterization (Whitson, 1983) is a process of dividing the plus component into finer component bandwidths.

The procedure adopted in this study for the plus fraction characterization is described in Figure 3.34. First the C_{7+} components are splitted into a series of components as shown in Table 3.3, where the first 6 components are kept as pure components. The plus fraction however is splitted into further range of components. Splitting is decided on the basis of the method chosen for splitting. Methods used in this analysis are Whitson,

Petroleum Experts 1 and Petroleum Experts 2 (Whitson & Brulé, 2000). Petroleum Experts 2 is developed specifically to split the plus fraction in gas condensate system and hence is a preferred method in this study. However, an attempt is made by other 2 methods as well before arriving on the final split.

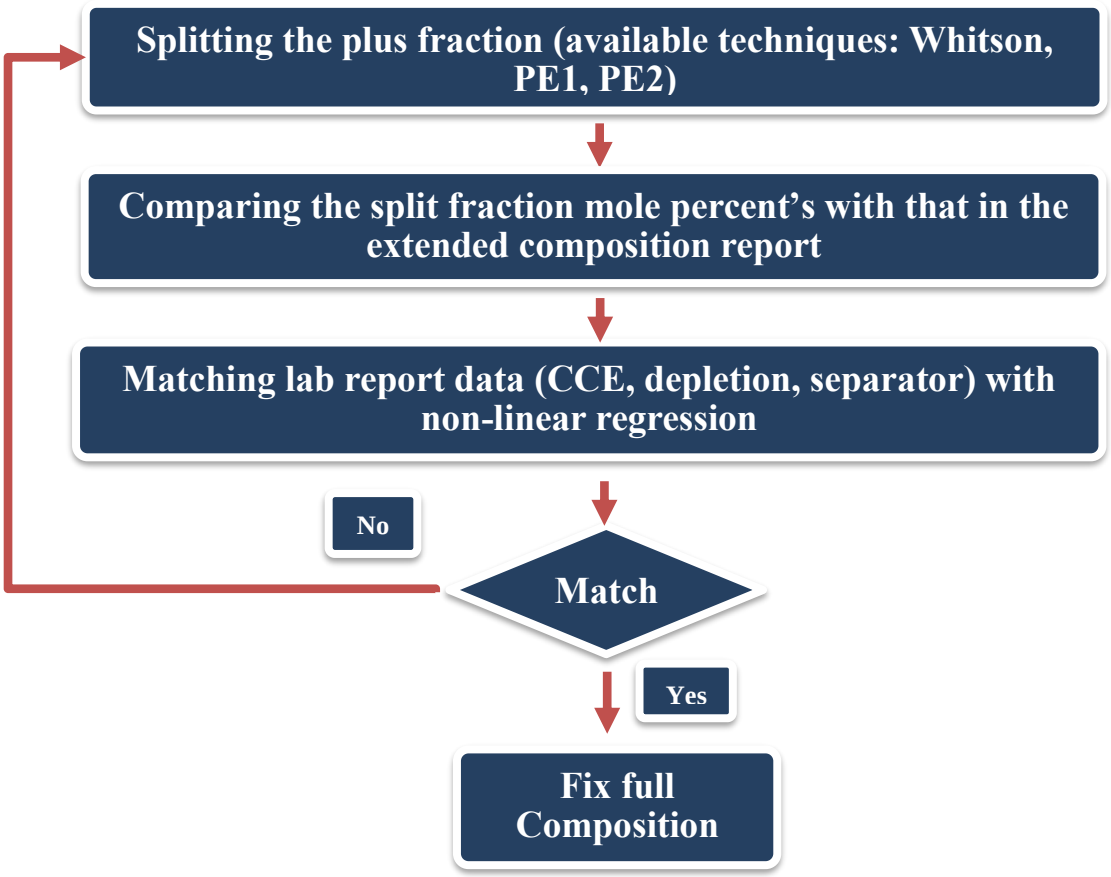

Figure 3.34. Workflow for C+7 characterization used in this thesis. First the C7+ fraction is splitted into multiple components and experimental data is matched with the components. A composition which gives best match with the experimental data with minimum number of components is selected

Table 3.3. Final components after splitting by PE2® splitting scheme. All components till C6 are used as pure components and after C6 all components are treated as pseudo components. This characterized scheme is used for nonlinear multiple regression to match all the fluid properties.

Component	Type
CO2	Pure Non Hydrocarbon
C1	Pure Non Hydrocarbon
C2	Pure Hydrocarbon
C3	Pure Hydrocarbon
iC4	Pure Hydrocarbon
nC4	Pure Hydrocarbon
iC5	Pure Hydrocarbon
nC5	Pure Hydrocarbon
C6	Pure Hydrocarbon
C7::C7	Pseudo
C8::C8	Pseudo
C9::C9	Pseudo
C10::C10	Pseudo
C11::C11	Pseudo
C12::C13	Pseudo
C14::C15	Pseudo
C16::C17	Pseudo
C18::C20	Pseudo
C21::C33	Pseudo

Number of components in the split is decided on the basis of the match obtained by non-linear regression on the PVT experiments with the input parameters. Table 3.4 summarizes the major properties matched in the experiment and Table 3.5 summarizes the inputs used for multiple nonlinear regression. A trial and error procedure is followed with the methods and number of components until a simultaneous match is obtained on all the properties with minimum number of split components.

Table 3.4. Properties matched during the non-linear multiple regression. A total of 10 properties are matched simultaneously. CCE stands for constant composition experiment and CVD stands for constant volume depletion study. GOR and FVF stands for gas oil ratio and formation volume factor respectively.

Properties
Saturation pressure
Density at saturation pressure
CCE gas density
CCE liquid dropout
CCE relative volume
CCE z factor (vapor phase)
CVD liquid dropout
CVD Z factor
Separator oil FVF
Separator GOR

Table 3.5. Parameters used to match the properties of various experiments described in table xx. A combination of these 4 properties for 16 components, hence a total of 16*4=64 properties is used to match the composition.

Properties
Critical pressure
Critical temperature
Accentric factor
Volume shift (temperature independent)

The final characterized sample includes 16 components i.e 6 pure components and C_{7+} further splitted into 10 components. Some of the critical properties matches after the fluid characterization are summarized from Figure 3.35 to Figure 3.42. Figure 3.35 to Figure 3.38 show the results of matching, key actual and predicted data from the depletion experiment. Figure 3.39 to Figure 3.41 show the key results from constant composition experiment (CCE). CCE results are necessary to verify the dew point pressures and all the experimental values above dew point pressure as opposed to depletion experiments which are more useful for predicting phase behavior below dew point pressure.

Figure 3.42 shows the phase envelope generated from the characterized sample. Depletion experiments show a typical retrograde gas condensation with condensate appearing at dew point pressure of 4284 Psi and then gradual evaporation of the generated condensate. Component wise production stream shows that the production is dominated initially by the lighter components which is expected from a gas condensate reservoir.

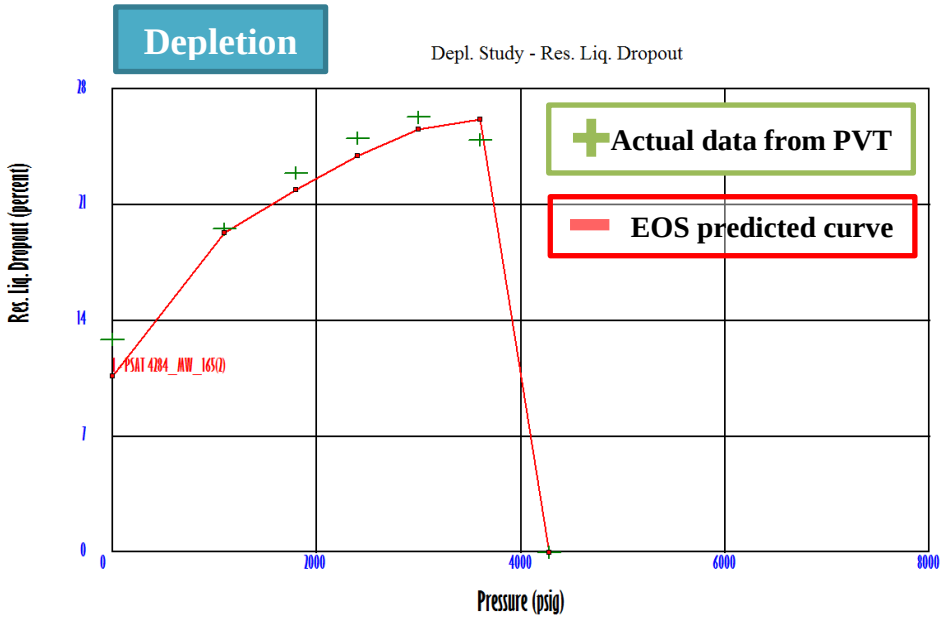

Figure 3.35. Liquid dropout curves (actual and simulated) from characterized composition. Green crosses show the actual dropouts observed during depletion and the red curve show the equation of state (EOS) predicted. The data exhibits a classic retrograde condensation. As pressure depletes i.e. from right to left on X axis, condensate starts appearing at dew point pressure (4284 psi) and below the dew point condensate starts re evaporating.

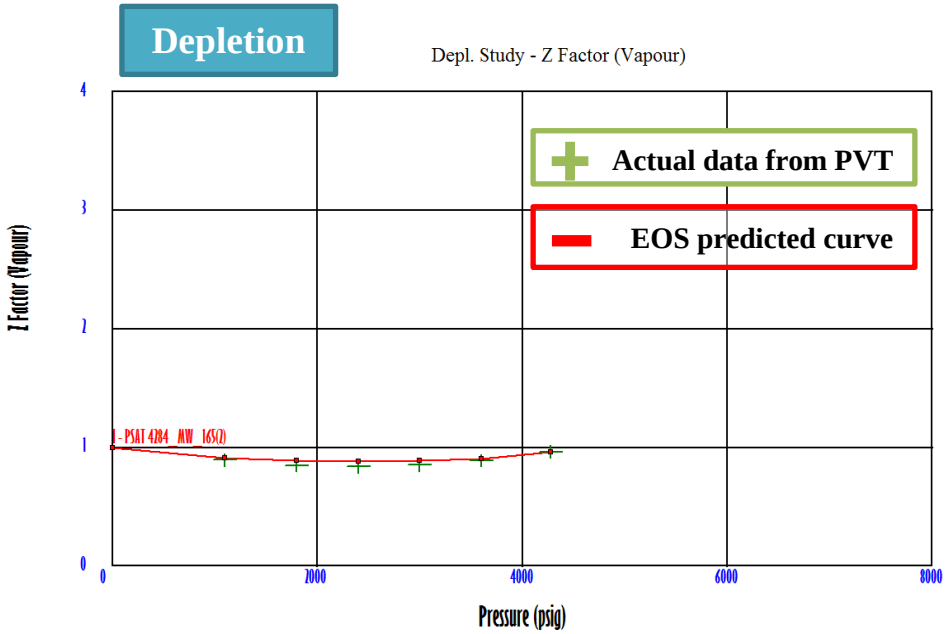

Figure 3.36. Vapor phase Z factor (actual and simulated) from characterized composition. Green crosses indicate the actual experimental data and red curve indicates the equation of state predicted Z factor. As pressure drops (right to left on X axis) Z factor first decreases and then increases.

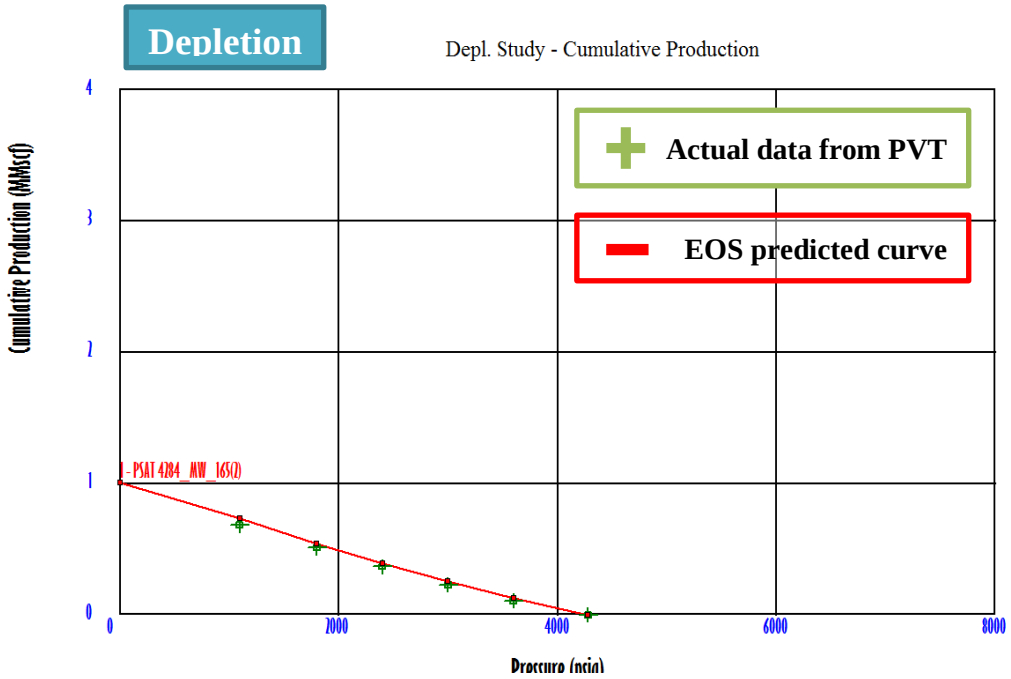

Figure 3.37. Cumulative production (actual and simulated) from characterized composition. Green crosses are the experimental data and the red curve is equation of state(EOS) predicted gas volumes. It can be observed that the EOS matches the experimental data very well.

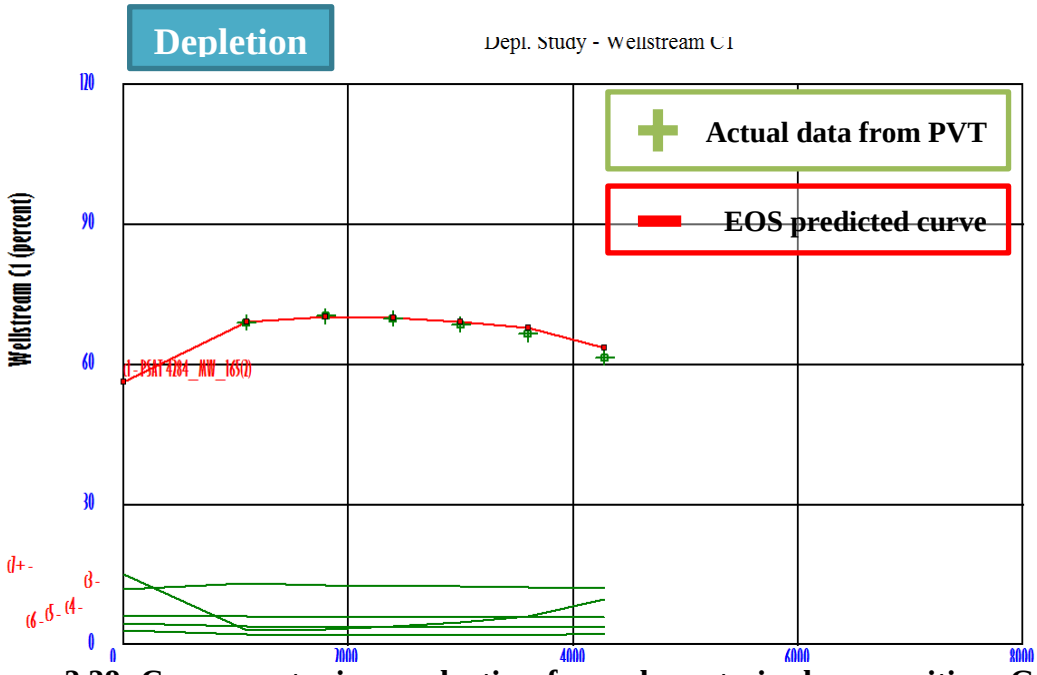

Figure 3.38. Component wise production from characterized composition. Green crosses are the experimental dataset and red curve is the EOS predicted curve. This curve shows the percentage of methane (C1) produced during the depletion process. However, all 16 components are predicted and matched with experimental dataset.

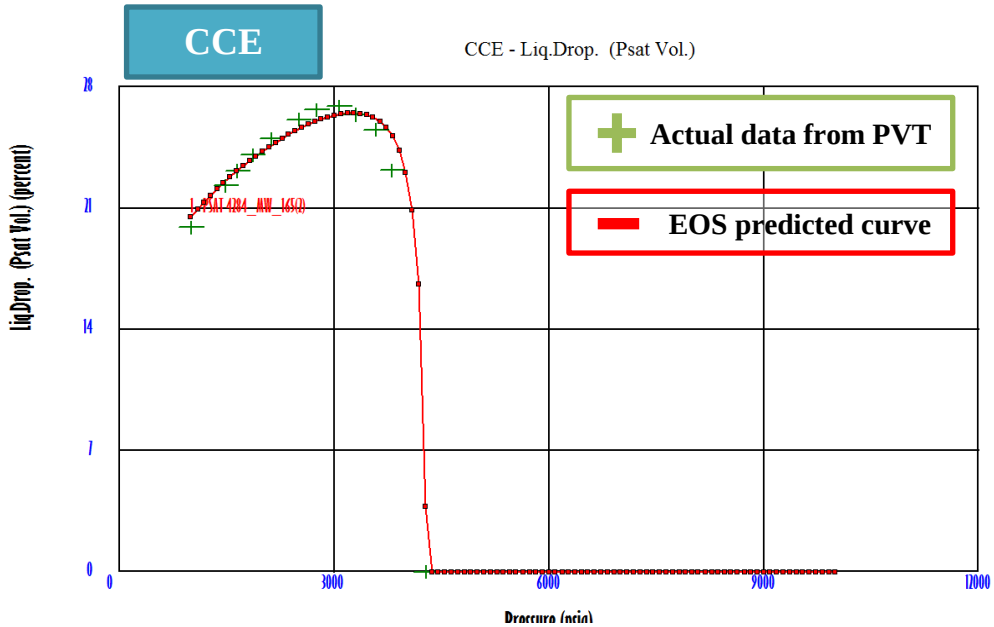

Figure 3.39. Liquid dropout curves (actual and simulated) from characterized composition from constant composition experiment (CCE). Green crosses indicate the experimental data points and red curve indicates the EOS generated curve. A good match is obtained for the full pressure depletion from dew point (4284 psi) to about 800 psi which is also the abandonment pressure.

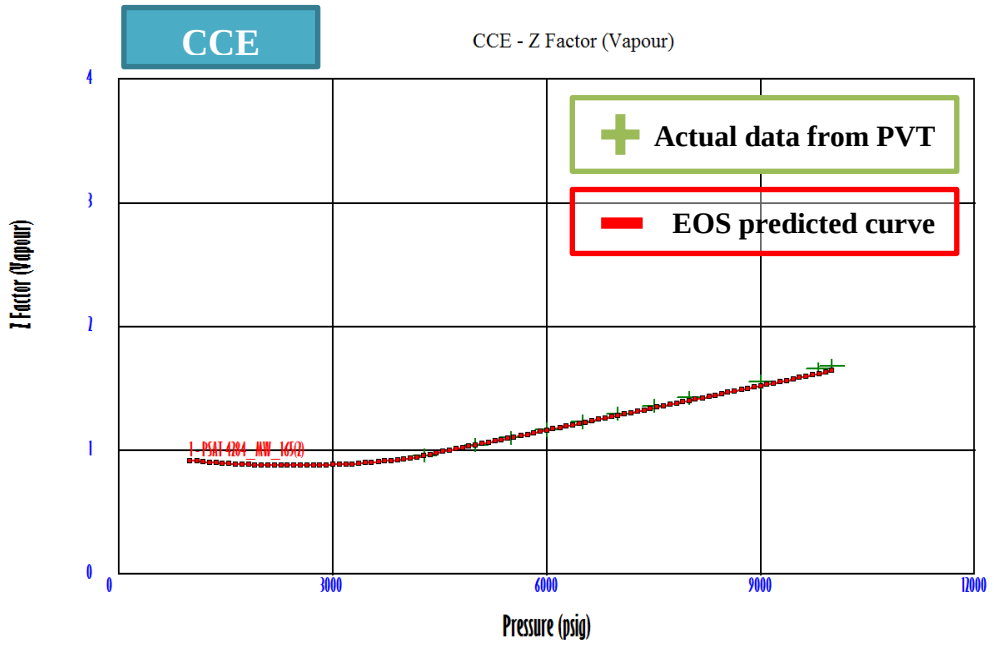

Figure 3.40. Vapor phase Z factor (actual and simulated) from characterized composition. Vapor Z factors obtained from the CCE experiment. Green crosses are the actual experimental data and the red curve is EOS predicted curve. IT can be observed that during depletion at constant composition, Z factor first decreases (right to left) and then increases.

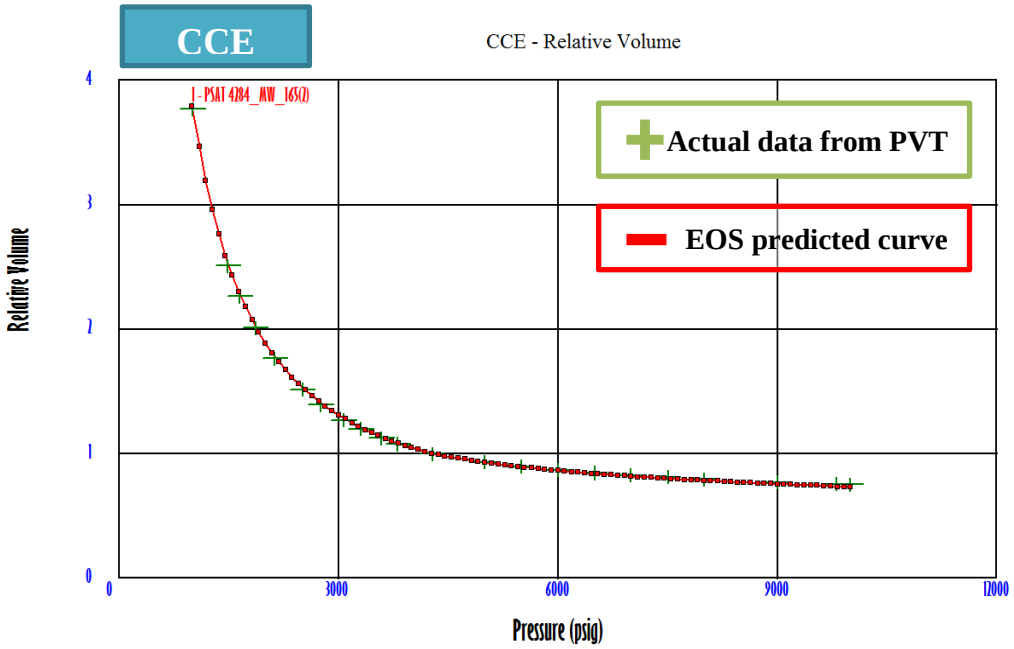

Figure 3.41. Relative volume (actual and simulated) from characterized composition. Relative volumes are the volumes with respect to the volumes at dew point pressure (volumes normalized by cell volume at dew point). Green crosses are the experimental dataset and red curve is the EOS predicted dataset.

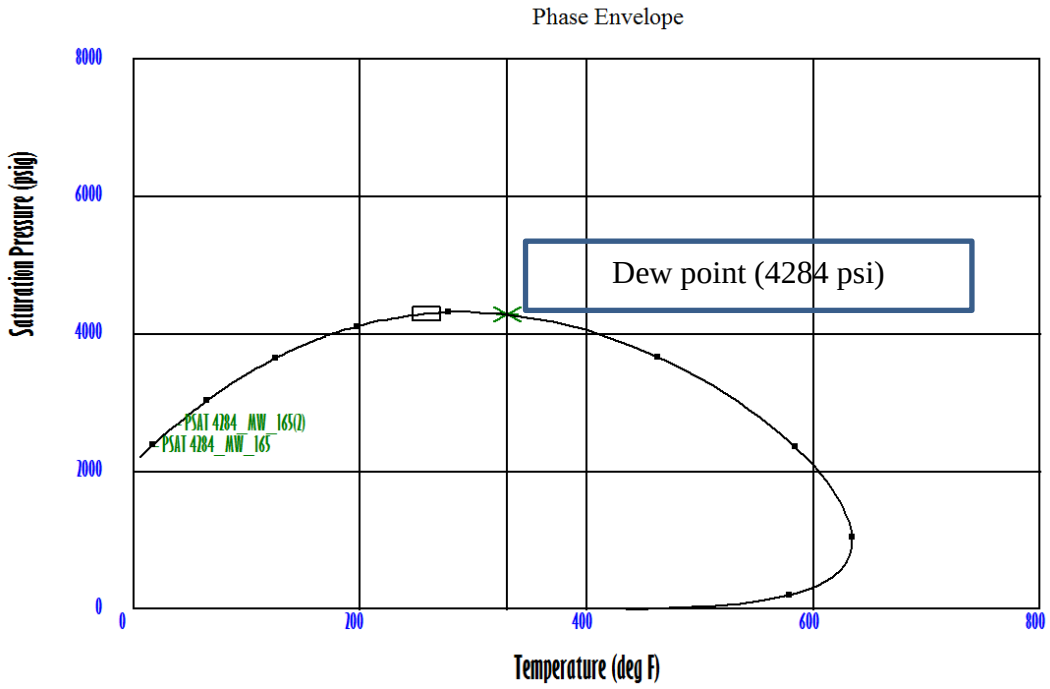

Figure 3.42. Phase envelope generated from characterized sample. Phase envelope is preserved during the characterization and the dew point is regenerated at 4284psi.

3.5.4. Lumping of Characterized Fluid

A total of 16 component characterized sample is too large to simulate with the computers used for simulation. Also, more components introduce more variables in the constitutive equations during the flow simulations. With more components it is difficult to honor the material balance during simulation and hence 16 components listed in table 3.3 have to be lumped into smaller number of components. A detailed account of the lumping procedure is documented by (Alavian, Whitson, & Martinsen, 2014; Rastegar, Jessen, & California, 2009).

Even with some guidelines, lumping procedure is hit and trial especially with higher carbon numbers. Moreover, as explained above, after lumping the components should preserve the characteristics of the characterized sample. This means lumping should be done in a way to honor all fluid properties previously matched in the section 3.5.3.

Following the guidelines described by (Alavian et al., 2014; Rastegar et al., 2009) and hit and trial for the higher carbon numbers, a final lumping scheme is decided. This lumping scheme is summarized in the Table 3.6. For the first three lumps, components with similar properties such as molecular weight, shape of the molecules (captured in acentric factors) are lumped together into 1 pseudo. For heavier components, lumps are created by hit and trial matching the depletion, CCE and separator experiments in order. The dew point and phase envelope is then matched by adjusting the binary interaction coefficients.

Table 3. 6. Final lumped composition which is used to match the fluid properties.

N2 + C1
CO2 + C2 + C3
iC4 + nC4 + iC5 + nC5 + C6
C7::C7 + C8::C8 + C9::C9
C10::C10 + C11::C11
C12::C13 + C14::C15
C16::C17 + C18::C20 + LAST_PSEUDO

Figure 3.43 to Figure 3.45 show the CCE experiments previously matched by 16 components and now with 6 components. Figure 3.46 and Figure 3.47 show an example of vapor Z factor and liquid dropout curves respectively for depletion experiment. All matches are preserved in the lumping scheme.

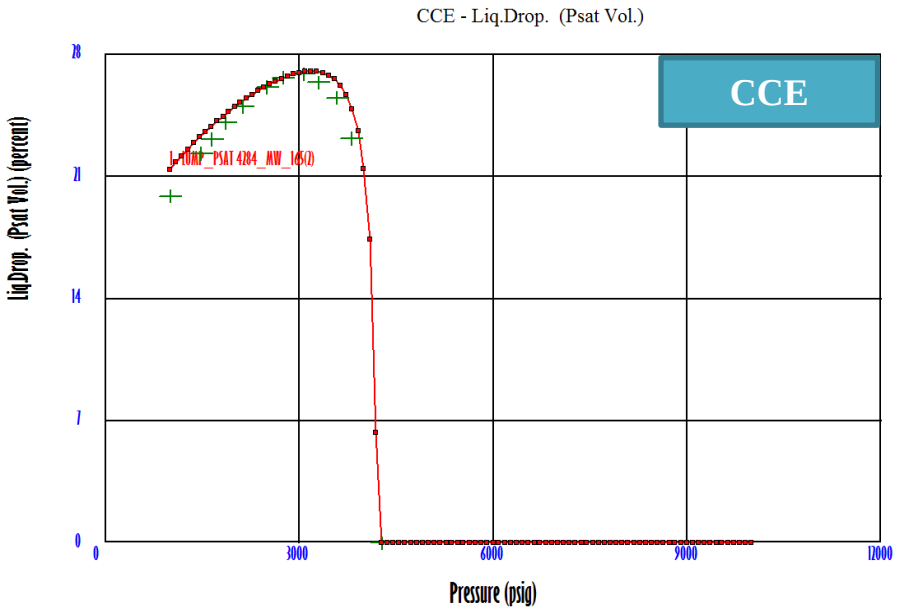

Figure 3.43. Liquid dropout curves (actual and simulated) from lumped composition. Match is preserved in the lumping process.

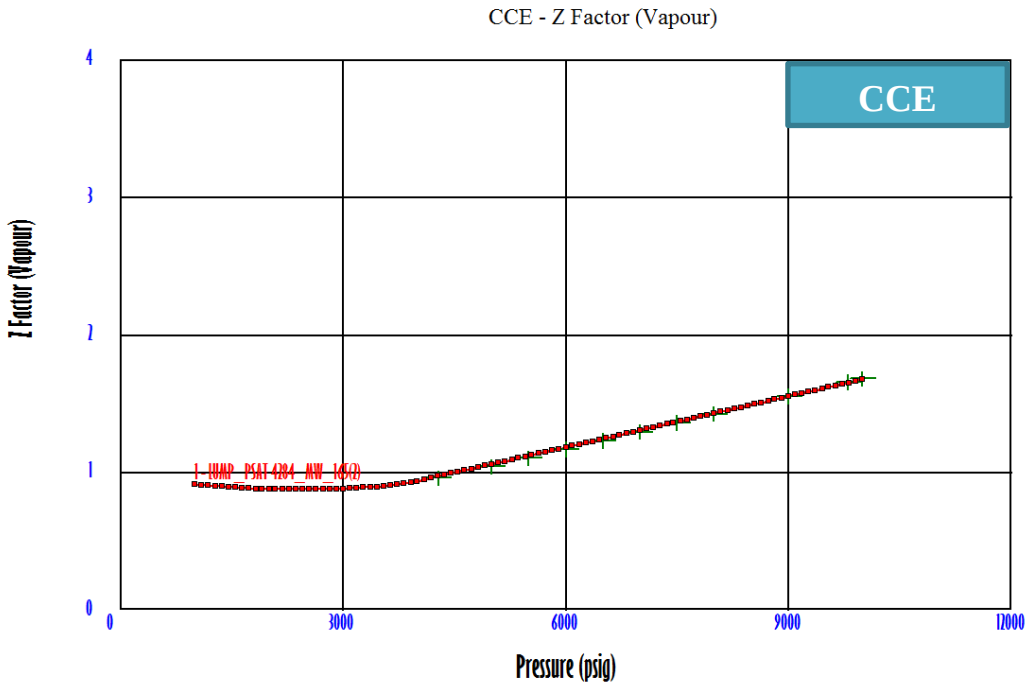

Figure 3.44. Vapor phase Z factor (actual and simulated) from lumped composition. Match is preserved in the lumping process.

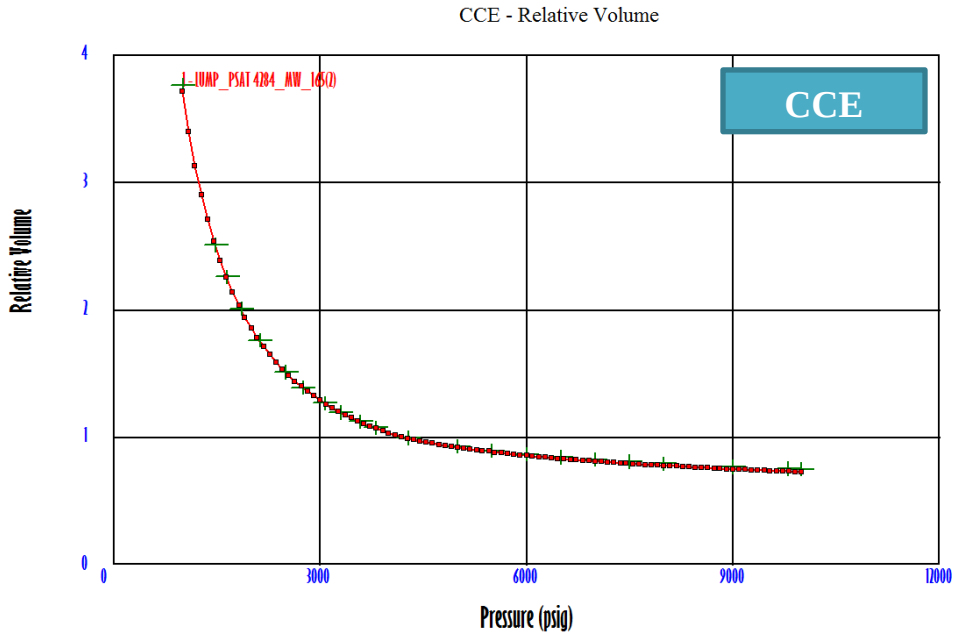

Figure 3.45. Relative volume (actual and simulated) from lumped composition. Match is preserved in the lumping process.

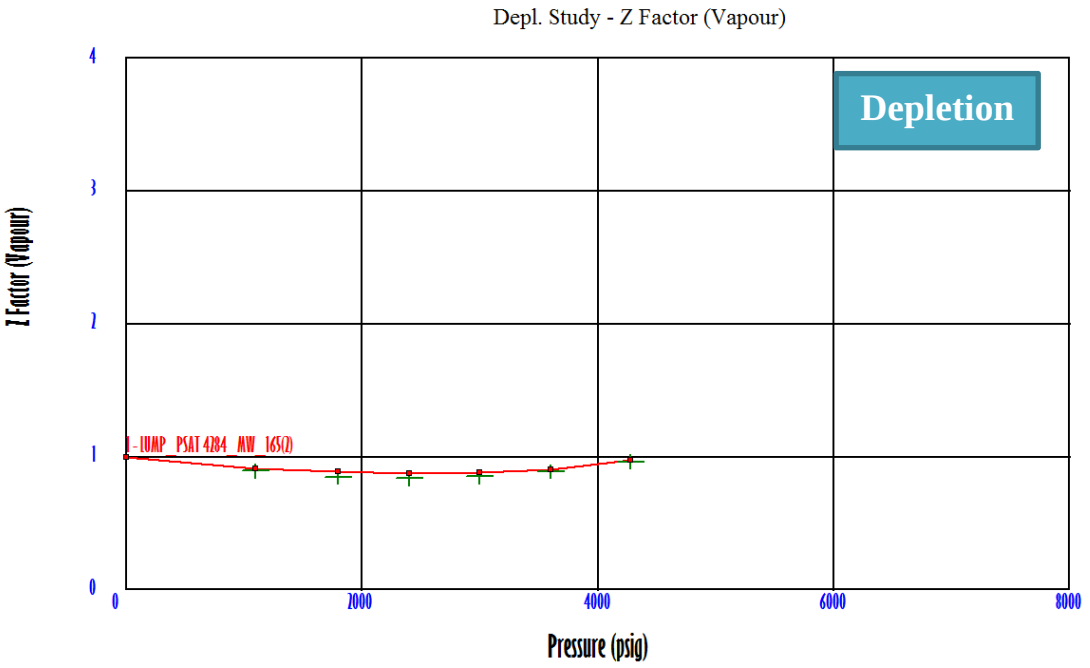

Figure 3.46. Vapor phase Z factor (actual and simulated) from lumped composition. Match is preserved in the lumping process.

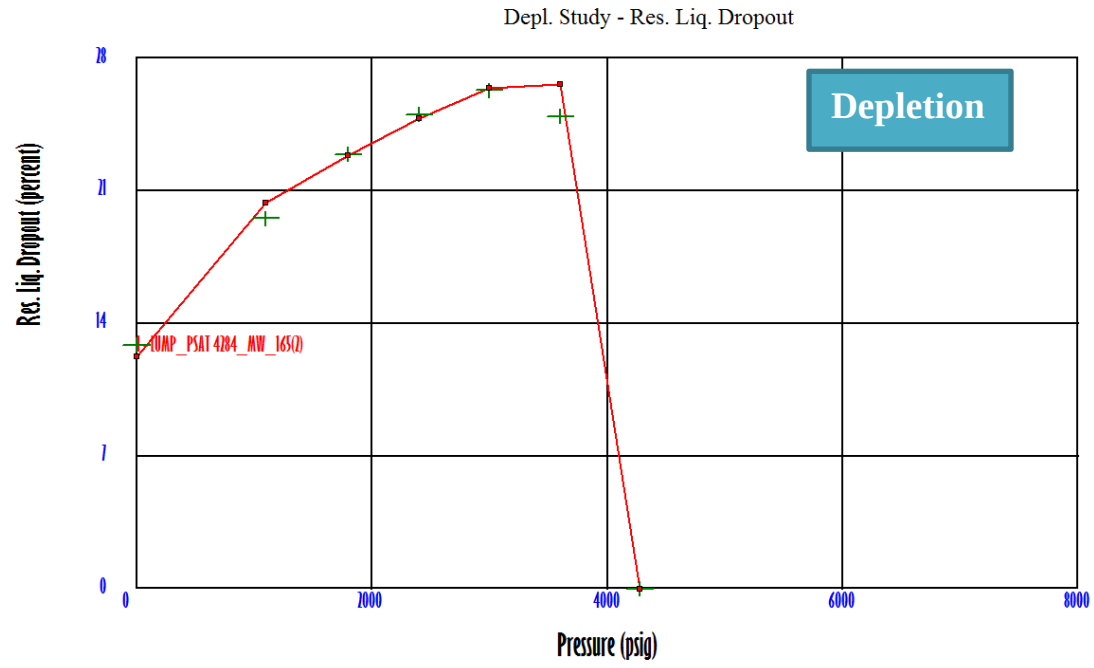

Figure 3.47. Liquid dropout curves (actual and simulated) from lumped composition. Match is preserved in the lumping process.

3.6.Simulation Study

3.6.1. Model Upscaling

Model created during the static modeling to honor all the rock type distribution consists of 10 million cells. However, the current computational ability in the simulation software CMG® with available licenses does not support this grid. Hence, this model has to be upscaled until it can be used for simulation.

This is done by reiterating the initial model by reducing the number of layers in each zone. Grid cell size is not changed to honor the completions data. After multiple iterations the final model is composed of 10 layers. 4 layers each in upper and lower EFS and 2 in middle EFS. This scheme is adpted as the upper and lower EFS are thicker than the middle EFS.

3.6.2. Model Setup

For simulation study, software platform (CMG®) is used. It is preferred because in the past from personal experience, it had been found very useful in modeling fractures from the front end. The corner point grid with all properties modeled during reservoir characterization is imported in the simulator. The fluid model created in PVTP® is also imported in the simulator. Relative permeability is used as one of the history matching parameters in this study. Relative permeability curves are defined by the correlations is shown in the Figure 3.48 and Figure 3.49. The relative permeability curves are generated by general correlation available in CMG® by adjusting mainly the connate and critical water saturations.

A single porosity model is assumed in this study. As no FMI log or any other direct evidence is available for the presence of prominent natural fractures, single porosity model is the best choice due to its simplicity. The hydraulic fracture network is then created in the matrix.

Model is initialized with a water and gas system with no transition zone under an assumption of gravity-capillary equilibrium (Coats, Dempsey, & Henderson, 1971). The initial reservoir pressure is defined at the top of the reservoir as 11500 Psi. As no information on capillary pressure curves is available an assumption of no transition zone is made. The initial reservoir pressure is calculated from the post –fracture reports made available by the operator. Composition of the fluid is initialized from the lumped fluid composition described in the fluid modeling section. Exact composition of the lumps is not mentioned due to data confidentiality.

Numerical controls for the linear solver are initially set to default and later tuned during the history matching procedure. The final tuned parameters for the finite difference grid are listed in Table 3.7. A maximum timestep size is fixed at 30 days to honor the daily production data and to get a monthly forecast after the history matching portion of the production data. Maximum number of iterations is obtained by hit and trial to increase the number of iterations to converge all constitutive equations for all phases.

Wells are coupled explicitly in the model where the bottomhole pressures calculated in the form correlation Hagedorn and brown is used. A comparison of different well correlation to calculate the well bottomhole pressure from tubing pressure is given in appendix B. Three wells on a PAD are used for the simulation purpose and then further sensitivities are done once a satisfactory history match is obtained.

Table 3.7. Numerical parameters used for history matching of basecase 500' spacing wells. Maximum timestep size is kept at 30 days to honor both the daily production data. It also allows the model to generate monthly forecast after the daily production is history matched. This leads to lesser run times without compromising the required details in the dataset.

Numerical parameter	Value
Maximum number of timesteps (MAXSTEPS)	100000
Maximum number of timestep size (DTMAX)	30 day
Minimum number of timestep size (DTMIN)	1E-7 day
First time step size after well change (DTWELL)	0.01 day

3.6.3. Stimulated Reservoir Volume (SRV) Generation

With grid and fluid model in place, microseismic data is imported in the grid. Methodology suggested by (Suliman et al., 2013) is used to create a SRV in the model. First, an amplitude filter is applied on the microseismic data to filter out the hydraulic fracturing events only (Suliman et al., 2013). All the microseismic events are mainly divided into following categories:

(a) Fault reactivation related

(b) Hydraulic fracturing related

(c) Ductile rock failure related

Based on work of Kanamori (1975) and Suliman et al. (2013), seismic moment and magnitude is calculated. Later the seismic magnitude was plotted with time and three different types of events described earlier are identified. Suliman et al.(2013), have also identified the failure criterion of EFS. The criterion is tabulated in Table 3.8. They have

also noted the amplitude range of the events which fall under hydraulic fracturing related events. These are tabulated in Table 3.9.

Using the amplitude filters, only the events related to hydraulic fracturing are filtered out. Microseismic data with only hydraulic fractures is given in Figure 3.48. Using the hydraulic fracture events fracture networks are created in the gridblocks containing the events. A probability is not assigned to magnitude and the number of events to create the fracture network as it is observed that the gridblocks away from the wellbore are discontinuous in nature. In other words, the fracture density diminishes away from the wellbore. This way the disconnected events are depleted slowly during production and a probability on amplitude and events is not required.

Table 3.8. Seismic failure criterion for EFS (after Suliman et al., 2013)

Failure criterion	Value	Unit
Magnitude of completeness	-3.25	
Seismic moment	167880.4	N-m
Seismic energy	8.39	Joule

Table 3.9. Microseismic amplitude range for different events in EFS (Suliman et al., 2013)

Event	Amplitude range
Hydraulic fracturing related	<-2.3 & > -3.25
Fault reactivation	>-2.3
Ductile deformation	<-3.25

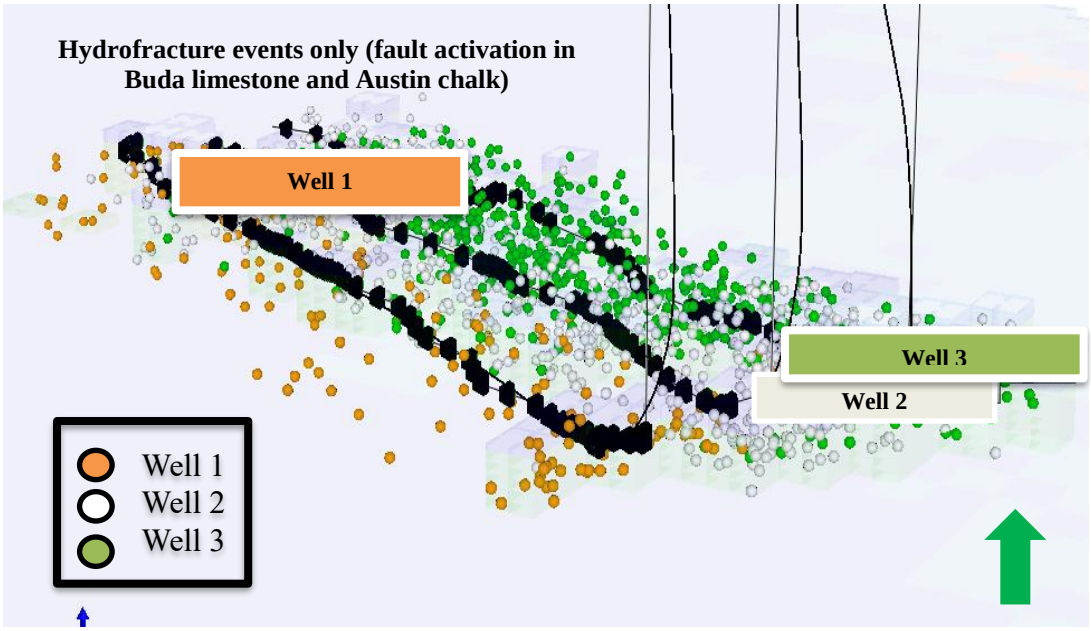

Figure 3.48. Well wise microseismic events (hydraulic fracturing related only)

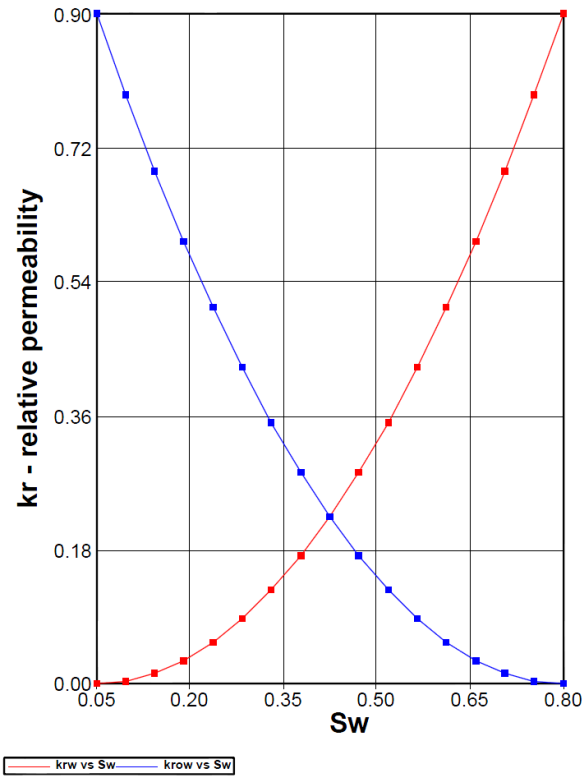

Figure 3.49. Gas relative permeability curves. Figure shows gas relative permeability with water saturation.

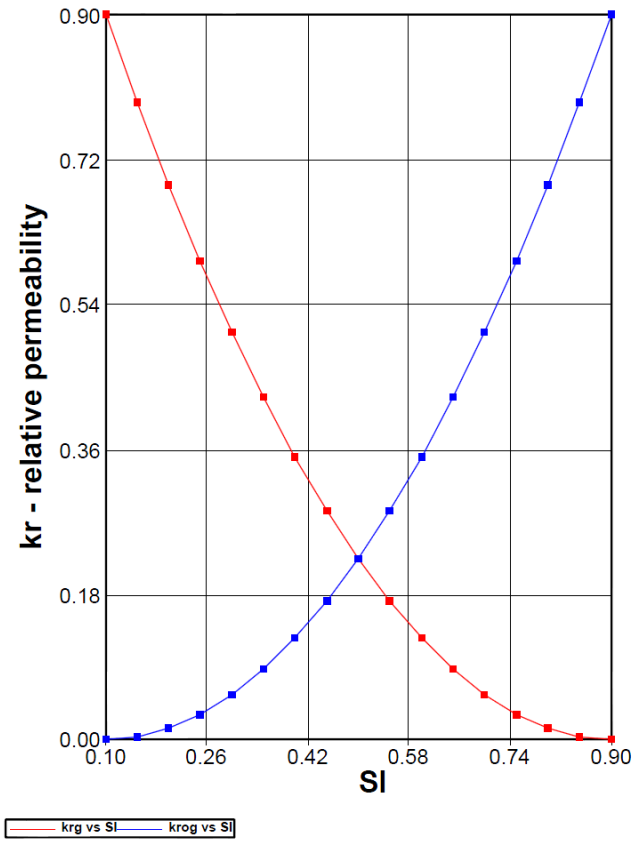

Figure 3.50. Gas permeability curves. Figure shows gas relative permeability with liquid saturation

3.6.4. History Matching of Base Case Model

The wells are operated on a gas rate control. With model under the gas rate control, the bottomhole pressure, condensate rate and water rate are predicted. First an initial match on condensate rate and bottom hole pressures are matched. Once, these are matched to match the water rates the water saturation inside the gridblocks is increased until a satisfactory match on water rate is obtained. The constraints are set on the water saturation by adding the frac water to the gridblocks in addition to the well log calculated water saturation. The results from the history match are summarized from Figure 3.51 to Figure 3.57. Figure 3.51 and Figure 3.52 show the results of the original gas rate and the simulated gas rate curves. As the model is run under gas rate control i.e. model tries to

honor the produced gas and predicts all other parameters it is vital that the gas rate should match perfectly. It evident from the figures that the gas rates and the gas cumulative volumes match perfectly.

Figure 3.53 and Figure 3.54 summarize the oil rates and the cumulative oil volumes. The model runs on the gas rate control and from the PVT model the oil rate is predicted. This is also the reason why a robust PVT model is needed during the simulation process. On the oil rate curve (Figure 3.53), it is important to note that the oil rates match over a significant period of time but the cumulative volumes do not show a perfect match. Degree of deviation depends from well to well basis. This can be explained due the CGR trends which is summarized in Figure 3.57. The CGR starts from a higher value and then stabilize at a value ~200-220 BBL/MMSCF. This can be due to unstable flow regimes, compositional gradient within the reservoir along with the partial closure of fractures due to uneven proppant distribution. This can also be attributed to a combination of all these factors.

As of now, there is not enough dataset to resolve and model the compositional gradient and variability with time to model these effects. Hence, a constant CGR value is modelled in the compositional model. This implies the model produces with a constant CGR of 200 bbl/MMscf before reaching the dew point pressure. In actual dataset the CGR starts with a higher value. Hence, the model underestimates the condensate production in initial production stem. A good match on oil rates is obtained after the CGR's are stabilized but the initial deviation leads to difference in the cumulative volumes. The degree of variations from well to well depends on the actual CGR of individual wells as the CGR varies from time to time and well to well.

The individual CGR of each well also vary by a small fraction (5%-10%) due to many factors such as compositional gradient across reservoir, exact landing position of the lateral in the EFS section (upper EFS has a higher CGR than lower EFS), production allocation etc. and hence the degree of variability in cumulative volumes differ in each well. This problem can be alleviated to an extent by assigning different PVT sets to different wells. However, the whole purpose of this study is to model interference i.e. all wells are sharing production and the system is same hence no compositional gradient assigned across the reservoir.

Water rates are matched by increasing the grid-block saturations and the result is summarized in Figure 3.56. Additional water from hydraulic fracturing fluid is added to the initial well log water saturation to obtain a match on water rates. A good match is obtained on the water rates by this technique except for well 3 during the late production trend. This well is re –fractured by the operator and hence the rates and pressures on this well do not match after the re-fracturing.

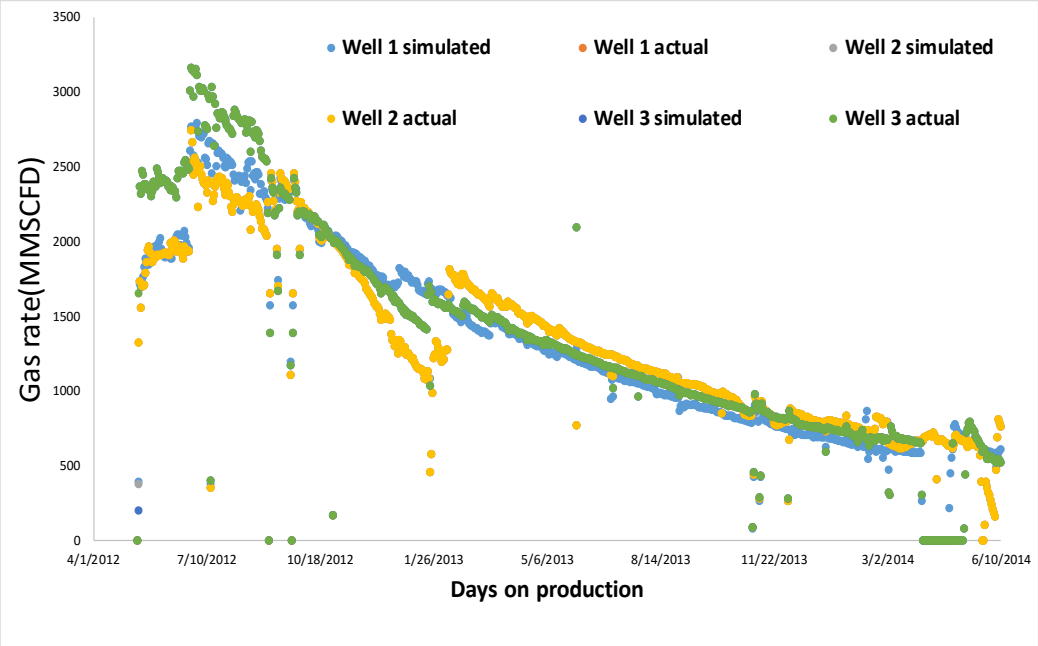

Figure 3.51. Gas rate with time for all three wells on PAD (actual and simulated). It is an exact match as the model is running on gas rate control.

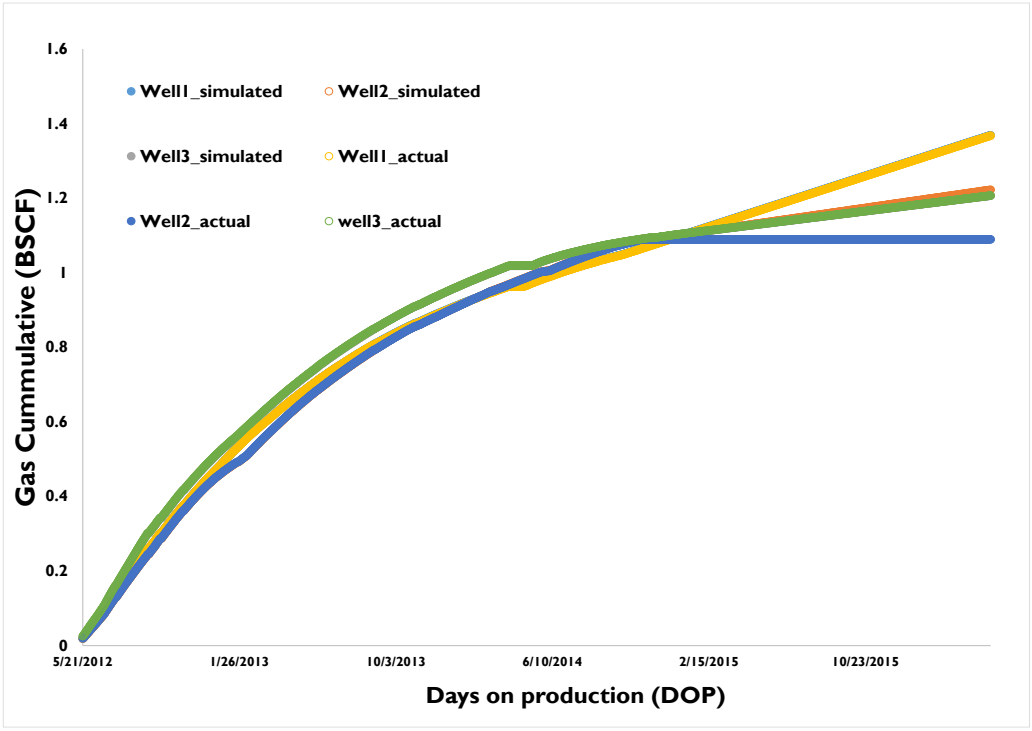

Figure 3.52. Cumulative gas volumes for all three wells on PAD (actual and simulated). It is an exact match as the model is run on gas rate control.

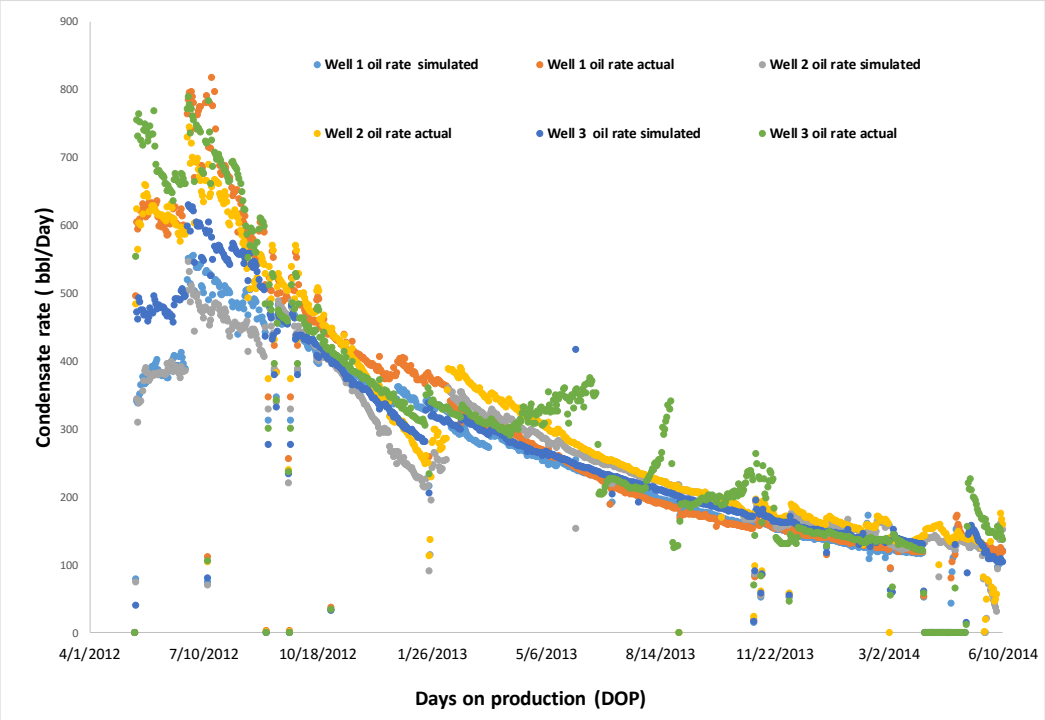

Figure 3.53. Predicted oil rates for all three wells on the PAD (actual and simulated). Model underestimates the oil production in the beginning as the well start with a higher CGR. However, after the CGR stabilizes model predicts the oil rates accurately.

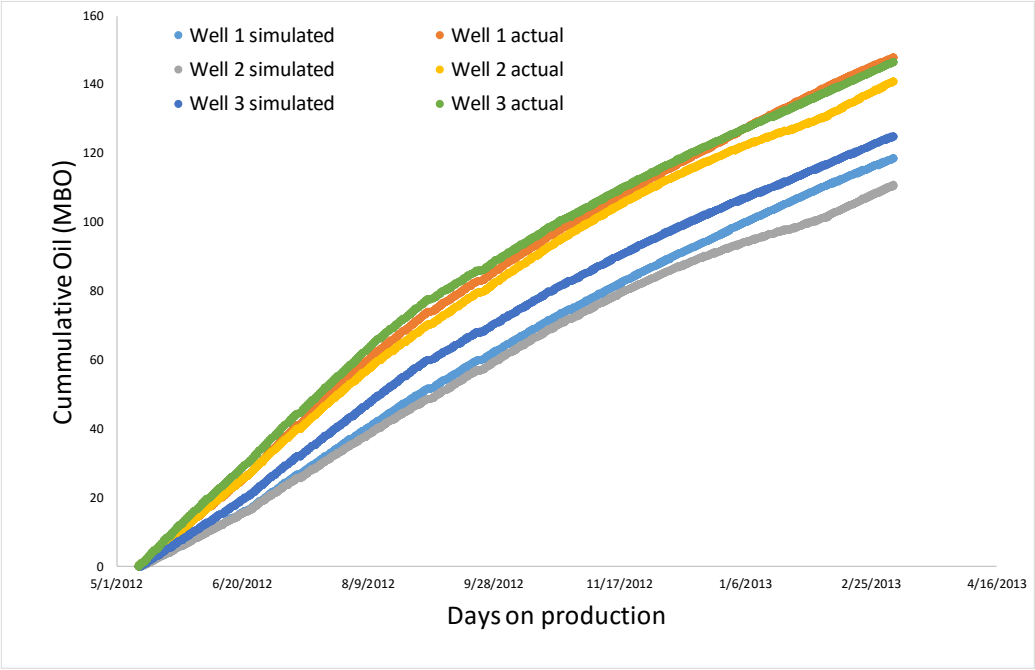

Figure 3.54. Predicted oil cumulative volumes for all three wells on the PAD (actual and simulated). Due to variability in CGR there is difference in predicted vs. actual CGR in the beginning.

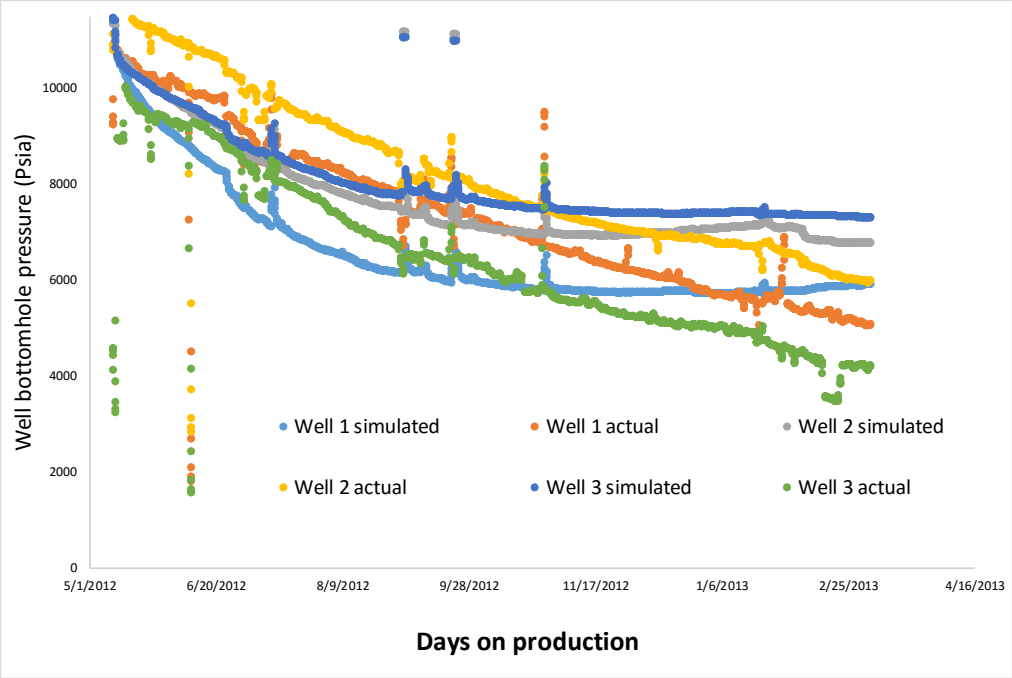

Figure 3.55. Predicted flowing bottomhole pressures (FBHP's) for all three wells on the PAD (actual and simulated). It can be observed in the figure that a good match is obtained on the flowing pressures and the pressure trend is honored in the analysis.

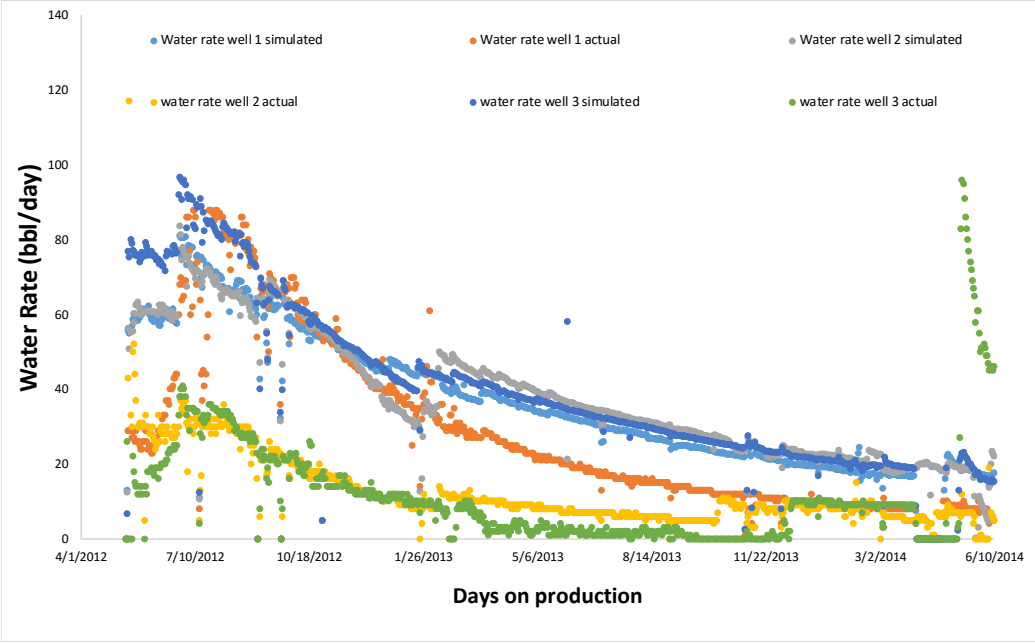

Figure 3.56. Predicted water rates for all three wells. A good match is obtained on the water rates by adding the fracturing water in the grid blocks assuming water propagates throughout the well spacing i.e. fluid travels from one well to another (500'). Later portion of the well 3 shown by a green spike in the image corresponds to a re-frac and hence show a different trend.

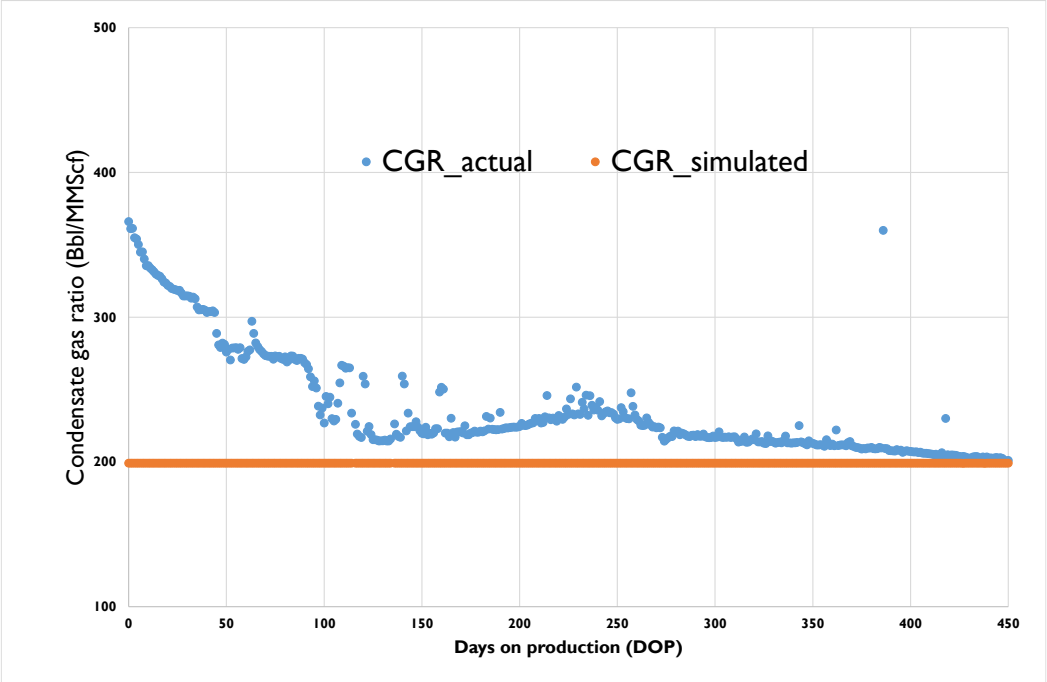

Figure 3.57. CGR trends over the well life. It can be seen that the wells start with a higher CGR and then stabilize to a constant lower CGR. The stable CGR is modelled during the PVT modeling and hence, the initial stem of the oil rates cannot be matched. On the Y axis is the CGR (bbl/MMscf) and on the X axis is the days on production.

From this history matched model, the EUR's are obtained by running the same model on constant exit rates (rates at last day of history matched data) for a total well life of 30 years. The wells were put on production in 2012 and hence the model is run until 2042.

A secondary constraint of 800 Psi of minimum bottomhole pressure is put on these wells. Hence, the model produces at exit rates and then produces until a minimum bottomhole pressure is reached or well life is complete. Cumulative oil and gas volume till end of well life is considered as expected ultimate recovery (EUR) from the wells. The results are summarized in Table 10.

Table 3. 10. Overall results summary. All EUR's based on 30 yrs. well life.

Well	1	2	3	Avg.
SRV (ft3)	4.80E+08	6.80E+08	6.25E+08	5.95E+08
Fracture conductivity	1000	1000	1000	1000
Fracture Width	0.01	0.01	0.01	0.01
Effective Permeability (mD)	1	1	1	1
Oil EUR (MSTB)	420	450	430	433
Gas EUR(BSCF)	4.9	5.4	5.2	5.2
OGIP, BSCF	39	39	39	39
Gas RF	13%	14%	13%	13%
Drainage Area (acres)	50	71	65	62

To calculate the original gas in place (OGIP), the volumetric equation 3.24 is used. Parameters used for volumetrics and its source are summarized in Table 3.11.

$$G = \frac{1}{22.957}\frac{Ah\phi S_{gi}}{B_{gi}} \tag{3.24}$$

Where, G is the original gas in place, A is Area (acres), h is the pay zone thickness (ft), S_{gi} is the initial water saturation, and Bgi is the initial gas formation factor.

Table 3.11. Parameters used for volumetrics.

Parameter	Value	Source
Area	57 ac	Calculated with 500 ft. well spacing and a fixed lateral length of 5000 ft.
Pay	220 ft.	Well logs
Porosity	10%	Median value from geostatistics
Initial water saturation	0.8	Median value from geostatistics
Initial Gas formation volume Bg	1.113	From PVT report
Final OGIP	39 Bscf	Calculated

Once, the EUR and the OGIP is known the gas phase recovery factor (RF) is calculated by dividing the gas EUR by OGIP. To calculate the drainage area, the micro seismic volumes are used. The micro seismic volumes are divided by the pay (h) to back calculate the drainage area under the assumption that everything inside microseimic generated SRV is drained by the respective wells.

A fixed fracture conductivity of 1000 mD and a fracture width of 0.01 ft. for all fractures is used for history matching purpose. The average gas recovery factors for all the wells is observed to be 13% and average drainage area is 62 acres.

Following conclusions can be drawn from the results:

(a) The middle well shows a higher SRV than the other two wells.

This can be explained by zipper frac effect (Sierra & Mayerhofer, 2014). It is argued by (Sierra & Mayerhofer, 2014) that the zipper fracturing alters the pre –existing stress regimes making them more even and hence fracture networks are evenly distributed across the reservoir. It can be also observed in the fracture networks created using microseimic data in Figure 3.58. There is more stimulation in the middle portion of the reservoir and less on the extreme right or left. Also, there is more well stimulation on heel side of the well and less on the toe side.

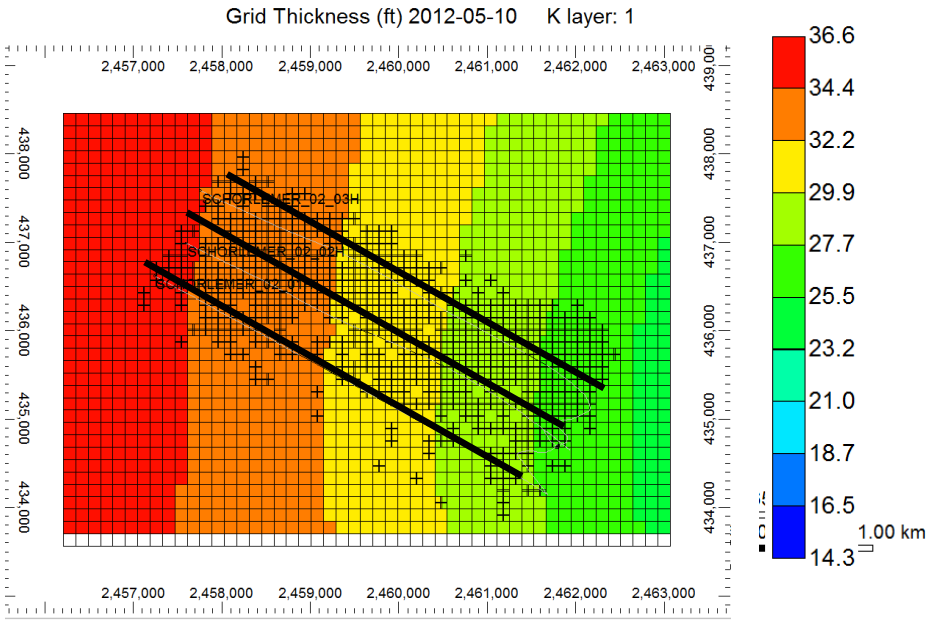

Figure 3.58. Fracture network assigned to wells. Fracture networks are represented in black crosses. Wells are represented by black sticks. From left to right; well 1, well 2 and well 3. More stimulated rock volume (SRV) is available in the middle portion of the reservoir. On extreme left or extreme right, there is less stimulation. Hence, more SRV is available for well 2 to drain. Also, on south east portion of the reservoir is the heel of the well and north west is the toe of the well. There is more stimulation towards heel of the wells vs. toe of the wells.

(b) Volumetric reservoir

Figure 3.59 shows the pressure depletion in the reservoir at the end of the well life. It can be observed that there is little or no contribution outside the fracture network. This implies that the reservoir essentially acts as a volumetric reservoir. Hence, same operating conditions can lead to different effect on the recovery in different wells. Well 1 which has a much lower SRV than well 2 and 3 but operated at same rates, GOR rises much earlier than in well 2 or well 3 (see Figure 3.60).

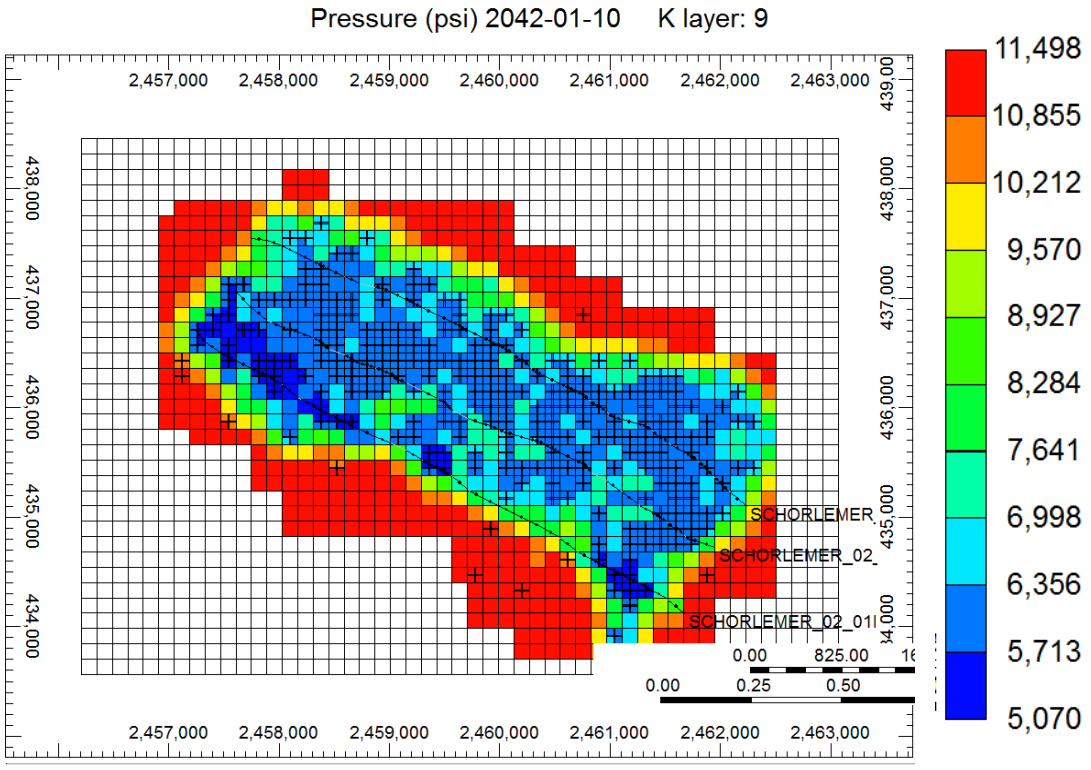

Figure 3.59. Pressure depletion in the reservoir at the end of well life. Uneven drainage areas can be observed all across the reservoir. The wells are represented by sticks and the fracture network is represented by the crosses. It can be seen that the region where there are no fracture networks, there is no pressure depletion.

Figure 3.60 shows the gas oil ratio (GOR) trends of all wells. The early increase in GOR implies an early drop in reservoir pressure and hence early condensate banking effect. Early condensate banking means the condensate recovery in the well will suffer and hence it should be taken into account in the reserves accounting process. This observation is further examined in section 3.6.7, where the effect of drawdown's is explored and calibrated with respect to condensate banking.

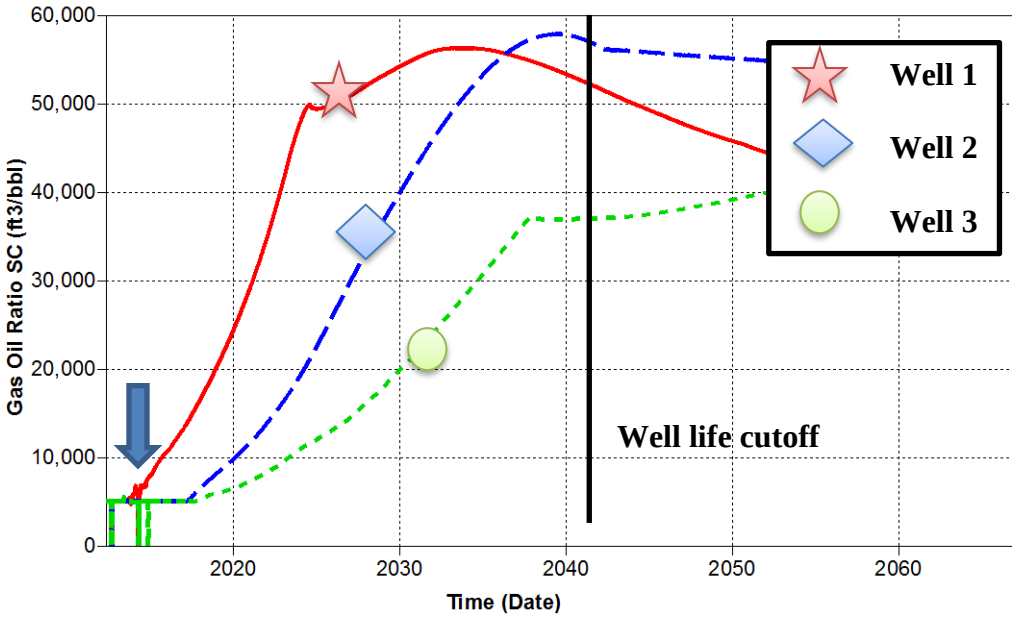

Figure 3.60. GOR trends for all wells on the PAD. It can be observed that GOR increases much earlier in well 1 than well 2 or 3 which is shown by the blue arrow. Hence, the dew point is reached earlier in the well with less SRV. This means the same chokes cannot be used for all wells on same PAD. Rates have to be optimized according to the stimulated reservoir volume(SRV).

3.6.5. Well Spacing Sensitivities

Well spacing sensitivities in this study is carried out for two well configurations i.e. when wells are placed in the same layer and when wells are placed in a staggered fashion. These two scenarios are elaborated in Figure 3.61 and Figure 3.62 respectively. The former shows an example where the wells are equally spaced in lower EFS section.

In Figure 3.62 however, the distance between the wells is still 200’ but the wells are placed in lower and upper EFS and hence the term staggered placement. This time well spacing between two lower EFS wells is 400’. This type of completion is designed under an assumption that I wells are downspaced under staggered placement, well interference effect can be reduced.

Generally, upper + middle EFS is lumped into upper EFS and hence in the sensitivity the section is described as upper EFS which is distinct from lower EFS which is more prolific in terms of petrohysical properties (high bulk density, high density porosity and low water saturation). Table 3.12 summarizes all the well spacing sensitivities carried out in this thesis. As the grid block spacing is kept at 70’ the spacing is kept in the multiples of 140’.

Table 3. 12. Well spacing sensitivity summary

Well Spacing	Same layer	Staggered
140	Lower EFS	Upper +lower EFS
280	Lower EFS	Upper +lower EFS
420	Lower EFS	Upper +lower EFS
700	Lower EFS	Upper +lower EFS
840	Lower EFS	Upper +lower EFS
980	Lower EFS	Upper +lower EFS
1120	Lower EFS	Upper +lower EFS

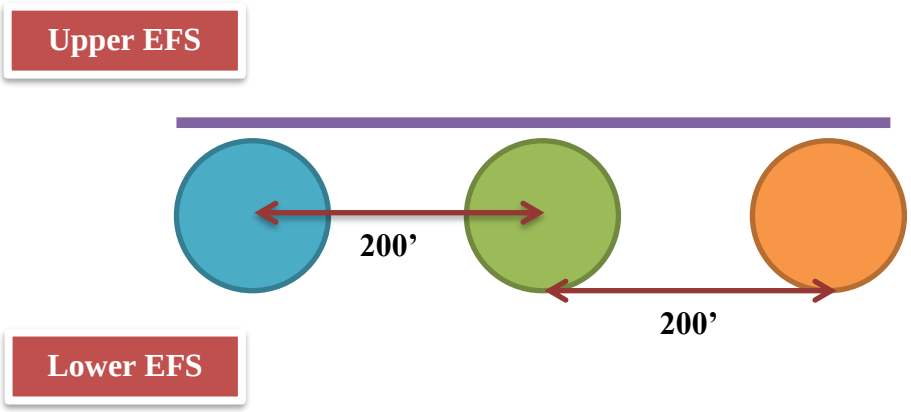

Figure 3.61. Example well configuration for same layer completion. All three wells are placed in lower eagle ford shale (EFS) section. Distance between two neighboring lower EFS wells is 200’. As well spacing is reduced these wells are more likely to be in rate interference.

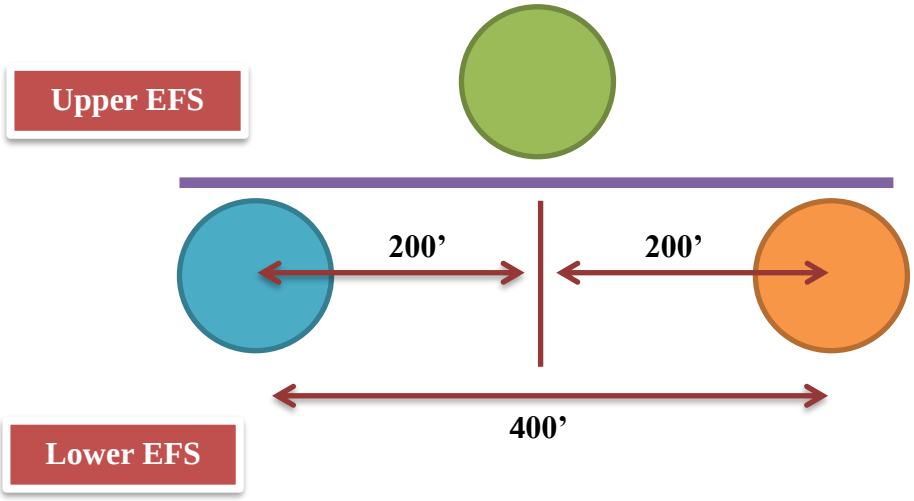

Figure 3.62. Example well configuration for staggered completion. Distance between adjacent lower Eagle Ford wells is 400’. Wells are less likely to be in rate interference in this configuration.

Assigning stimulated rock volumes

As the microseismic data is available for only 500’ spacing, assigning SRV’s is a critical component in deciding the ultimate recovery. The strategy adopted to assign the SRV to the downspaced case consisted on assigning for well spacing’s less than 500’ full EFS thickness to the wells.

Figure 3.63 shows the top of EFS (layer 1). It is observed that the fractures grow to the top of EFS. Also the full 500' between the wells are not drained. Hence, based on these two scenarios, full thickness of upper and lower EFS is assigned for all well spacing's. However, as full 500' is not drained in the base case scenario, the SRV is kept the same for all well spacing's above 500'. This is done under an assumption of same completions. Hence, keeping the completions same as full 500' is not stimulated in base case then it is highly unlikely that with further increasing the well spacing's with same completions SRV will be increased.

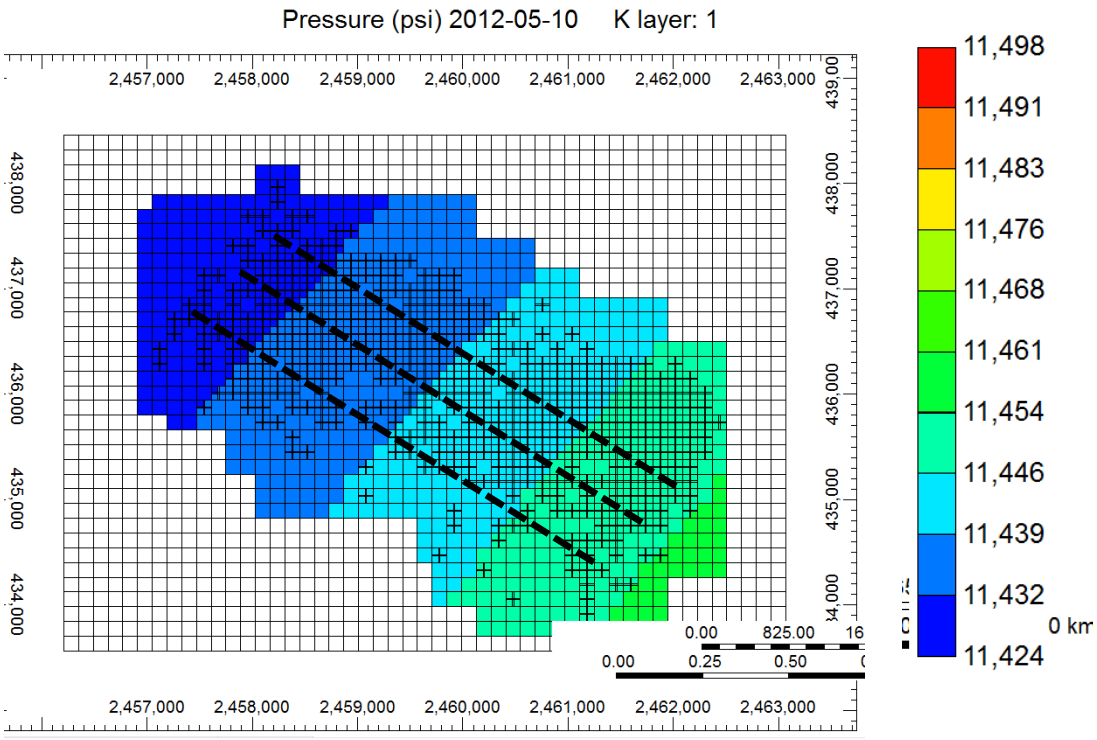

Figure 3.63. Fracture network created using micro seismic. Fracture networks are shown in black crosses. Layer under consideration is Eagle Ford top (K layer =1) and wells are in placed in lower Eagle Ford. Representative well locations are shown by dashed black lines. It is clear from the figure that hydraulic fractures grow from bottom of Eagle Ford till top of Eagle Ford.

Results Summary of all sensitivity cases

Figure 3.64 shows an example of same layer and staggered layer placement in the grid. For same layer all wells are placed in layer 9 which corresponds to lower EFS. For staggered wells one well is placed in lower EFS (layer 9) and one well in upper EFS (layer

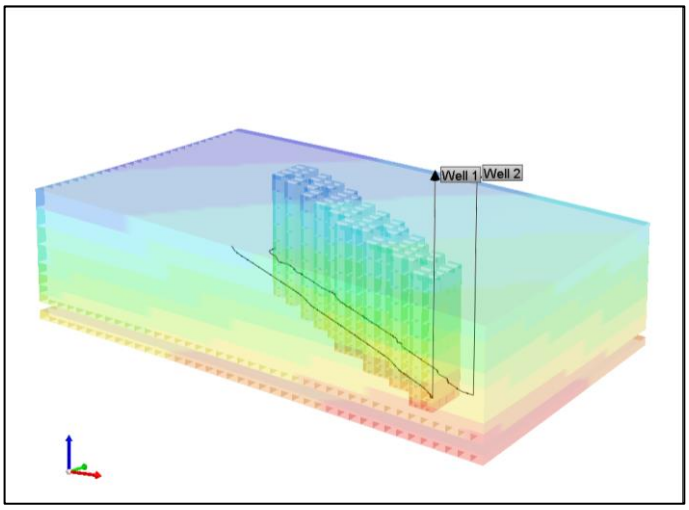

(a)

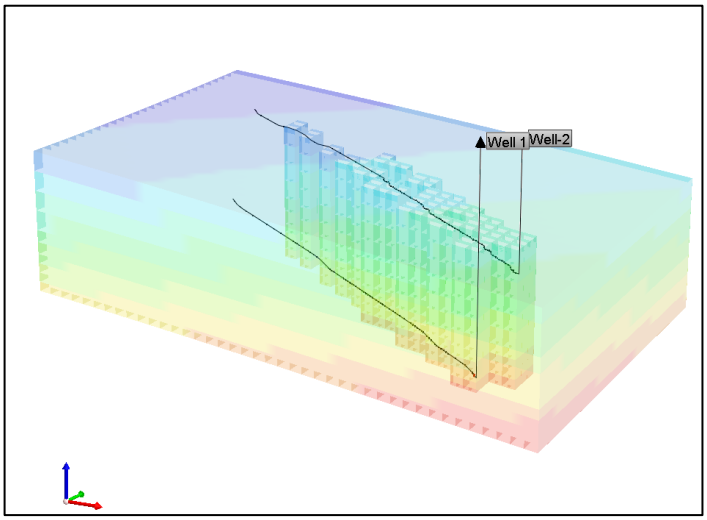

(b)

Figure 3. 64. Example SRV for 140 ft. spacing. (a) wells placed in same layer (lower EFS) (b) wells placed in staggered fashion (one well in upper EFS and one well in lower EFS). In both cases full thickness of upper and lower EFS is assigned to the SRV.

Table 3.13 and Table 3.14 summarize the results from all the cases in staggered and same layer completions. Same results are then represented graphically from Figure 3.65 to figure 3.67.

Table 3.13. Expected ultimate recovery (EUR) and recovery factor (RF) from same layer completions.

Same Layer				
Well Spacing	**Oil EUR**	**Gas EUR**	**OGIP(BSCF)**	**RF**
140	160	1.5	11	14%
280	250	3.6	22	16%
420	480	5.8	33	18%
700	440	5.4	39	14%
840	449	5.15	39	13%
980	465	5.35	39	14%
1120	435	5.1	39	13%

Table 3.14. Expected ultimate recovery (EUR) and recovery factor (RF) from staggered completions

Staggered				
Well Spacing	**Oil EUR**	**Gas EUR**	**OGIP(BSCF)**	**RF**
140	115	1.1	11	10%
280	225	3.1	22	14%
420	440	5.5	33	17%
700	425	5.25	39	13%
840	445	5.35	39	14%
980	455	5.45	39	14%
1120	420	4.9	39	13%

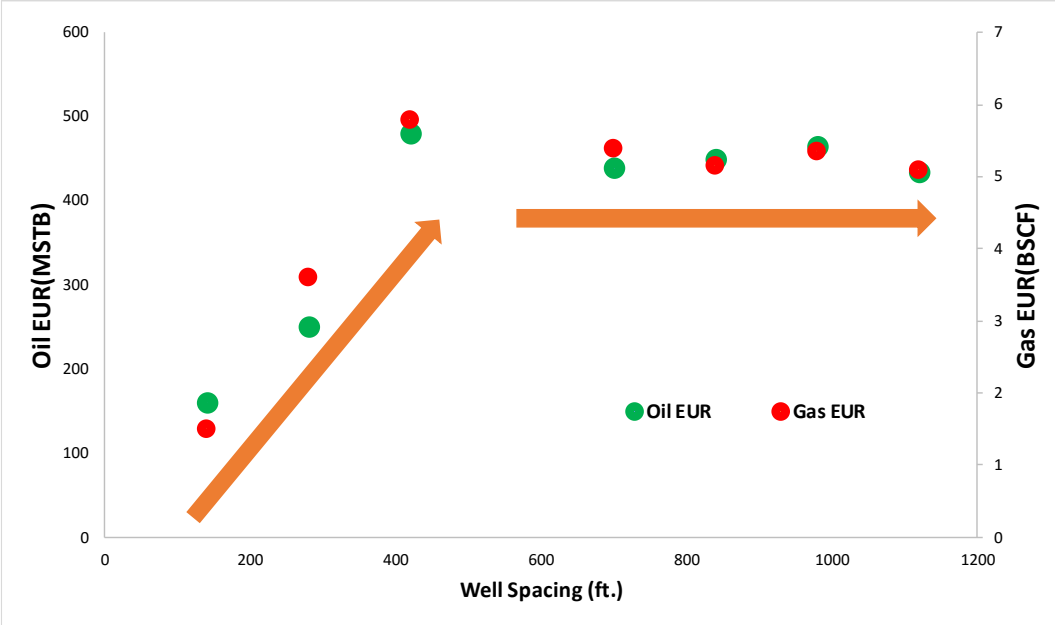

Figure 3.65. Oil and gas expected ultimate recoveries (EUR) for different well spacing's for same layer completions. The EUR's become constant after maximizing at 420'. There is a dramatic decrease in EUR's below 420'.

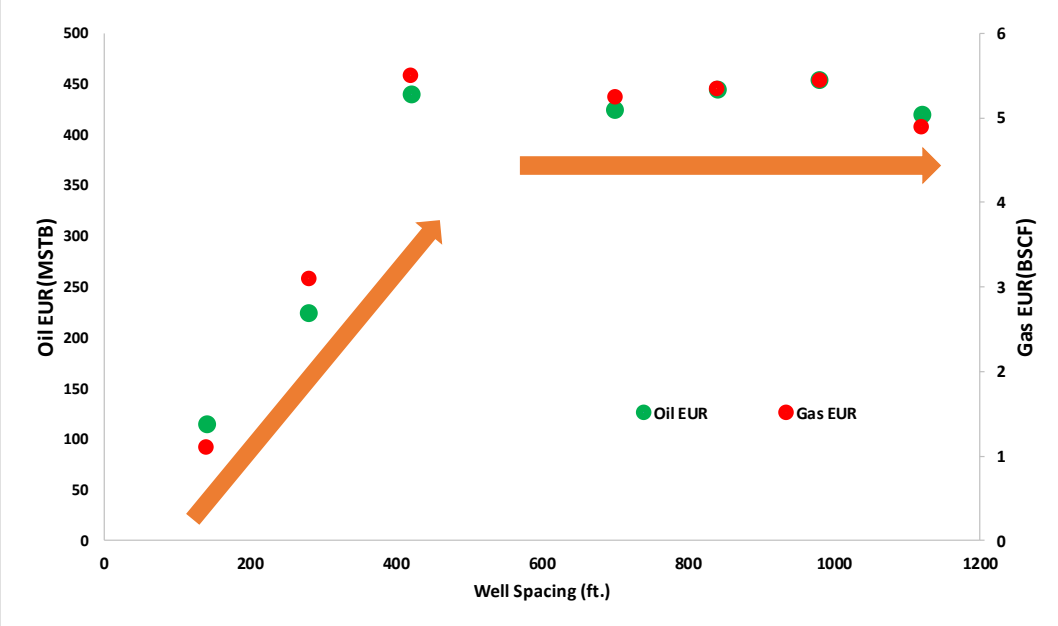

Figure 3. 66. Oil and gas expected ultimate recoveries (EUR) for different well spacing's for staggered completion. There is a dramatic decrease in EUR's below 420'. Above 420' ft. the EUR's become more or less constant. The deviations above 420' could be due to variations in geological properties in upper EFS due to presence of small scale heterogeneities.

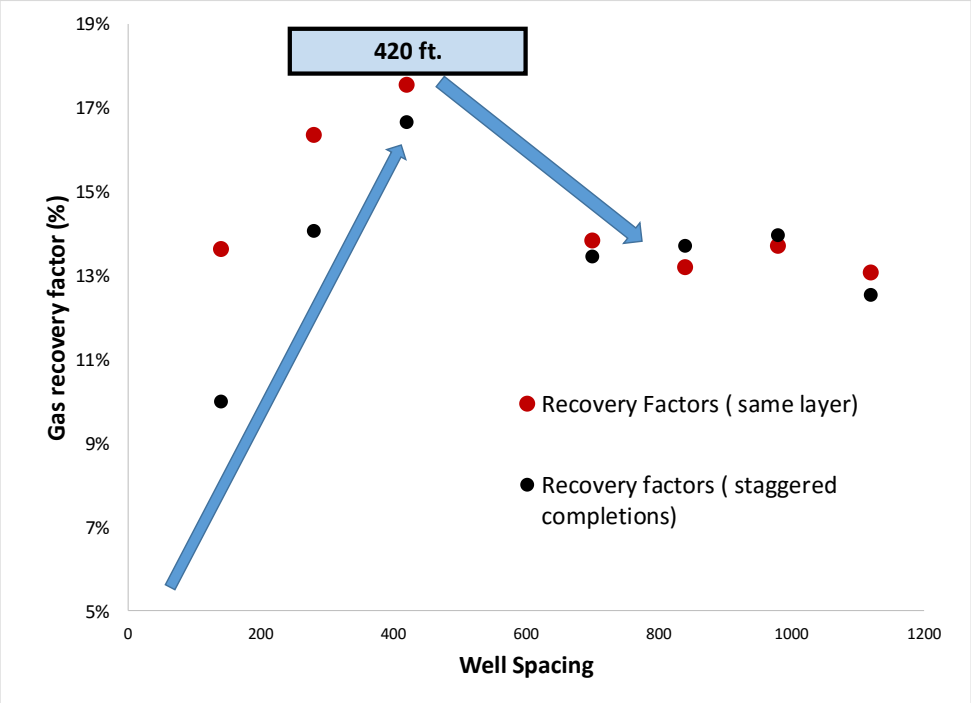

Figure 3.67. Recovery factor for staggered and same layer completions. Although there is a marginal difference in recovery factors at different well spacing's for same layer and staggered completions, a trend is clear. The recovery factors increase till a well spacing of 420' and then decrease and become constant. There is a dramatic decrease in recovery factors below 420'.

Figure 3.65 shows the oil and gas EUR trends for same layer completions and Figure 3.66 shows the oil and gas trends for staggered completions. In both figures, it can be seen that the EUR's maximize at 420' well spacing and become constant after that. In recovery factor plots, the recovery factors also maximize at a well spacing of 420' and decrease dramatically below this well spacing. Hence, 420' is the ideal well spacing in this case. From all sensitivity cases there are some critical insights can be drawn in the well spacing optimization:

(a) Dramatic decrease in recovery factors for 140' and 280' case

In the 140' and 280' spacing there is a significant loss in EUR's due to downspacing. This is attributed to the fact that after a certain well spacing, once all the area between the wells is stimulated pumping more proppant volumes just increase the fracture

conductivity and does not increase the SRV. This effect is discussed in section 3.6.6 These sensitivities show that once a limiting fracture conductivity is reached, the EUR's do not increase with more conductive fractures. The net SRV volume is the most important parameter to increase the EUR's and not the fracture conductivity.

(b) Completion optimization

In downspaced wells, reducing the amount of proppant could be one option to reduce the well cost and still achieve the same EUR's.

(c) Drilling all wells simultaneously to avoid future re-fracturing costs

Re-fracturing during development stage is an essential condition. Wells completed with single well PAD's, essentially act as pressure sink for the new adjacent well hydraulic fracturing stages and can suffer a "fracture hit". For older wells, with narrow spacing's, standard shut-in's may not alleviate the risk completely and hence they have to be refracture'ed before the new wells are completed to re-pressurize the system. To avoid the costs of refracturing in future, while downspacing all wells have to be completed simultaneously (preferably with zipper fracture).

(d) Staggered completion may not be a useful completion technique

As full net pay (upper + lower EFS) is assigned to both wells there is no advantage is attained in the staggered configuration as compare to the conventional same layer completion.

(e) Drawdowns must be optimized (due to less SRV, higher sustained rates may not be possible without losing oil EUR's due to condensate banking)

The shale reservoir with hydraulic fractures essentially acts as a volumetric reservoir and there is no contribution from outside the fracture network (pressure depletion images). Hence, if SRV is smaller, to sustain higher rates pressure drop's quickly leading to early condensate banking. Drawdown management hence become even more important at smaller spacing's. Otherwise an oil EUR deduction up to (10-20%) should be assigned to the wells.

(f) Longer laterals difficult to design due to uncertainty in trajectory (error ellipse)

It is almost impossible to design longer laterals with this spacing's. As the length of the lateral increase, the error associated with the probability to keep the well string in the zone also increases. Figure 3.68 shows this phenomenon when the lateral length increases the error margin to keep the wells in zone also increases. This can be alleviated with the more expensive tools (like rotary steerable systems) which anyways affect the economics of the well negatively.

(g) One upside from this well spacing could be extra SRV at the heels of the wells, if the completion design incorporates it.

It can be seen from the micro seismic that heel portion of the lateral is more stimulated than the toe portion of the lateral and hence if wells are downspaced there could be an extra stimulated SRV at the heel of the well.

(h) Preferential drainage around wellbore and staggered completions

Although the results from both same layer completion and the staggered completions are similar the absolute difference in EUR's can be explained on the basis of difference in geological properties. As discussed in section 3.4.3 the upper EFS is composed of small scale heterogeneities and along with poor petrophyscial properties such as low bulk density (less carbonate more clay), low density porosity and high water saturation as compared to lower EFS.

Figure 3.68 shows the drainage pattern of a staggered well completion. It can be observed that the lower Eagle Ford drains first the near wellbore region and then much later the upper Eagle Ford and even at the end of well life some of the upper Eagle Ford remains undrained. On the other hand, the upper Eagle Ford well drains the upper Eagle Ford first and then lower Eagle Ford region.

Hence, if the wells in upper and lower EFS drain their respective areas around the wellbore preferentially (and hence the name preferential drainage), well in upper EFS will have slightly less EUR than lower EFS and hence on a cumulative basis, wells in staggered completion will have a lower EUR's than wells in same layer completion. The effect will vary to the degree of heterogeneity.

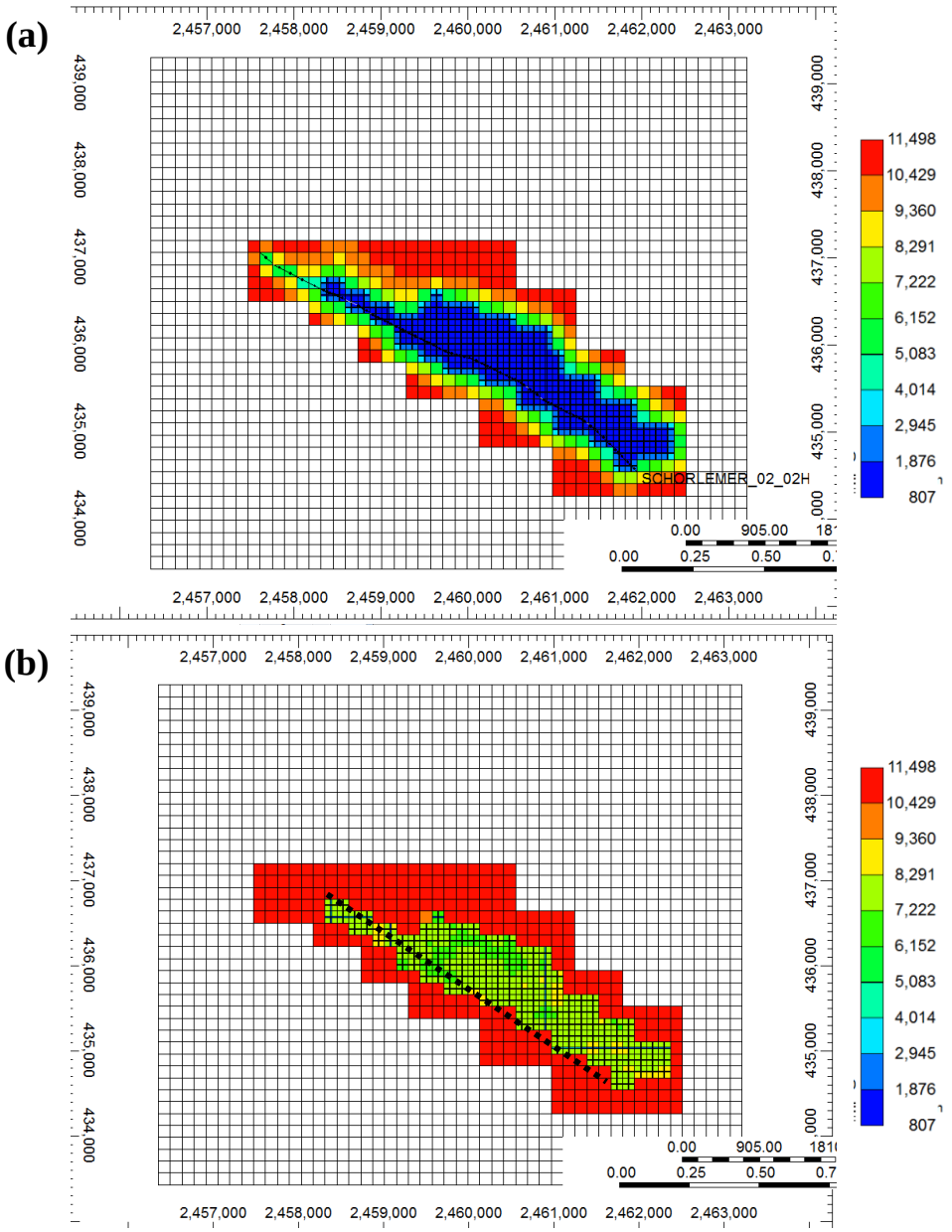

Figure 3. 68. Drainage pattern at the end of 30 years for well 1 placed in lower EFS. (a). Pressure profile at the end of well life in lower EFS (b). Pressure profile at the end of well life at top of EFS. It can be seen that the lower EFS well preferentially drains the lower EFS.

3.6.6. Fracture Conductivity Sensitivity

To see the effect of fracture conductivity in our case, in 280’ down spaced case fracture network effective permeability was varied. The output production profiles are then used to create type curves (TC) for different fracture conductivities. The output curves are summarized in Figure 3.69. It can be noticed that initial production is affected by the fracture conductivity. However, after some time all the cumulative volumes tend to converge asymptotically. Hence, the ultimate recoveries are not affected by the increasing the fracture conductivity beyond a certain point.

Hence, in any completion optimization program while downspacing, the stress should be on increasing the net reservoir contact area (SRV) instead of achieving higher fracture conductivities.

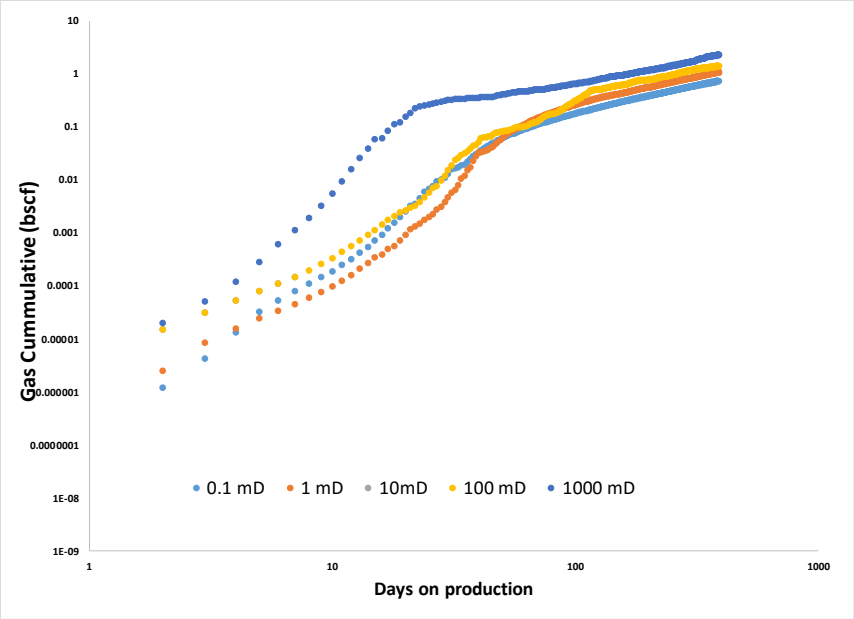

(a)

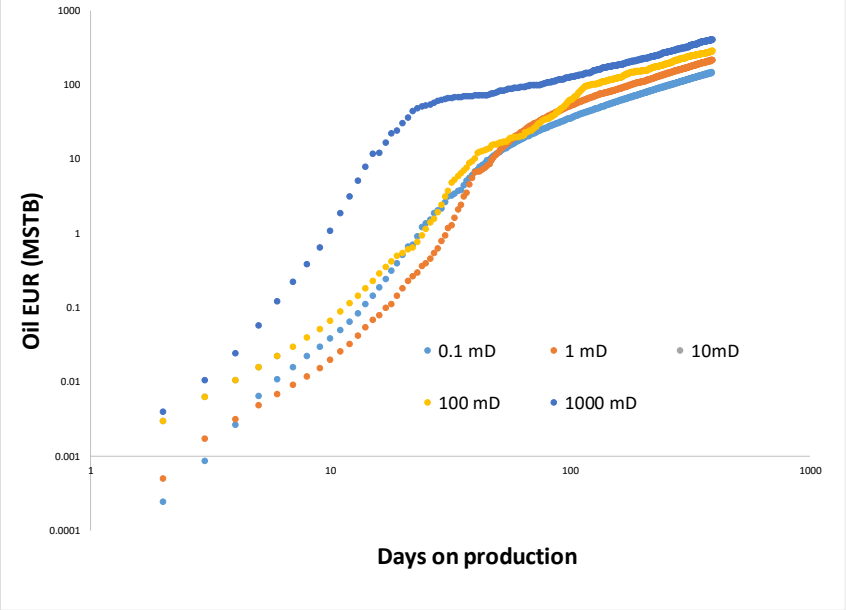

(b)

Figure 3. 69. Oil and gas cumulative volumes with time. a) Gas cumulative volumes in bscf with production time at various fracture conductivities b) Oil Cumulative volumes in MSTB with time. Plots indicate that first stem of the production i.e. initial 90 days is affected by the fracture conductivity. However, after some time all plots converge towards same cumulative volumes. This means increasing proppant volumes to achieve higher fracture conductivity may provide initial production profile but does not affect the ultimate recoveries.

3.6.7. Drawdown Management

It is discussed in section 3.6.4 that the shale reservoir essentially acts as a volumetric reservoir. This means if wells are down spaced SRV available to the wells also decreases. This means to draw the same production reservoir pressure drops quickly for wells with less SRV and may lead to early condensate banking.

To quantify the effect of drawdown management, the 280' model is run with different drawdowns. A very fine scale grid (21*21*3) is used to capture both the pressure depletion and retrograde condensation around the grid blocks (GB's). The model is run with a fixed SRV of 3.7 E+08 ft^3 under different drawdown controls. The drawdown is increased gradually until a point where retrograde condensation is observed.

The results at the beginning of well life (3 years into well life) and end of well life (30yrs) are summarized in Figure 3.70. It shows that when well is operated under the drawdown below 8000 Psi, no oil saturation around the wellbore is observed. However, there is a sudden condensate banking around the wellbore below the 8000 Psi drawdown. Hence, the well has to be operated below this drawdown to avoid condensate banking. This also implies for any well first the SRV has to be estimated by direct methods like microseismic or indirect methods like rate transient analysis. Based on the SRV the choke management (or drawdown management) strategy needs to be custom tailored for each well even if they are on the same PAD.

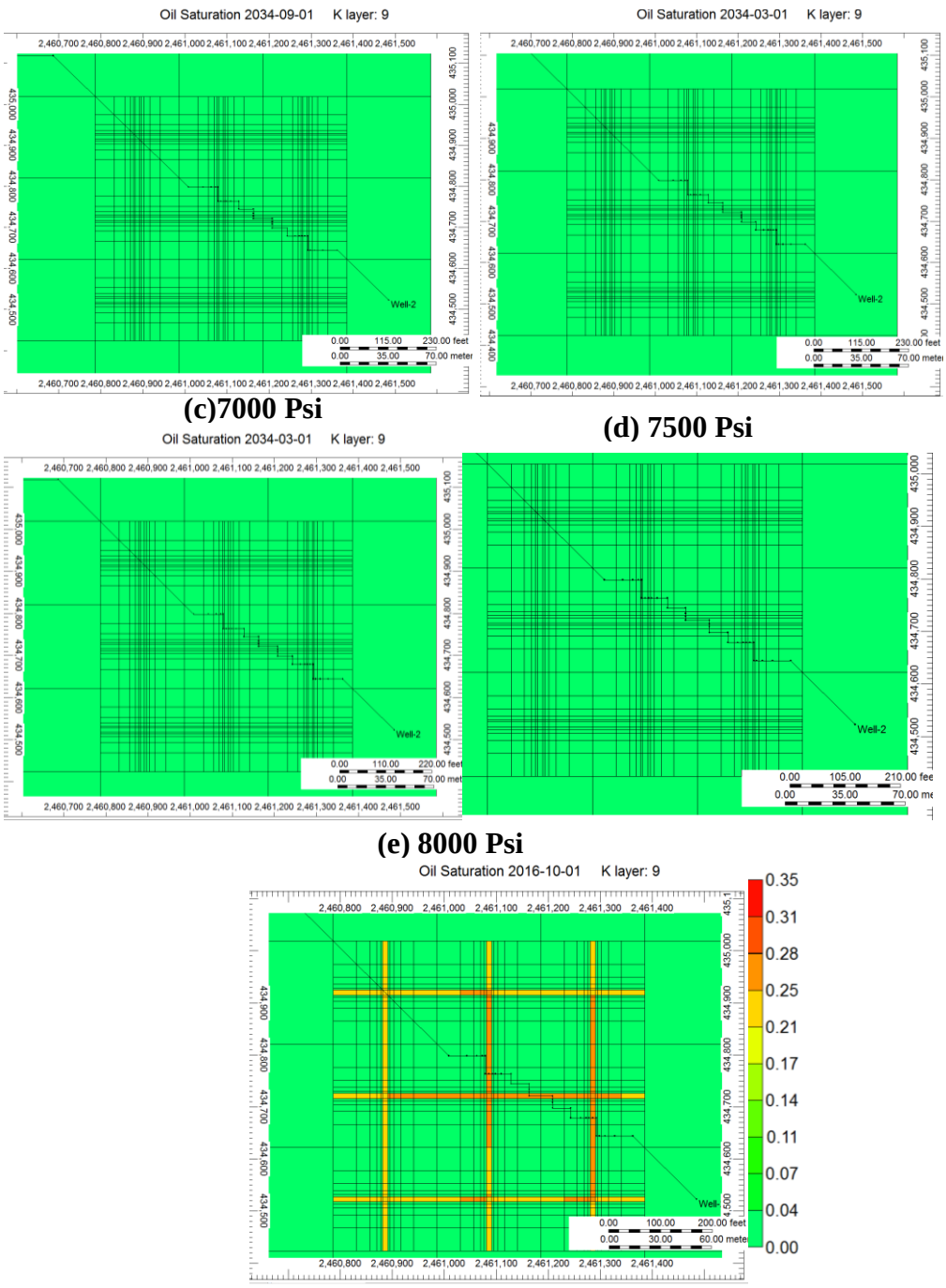

Figure 3.70. Oil saturation around the wellbore at different drawdowns at the end of 30 years. From left to right (a) for well operated under constant drawdown of 5000 psi as primary constraint (b) for well operated under constant drawdown of 6000 psi as primary constraint. (c) for well operated under constant drawdown of 7000 psi as primary constraint (d) for well operated under constant drawdown of 7500 psi as primary constraint (e) at end of 3 years for well operated under constant drawdown of 8000 psi as primary constraint. It can be observed that an early condensation occurs around the wellbore for a threshold drawdown of 8000 psi.

4. Multivariate Statistical Techniques

4.1.Introduction

For this portion of thesis, statistical techniques are used to quantify the EUR and hence the recovery factor from downspaced wells. A total of 1514 horizontal multi-fractured wells from Dewitt County, TX are chosen. Eagle Ford shale in this county offers a significant amount of wells with substantial well history and the condensate gas ratio (CGR) range is similar to our wells.

These wells are clustered into type curve areas and the Arp's decline parameters i.r. initial production (IP), decline (D) and b factor (b) are correlated with relevant parameters including well spacing. The method used to correlate these parameters is multiple regression.

4.2.Methodology

Figure 4.1 elaborates the area of interest (AOI) and the wells chosen for analysis. The area of interest for our study is the Dewitt county. From Figure 4.1 also shows the location and stick maps for all the wells chosen for analysis. A total of 1514 wells are selected for the analysis and all wells are horizontal wells completed with a multi-fracturing scheme. The analysis includes all wells in this county which are brought on production up to march 2016. A public information database drillinginfo® is used to extract the production data from these wells. The figure shows an overlay of the well shape files with the county outline shape files.

The overall production trend from all of the wells is demonstrated in Figure 4.2. The production is normalized to the peak production in Figure 4.2. A drop towards end is due to the reduction in well count.

In a conventional type curve (TC) analysis first the AOI is divided on certain number of criterion such as geological units, condensate gas ratio etc. Within the clusters wells are further subdivided and a decline trend is established in the well clusters. Then Arp's parameters (discussed in chapter 1, equation xxx) i.e. initial production (IP), decline (D) and b factor (b) are correlated with the parameters which correlate the best with Arp's parameters. This approach however, has many limitations. An example is elaborated in Figure 4.3. The figure shows that the Arp's parameters correlate to multiple variable simultaneously and hence the problem of generating type curves is not a univariate problem.

In this thesis following workflow is followed to generate the type curves:

(a) Wells are first clustered using multiple parameters simultaneously to generate type curve areas. Methods such as neural networks and k-means clustering is used to cluster the wells.

(b) Flow regimes in the wells are identified with the help of a combination of reciprocal rate- cumulative plots as well as type curves

(c) Decline curve analysis is performed for the wells which are in boundary dominated flow (BDF)

(d) 50% of the wells in BDF are then selected for multiple regression

(e) Multiple regression is run on 50% of the wells to obtain regression equations for Arp's parameters

(f) Using the type curve equations generated from 50% of the wells, EUR's are predicted for rest 50% of the wells. The predicted EUR's are then compared against

the EUR's obtained from actual decline curves and errors in prediction from statistical method is quantified.

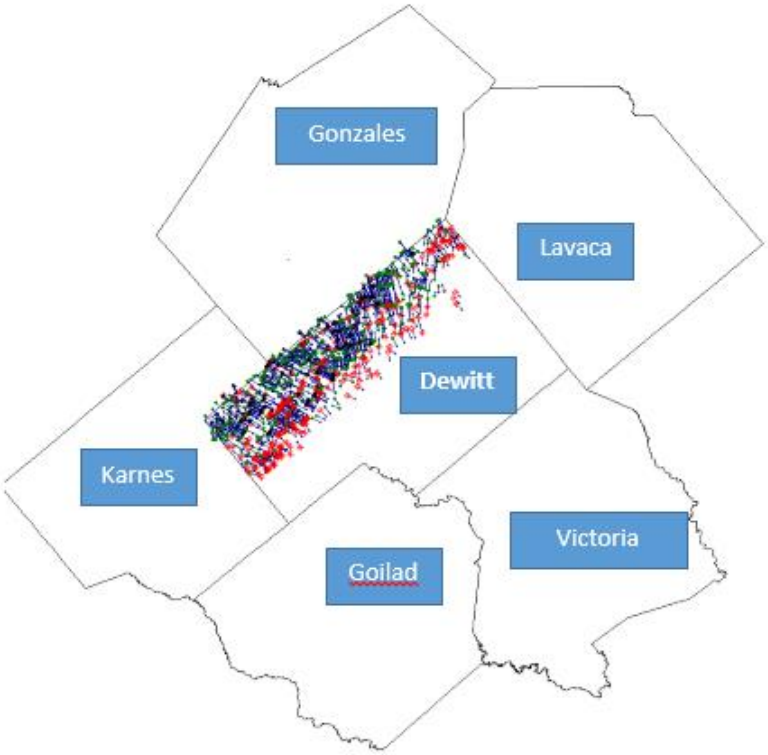

Figure 4.1. Area of interest for analysis. Overlay includes selected wells and surrounding counties.

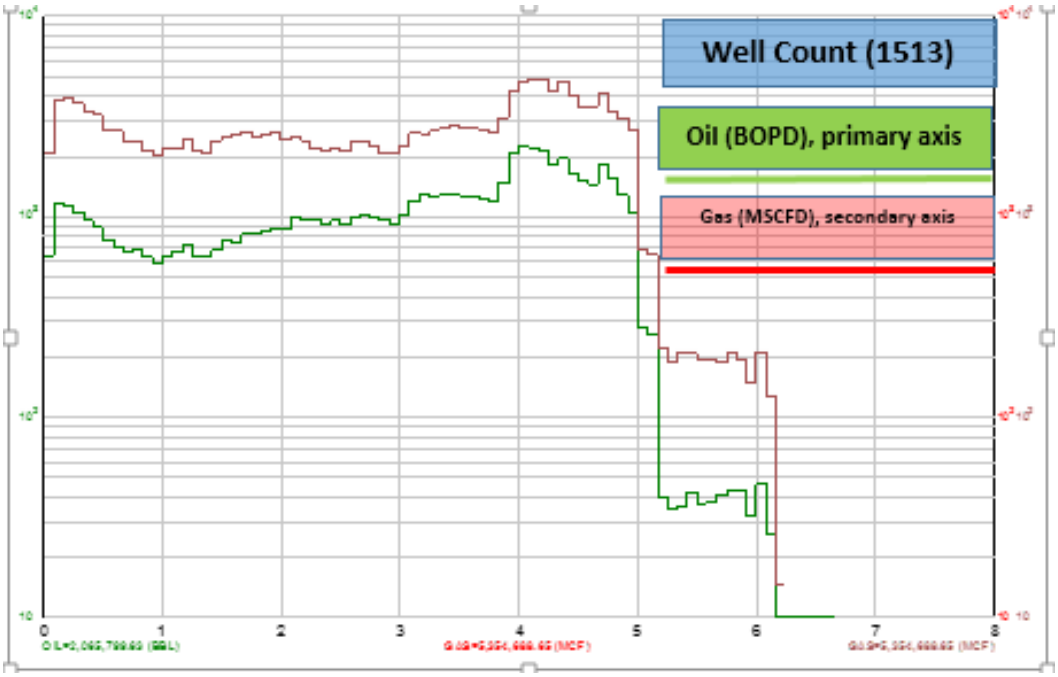

Figure 4.2. Production trend (all wells). Data normalized to maximum rate.

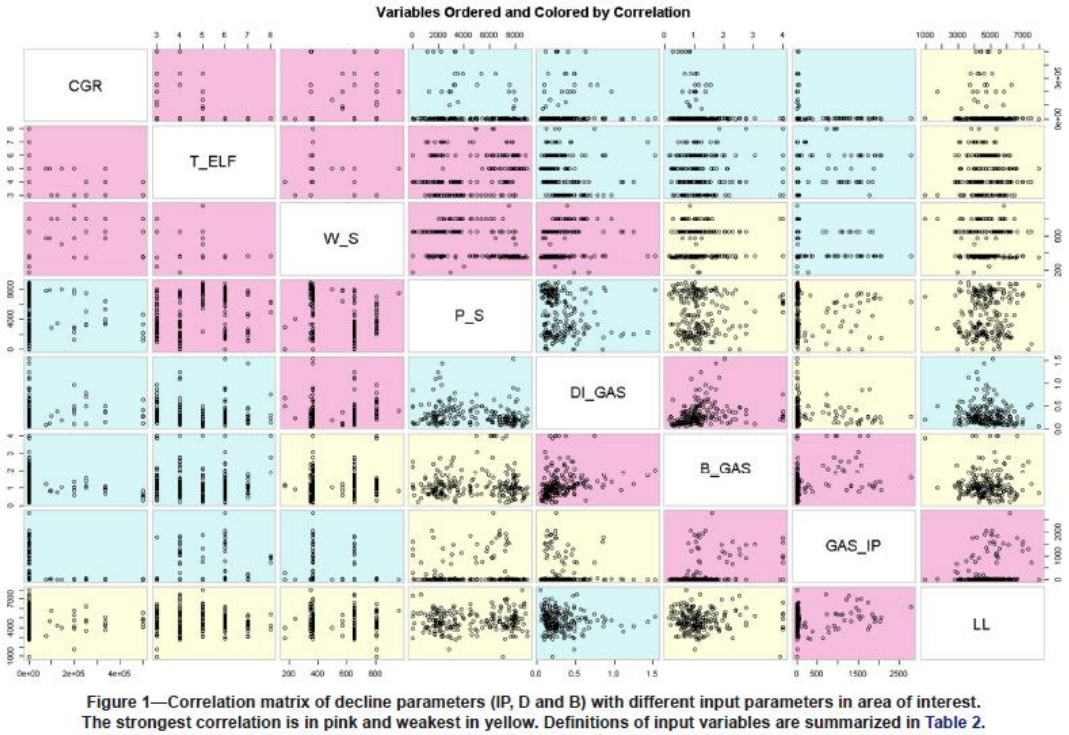

Figure 1—Correlation matrix of decline parameters (IP, D and B) with different input parameters in area of interest. The strongest correlation is in pink and weakest in yellow. Definitions of input variables are summarized in Table 2.

Figure 4.3. Correlation matrix of Arp's parameters with multiple parameters simultaneously. It can be observed that the Arp's parameters correlate with multiple parameters and hence problem statement is multivariate.

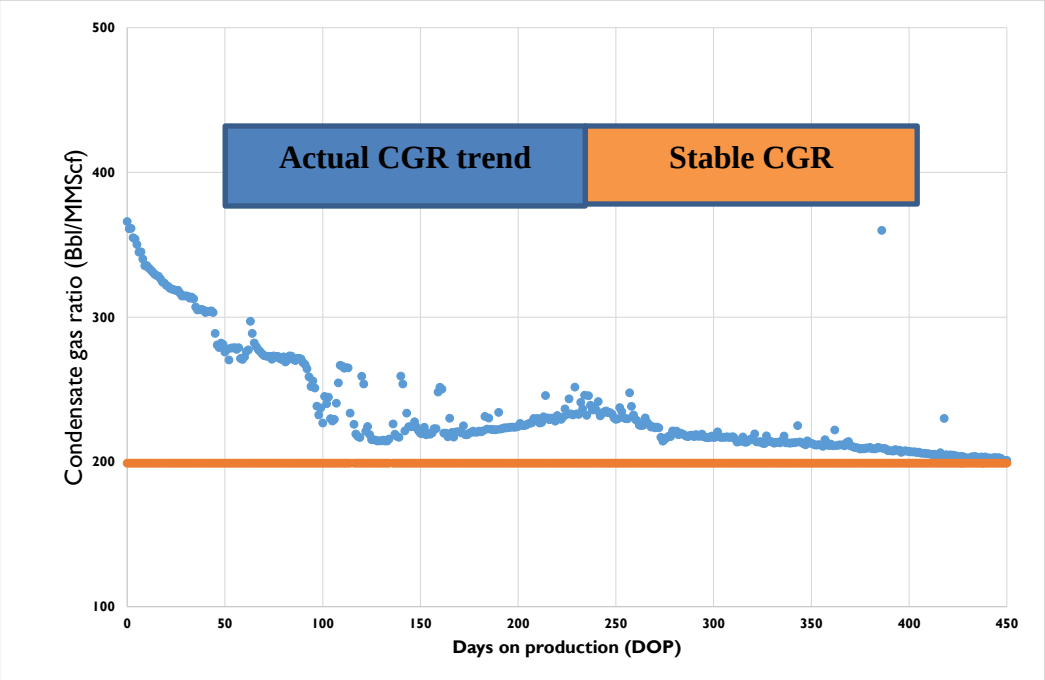

Figure 4.4. Condensate gas ratio (CGR) trend of a typical well in Eagle Ford shale. It can be seen that the CGR starts with an initial high value and gradually stabilizing.

4.2.1. Clustering Parameters

The clustering of data to generate the type curves for first step is done using following parameters:

a. Flowing pressures: The flowing pressure recorded at stabilized flow rates (IP tests) is a good indicative of actual reservoir pressure. In case of wells which are flowing through the casing, casing pressure is taken. For wells with tubing flow, tubing pressure is used. This way a pressure variation across the lease is mapped. As the dataset is taken from a public database, a detailed geology is not available. In case a detailed geological information is available this can be further fine-tuned by geology. For example, pressure variations across a major fault mapped on seismic, or an area of the reservoir where seal is not intact and hence unusually low pressure.

b. Shut in pressures: Shut in pressures similar can be utilized similar to the flowing pressure. Although like conventional analysis, it cannot be utilized to derive any meaningful parameters like permeability or skin due to supercharging of reservoir. It can further bolster the confidence in pressure profile across the reservoir. An initial reservoir pressure can also be taken if the data is available for significant number of wells. As post fracture reports for limited number of wells is available, extended shut in pressures are taken as a proxy.

c. Condensate gas ratio (CGR): CGR (BBL /MMSCF) is an important parameter that influences the flow potential in the reservoir. CGR values can not only define the fluid type in the reservoir but combined with reservoir pressures are strong indicatives of reservoir drive mechanism and hence the EUR's. However, what CGR value to take is very important for the analysis.

A typical CGR trend in condensate well is shown in 4. It is clear from the plot that the CGR trend gradually decreases and stabilize at a constant value. It can be because of multiple reasons including but not limited to: flow stabilization (from linear to boundary dominated), compositional gradient within the reservoir or gradual fracture tip closure i.e. initial production from upper EFS with high CGR gradually moving to lower CGR of lower EFS.

Hence, using cumulative CGR's or initial test CGR's to define long term production and hence the EUR's is not a wise choice. In this study all CGR values used are the stable CGR's. For wells in which CGR has yet not stabilized, CGR values are borrowed from the adjacent wells for best approximation of stable CGR's.

d. Flow potential (productivity index): To analyze the flow potential of the wells, use of cumulative volumes has been avoided in this study. Cumulative volumes not normalized by time and pressures are a poor choice for flow potential. As a detail pressure history for the wells is not available on drillinginfo®, the IP test values are used. The wells are first classified into oil or gas wells on the basis of CGR.

Wells with CGR<400 are considered as gas wells and wells with CGR> 400 are considered as oil wells. Fine subdivisions (dry gas, lean gas, rich condensate, light oil etc.) are not done at this stage. Once, the wells are classified into oil or gas wells the major phase stable rate during the test is taken as flow rate from the well. This is then divided by drawdown (Stabilized Shut-in pressure – Flowing tubing head pressure). This tubing head pressure (THP) based PI's are then taken for the wells. Out of 1514 wells, IP tests are reported in only 945 wells. For other wells, PI's are taken from immediate neighboring wells.

e. Oil and gas gravities: Oil and gas gravities are indicative of the fluid type. Surface oil and gas gravities are included in the clustering process.

4.2.2. Clustering Methodology

Wells are then clustered using the 5 parameters described before. The data file obtained is imported into R (software environment for statistical computing and graphics) to use Unsupervised Clustering Techniques, in this case, self-organizing maps (SOM) and k-means. These unsupervised learning algorithms are used for exploratory data analysis to find hidden patterns or grouping in data.

The objective in k-means is to define for each cluster a centroid. Then, each data point belonging to the set is compared and associated with the nearest centroid. After the initial grouping, the centroids are re-calculated as barycenters of the clusters resulting from the previous step. The centroids change their location step by step until no more changes are done.

On the other hand, self-organizing maps work as a data visualization technique that reduces the dimensions of a data set through the use of self-organizing neural networks. The map units are allowed to change themselves by learning to become more like to the samples from the data they are compare with. A map of 1 or 2 dimensions is created to plot the similarities of the data by grouping similar data items together.

First an estimate of the appropriate number of clusters required using a k-means algorithm is determined. This is done by calculating the sum of squares between each cluster initially assuming different numbers of clusters, and looking for an “elbow-point”. Figure 4.5, exhibits the results obtained from the algorithm. The change in the slope starts around 5 clusters. But the ideal number may be anywhere between 5 and 9 clusters. For the purpose of defining the groups of wells a number of 5 clusters was selected.

After defining the number of clusters, the k-means algorithm is applied to the data specifying an output of 5.

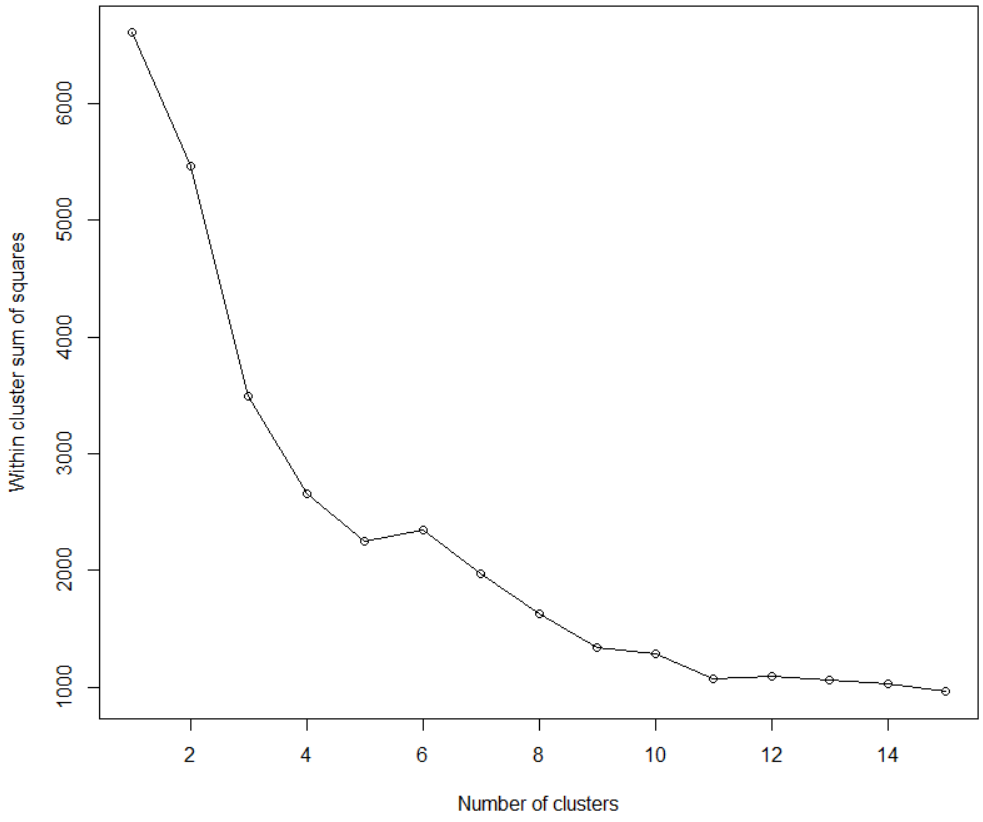

Figure 4. 5. Number of clusters from k-means. The elbow point can be observed at number of clusters=6.

Cluster analysis for k-means is used to plot the group results in 2 dimensions using the first principal components, as shown in Figure 4.6**.** The principal components selected explain around 64% of the variability, which means that they are a good representation of all the parameters selected.

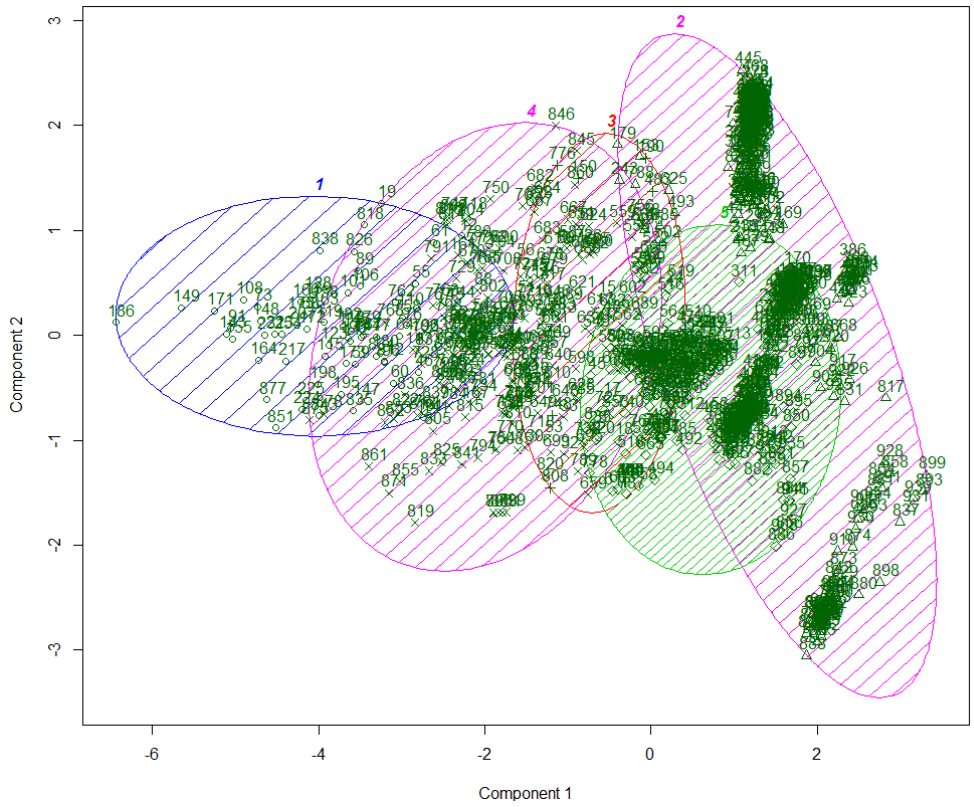

Figure 4.6. Cluster plot using principal components.

As a clustering alternative a Self-Organizing Map (SOM) using the R package: Kohonen is used for training purpose. The SOM is a map of size of 9x9 with a hexagonal topology, the number of times the complete data set is presented in the network is 500 (rlen). The learning rate (indicating the amount of change) declines from 0.05 to 0.01 over the number of updates. The variables are standardized with the mean and standard deviation for the model construction.

Error! Reference source not found.7. shows the training progress of the map over t ime (iterations). The y-axis shows the distance from each node's weights to the samples represented by that node. This distance should reach a minimum plateau; in this case the plateau is reached around 200 iterations.

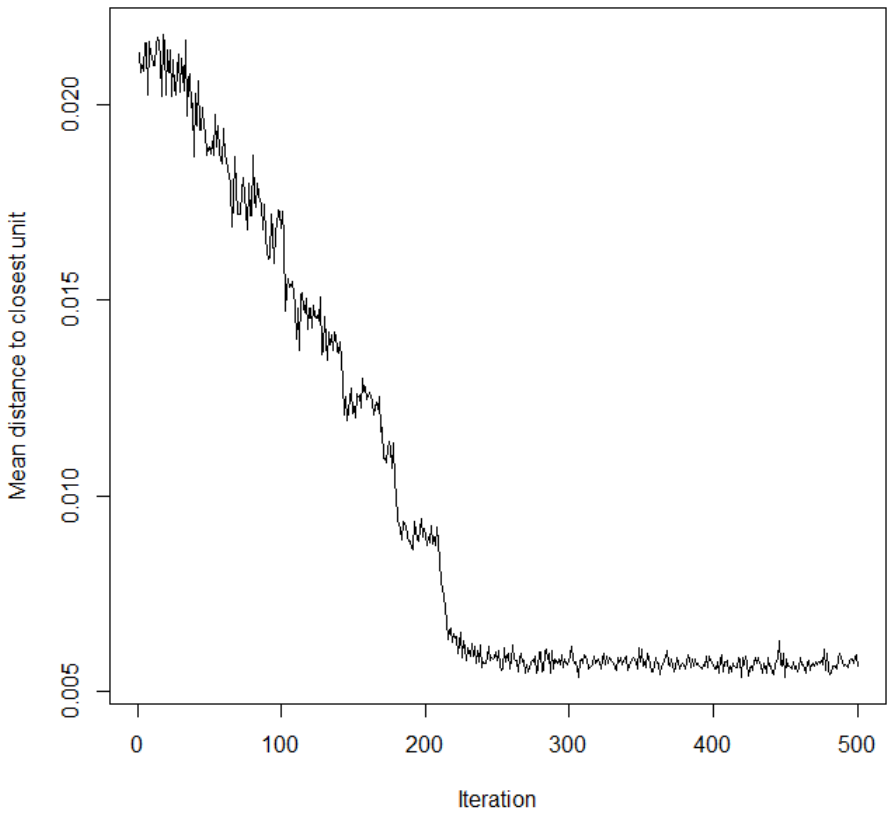

Figure 4.7. SOM Training Progress. The process flattens out after 200 iteration.

Error! Reference source not found.8. shows the counts plot. The color in each c ircle shows the number of times the unit was a best matching unit, for example, a unit colored in yellow was best matching unit for around 30 counts or times. The counts plot measures the map quality, ideally the sample distribution should be uniform. If there is large count value in a region of the map, a larger map should be use. For this study a network size of 9X9 was selected, which is adequate for the data set size.

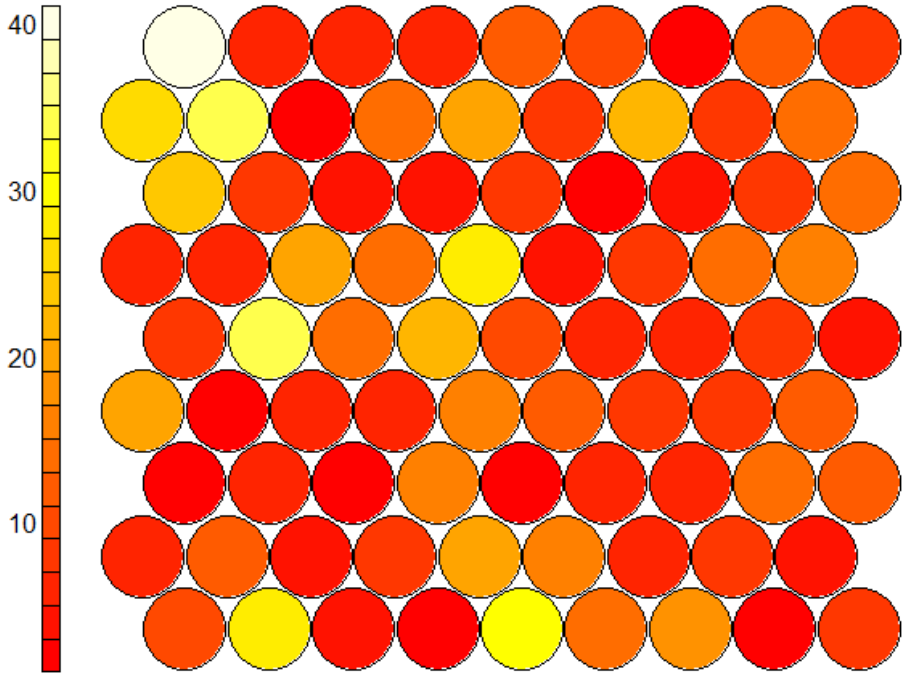

Figure 4.8. SOM counts plot

To understand better the map obtained the codes plot shown **Error! Reference s ource not found.**9 is used. Which is a fan diagram representation for each parameter weight in the nodes. From the plot we can see patterns in the distribution. The data points with high flowing and shut-in pressures are located in the left upper corner, while the data points with high oil density are located in the left lower corner.

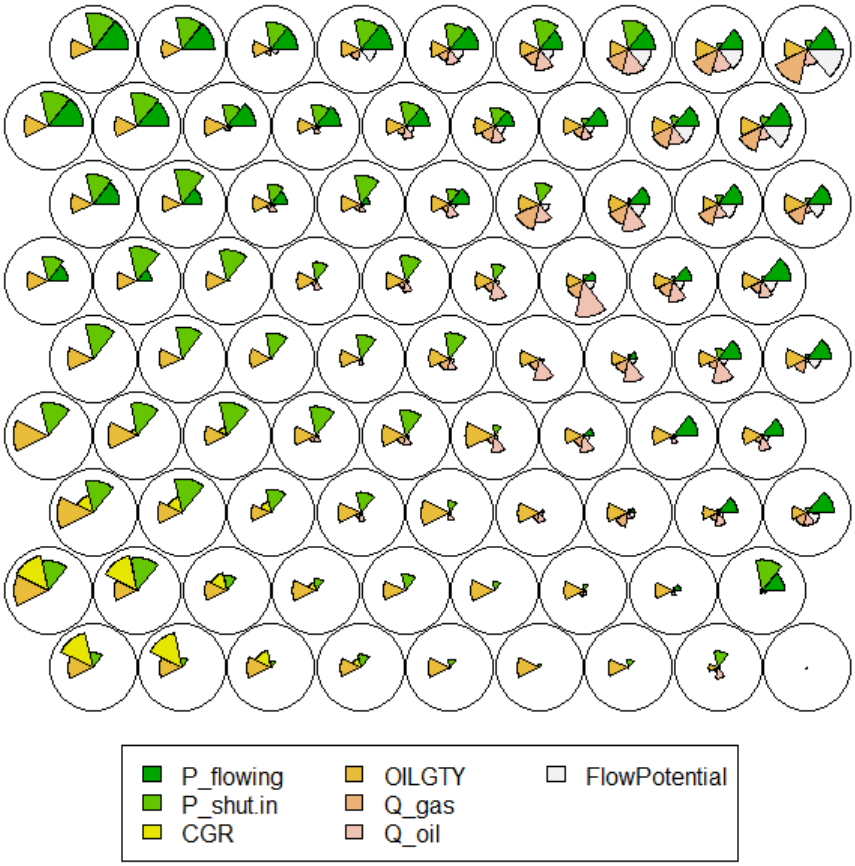

Figure 4.9. SOM Codes plot in fan diagram format.

Selecting the boundaries for each cluster is a subjective task that can be based on the visualization of the plots shown above. For these data set, a number of 5 clusters were selected. Then, we use hierarchical clustering from the Kohonen package for the classification. The resultant clusters are shown below in **Error! Reference source not found.**10.

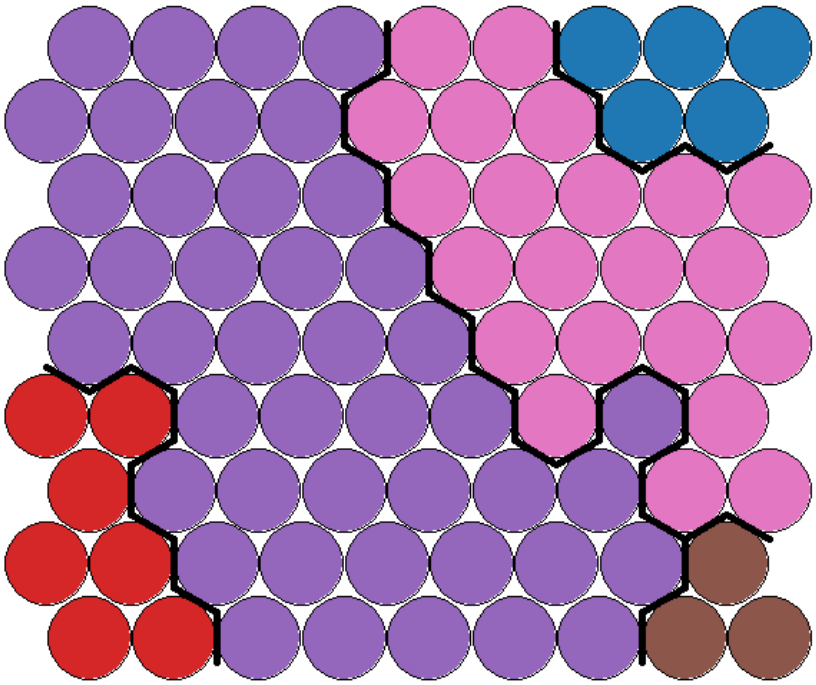

Figure 4.10. Clusters obtained from hierarchical clustering on the SOM nodes.

The final selection of Clustering method is based on following criterion:

a. Predictability

b. Data distribution

Both methods give similar predictability (~70%). However, with k means the classification suits the well parameters analyzed and is more efficient than the hierarchical clustering used in SOM. Hence k means clustering is selected for clustering the data. However, the maps generated with SOM, give an idea of the data distribution and the relations between the parameters. The clustered wells or type curve groups are shown in Figure 4.11.

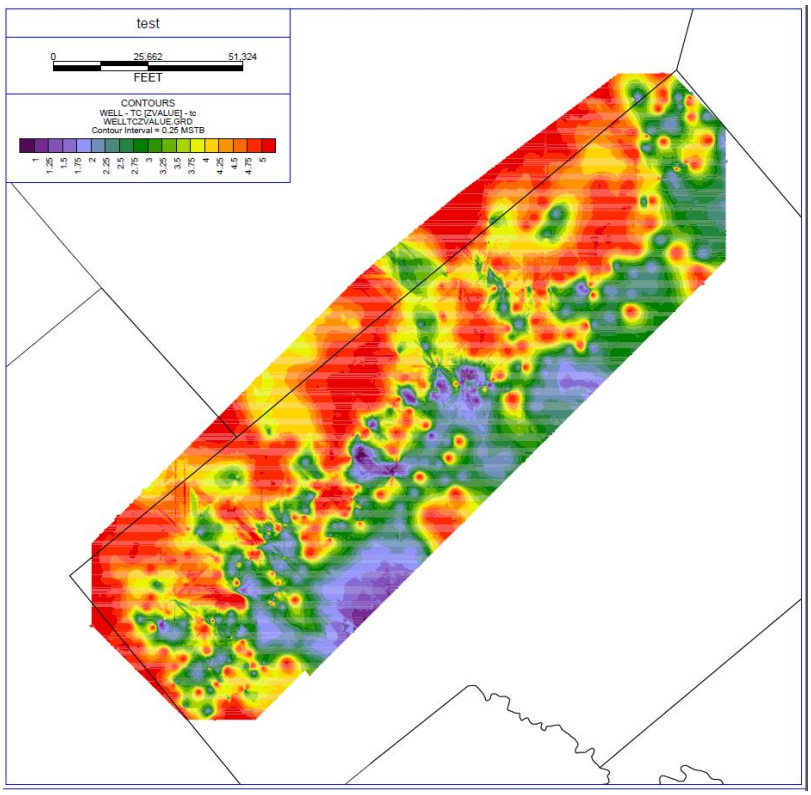

Figure 4.11. Type curve classification (1-5) based on k-means clustering. Type curve contours overlay with county outline. Majority of the area is type curve area 5 (rich condensate) but variations within type curve areas can be observed as the type curves are bases on cumulative effect of multiple parameters.

Before decline fitting the individual wells, it was essential to confirm if the wells are indeed in boundary dominated flow (BDF). With a limited dataset, there is a limitation on methods that can be applied to identify the wells in BDF. In this study a combination of Fetkovich type curves (rate –time) and reciprocal-rate cumulative plot are used. These are elaborated in Figure 4.122 and **Error! Reference source not found.**3.

Fetkovich type curve do not require pressure data and are ideal in this situation. Reciprocal –rate cumulative curves are used in conjunction with the type curves. One by one all 1514 wells are tested for flow regime identification.

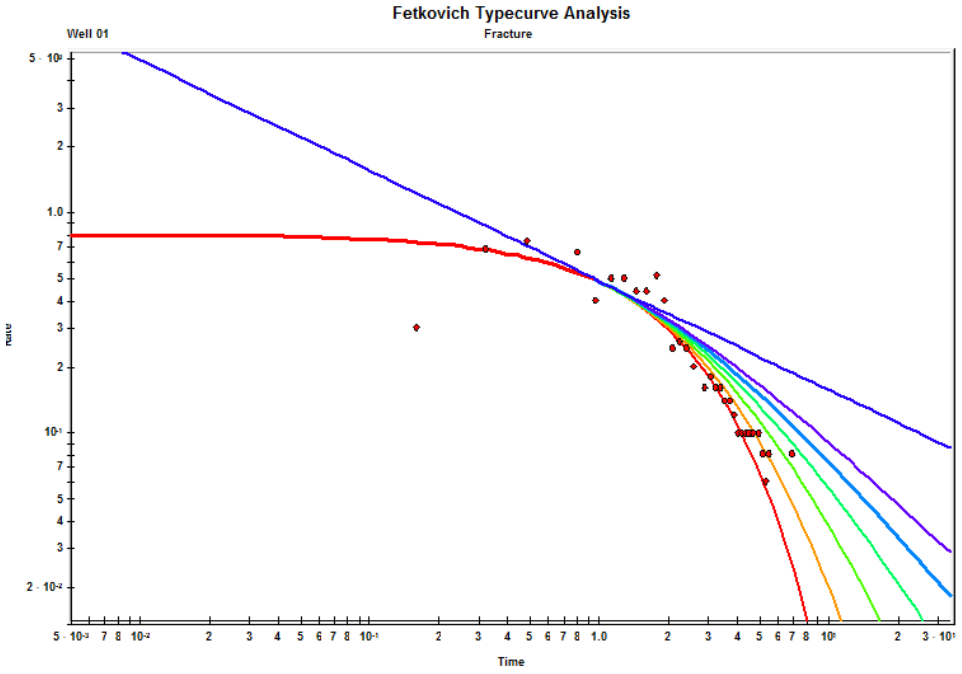

Figure 4.12. Fetkovich type curve analysis

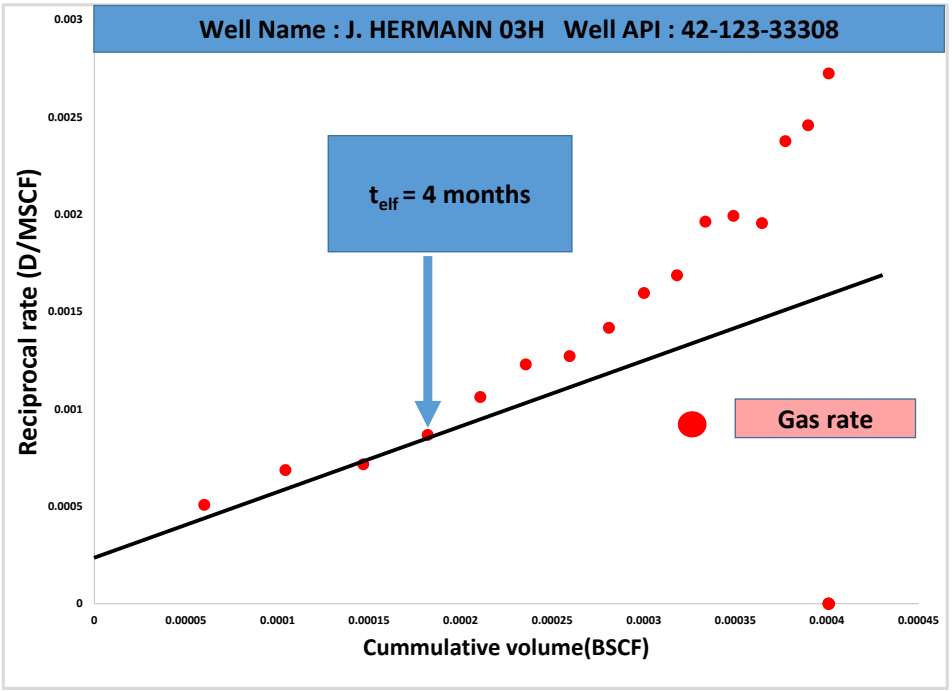

Figure 4. 13. Reciprocal rate-cumulative diagnostic plot

4.3. Results

Once all the response variables and input variables are set, a principal component analysis (PCA) is done to reduce the number of variables for multiple regression under each type curve group. With CGR range in concern type curve 5 was found to be most suitable for application. Principal components for this group are summarized in Table 4.1 and in Figure 4.144. Table 4.2 summarizes the definition of the variables.

Multiple regression results are summarized in Table 4.3 for the major phase (gas). P values of the PC's show that the variables chosen can be used as very good predictor of type curve parameters. But the R^2 values are not close to 1. This is a classic case of low P, low R^2 and the direct interpretation of this case is the insufficient number of variables chosen for analysis. In this case, we have used a limited dataset available on public domain, however for operators with significant dataset, additional variables such as initial reservoir pressure (from multiple wells), petrophysical parameters from significant number of wells, rate transient analysis parameters, and proppant volumes can increase the R^2 values significantly.

The IP, declines and b factors are then generated for Arp's hyperbolic equation with fixing the lateral length = 5000' (our simulation wells average lateral length), CGR = 220 BBL/MMSCF, Telf =90 days or 3 months and extended shut in pressures = 8000 Psi. Well spacing is then varied at 200', 400', 600', 800' and 1000'. The results are summarized in Table 4.4. From table 4.4 it can be seen that the recovery factors maximize at a well spacing of 400' and well spacing of 400' is optimal.

Table 4.1. Input parameters derived from 5 principal components. Loading of each input parameter can be seen on every principal component

Parameter	PC1	PC2	PC3	PC4	PC5
T_ELF	-0.5988	0.149242	-0.05741	0.364461	0.695006
W_S	0.605825	-0.07519	-0.10285	-0.34	0.707914
P_S	-0.39865	-0.1677	0.601563	-0.66541	0.091165
LL	0.004188	-0.94816	0.068709	0.305764	0.052545
CGR	0.339806	0.211996	0.7871	0.464017	0.068931

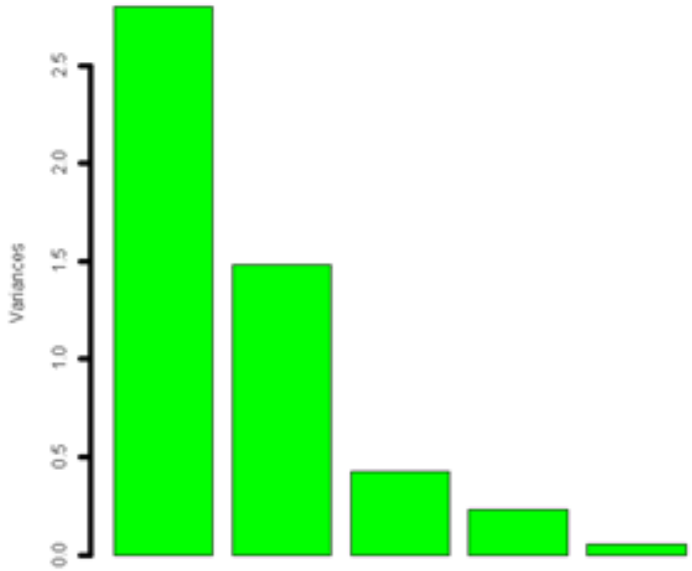

Figure 4.14. Scree plot for five principal components. Two or three principle components are enough to represent the variability in the dataset.

Table 4.2. Definition of the input variables used for principal component analysis.

Variable	Definition
T_{ELF}	Time end of linear flow
WS	Well spacing
P_S	Extended shut-in pressure
LL	Perforated lateral length
CGR	condensate gas ratio

Table 4.3. Example multiple regression results summary for type curve 5.

Type curve 5			
GAS IP	**PC**	**p value**	**R^2**
	1	7.00E-02	0.65
	2	2.63E-03	
	3	2.15E-02	
GAS D	**PC**	**p value**	**R^2**
	1	8.41E-04	0.6
	2	1.14E-01	
	3	1.11E-01	
GAS B	**PC**	**p value**	**R^2**
	1	5.49E-02	0.68
	2	8.54E-01	
	3	1.58E-02	

Table 4.4. Expected ultimate recovery (EUR) and recovery factor summary for different well spacing's.

Well Spacing	**Gas EUR(BSCF)**	**OGIP(BSCF)**	**RF**
200'	0.65	15.8	4%
400'	2.75	31.62	9%
600'	2.8	39	7%
800'	3.1	39	8%
1000'	3.2	39	8%

Conclusions

In this study analytical models indicate that the optimal well spacing in the AOI is 118 ft. The results are based on a horizontal well with equal fracture half-length model. Hence, the direct conclusion from analytical models are the optimal well spacing is ~250 Ft.

Rock typing in the area indicate 4 different rock types. A 3D lithological model created from the well logs indicate that the upper and middle Eagle Ford shale are more heterogeneous composed of small scale heterogeneities. Lower Eagle Ford on the other hand is a more continuous interval. Lithology constrained porosity and water saturation indicate that lower Eagle Ford is a more prolific area as compared to upper or middle Eagle Ford. Micro- seismic data indicate that even if the wells are placed in lower Eagle Ford the fracture networks grow till the top of Eagle Ford interval.

History matching of historical production data shoes uneven drainage areas with more drainage on the heel side of the lateral. Sensitivities on the history matched model indicate that a well spacing of 420 ft. maximizes the recovery factors and hence is the optimal well spacing. Sensitivities on staggered vs. same layer completions indicate that there is no significant difference in expected ultimate recoveries in staggered vs. same layer completions. However, there is a preferential drainage around the wellbore in both cases. Preferential drainage dominates the early production history and hence wells in lower Eagle Ford perform better than upper and middle Eagle Ford in the beginning of well life. Upper Eagle Ford wells slowly catches up in production rates ultimately reaching to same recoveries asymptotically to the lower Eagle Ford wells.

Sensitivities on fracture conductivities indicate that increasing the fracture conductivities beyond a certain point does not increase the ultimate recoveries but higher conductivity fractures give short lived high initial production. Sensitivities on pressure drawdowns indicate that the reservoir behaves as a volumetric reservoirs and drawdowns have to be tailored according to the stimulated rock volume(SRV). High drawdowns in smaller SRV's may lead to an early condensate banking in the reservoir.

References

Adeoti, L., Ayolabi, E. A., & James, P. L. (2009). An Integrated Approach to Volume of Shale Analysis: Niger Delta Example, Orire Field. *World Applied Sciences Journal*, *7*(4), 448–452.

Ajani, A. A., & Kelkar, M. G. (2012). Interference Study in Shale Plays. *SPE Hydraulic Fracturing Technology Conference*, (February), 6–8. http://doi.org/10.2118/151045-MS

Alavian, S. A., Whitson, C. H., & Martinsen, S. O. (2014). Global Component Lumping for EOS Calculations. *SPE*, (October), 27–29. http://doi.org/10.2118/170912-ms

Al-Hussainy, R., Ramey H. J., & Crawford, P. B. (1965). The Flow of Real Gases Thorugh Porous Media. *Journal of Petroleum Technology*, SPE-01243.

Andrade, J., Civan, F., Devegowda, D., & Sigal, R. (2010). Accurate Simulation of Shale-Gas Reservoirs. *Society*, (September), 19–22, SPE 135564. http://doi.org/10.2118/135564-MS

Application, P., & Shales, F. (2016). Multivariate Statistical Analysis for Resource Estimation in Unconventional.

Arps, J. J. (1944). Decline Curve Analysis.pdf. *Aime*. http://doi.org/10.2118/945228-G

Bassiouni, Z. (1994). Theory, measurement, and interpretation of well logs.

Blasingame, A. T. (1988). Review Materials: Properties of Reservoir Fluids.

Brown, M., Ozkan, E., Raghavan, R., & Retired, P. P. (2011). Practical Solutions for Pressure-Transient Responses of Fractured Horizontal Wells in Unconventional Shale Reservoirs. *Engineering*, (December), 663–676. http://doi.org/10.2118/125043-PA

Callard, J. (2015). Forecasting Reserves in the Bakken Reservoir Incorporating Flow Regime.

Chang, Y., Hammond, P., & Pop, J. (2005). When Should We Worry About Supercharging in Formation Pressure While Drilling Measurements? *Proceedings of SPE/IADC Drilling Conference*. http://doi.org/10.2118/92380-MS

Coats, K. H., Dempsey, J. R., & Henderson, J. H. (1971). The Use of Vertical Equilibrium in 2D Simulation of 3D Reservoir Performance. SPE.

Crain, E. R. (2016a). Gamma Ray. *Crain's Petrophysical Handbook*.

Crain, E. R. (2016b). Porosity Basics. *Crain's Petrophysical Handbook*.

Crain, E. R. (2016c). Shale Volume from Neutron Density Crossplot Models.

Dean, R. H., Gai, X., Stone, C. M., & Minkoff, S. E. (2006). A Comparison of Techniques for Coupling Porous Flow and Geomechanics. *SPE Journal*, *11*(1), 132–140. http://doi.org/10.2118/79709-pa

Doveton, J. H. (2001). All Models Are Wrong , but Some Models Are Useful : "Solving" the Simandoux Equation Prolog : The Archie Equation.

Dunham, R. J. (1962). Classification of carbonate rocks according to depositional texture. In *American Association of Petroleum Geologists Memoir*. *1* (pp. 108–121).

El-Banbi, A. H., & Wattenbarger, R. A. (1995). Analysis of Linear Flow in Gas Well Production. *SPE Gas Technology Symposium*, 15–18 March. http://doi.org/10.2118/39972-MS

Engineers, S. of P. (2007). Petroleum Resources Management System. *World Petroleum Council*, 1–47.

Fetkovich, M. J., Fetkovich, E. J., & Fetkovich, M. D. (1996). Useful Concepts for Decline Curve Forecasting, Reserve Estimation, and Analysis. *SPE Reservoir Engineering*, *11*(1), 13–22. http://doi.org/10.2118/28628-PA

Folladori, M. H. (2014). Sec Hot-Button Topics – Reserves Disclosures.

Freeborn, R., & Russell, B. (2012). How To Apply Stretched Exponential Equations to Reserve Evaluation. *SPE Hydrocarbon Economics and Evaluation Symposium*, (September), 24–25. http://doi.org/10.2118/162631-MS

Gaymard, R., & Poupon, A. (1968). Response of Neutron and Formation Density Logs in Hydrocarbon Bearing Formations. *Pertrophysics*, (2).

Hamada, G. M., British, T., Almajed, A. A., & Fahd, K. (2010). Uncertainly Analysis of Archie ' s Parameters Determination Techniques in Carbonate Reservoirs Calculation of Archie ' s Parameters, 1–10.

Hester, T. C. (1999). Calibration of the "Gas Effect" Using Neutron, Density, and Gamma-ray-intensity Wire-line Logs. *U.S. Geological Survey*.

Hoffmann, A. E., Crump, J. S., & Hocott, C. R. (1953). Equilibrium Constants for a Gas-Condensate System. *SPE*, *198*(219–G), 1–10.

Hurst, W. (1973). The Material Balance Equation.

Imo-jack, O. (2010). PVT Characterization of a Gas Condensate Reservoir and Investigation of factors affecting Deliverability. *SPE 140629*.

Izgec, B., & Barrufet, M. A. (2005). Performance Analysis of Compositional and Modified Black-Oil Models for a Rich Gas Condensate Reservoir. *SPE Western Regional Meeting*. http://doi.org/10.2118/93374-MS

Kanamori, H., & Anderson, D. L. (1962). Theoretical Basis of Some Empirical Relations in Seismology, *XXVII*(2), 213–220.

Lacayo, J., & Lee, J. (2014). Pressure Normalization of Production Rates Improves Forecasting Results. *Spe*, (April), 1–3.

Lee, W. J., Texas, A., & Sidle, R. E. (2010). Gas Reserves Estimation in Resource Plays. *SPE 130102*, (February), 23–25.

Liang, P., Mattar, L., & Moghadam, S. (2012). Analyzing Variable-Rate/-Pressure Data in Unconventional Gas Reservoirs, (February), 15–17.

Madrazo, A. (1960). Liquid-Density Correlation of Hydrocarbon Systems. *SPE*.

Mattar, L., & McNeil, R. (1998). The "flowing" gas material balance. *Journal of Canadian Petroleum Technology*, *37*(2), 52–55. http://doi.org/10.2118/98-02-06

McNeil, R., & Mattar, L. (1995). The "Flowing" Material Balance Procedure. *Annual Technical Meeting*. http://doi.org/10.2118/95-77

Minkoff, S. E., Stone, C. M., Arguello, J. G., Bryant, S., Eaton, J., Peszynska, M., … Steve, B. (1999). Staggered In Time Coupling of Reservoir Flow Simulation and Geomechanical Deformation: Step 1 — One-Way Coupling. *Proceedings of SPE Reservoir Simulation Symposium*, 2. http://doi.org/10.2118/51920-MS

Nobakht, M., Ambrose, R., Clarkson, C. R., Youngblood, J., & Adams, R. (2013). Effect of completion heterogeneity in a horizontal well with multiple fractures on the long-term forecast in shale-gas reservoirs. *Journal of Canadian Petroleum Technology*, *52*(6), 417–425. http://doi.org/10.2118/149400-PA

Nobakht, M., Associates, F., & Clarkson, C. R. (2012). New and Improved Methods for Performing Rate-Transient Analysis of Shale Gas Reservoirs. *Engineering*, (February), 20–22. http://doi.org/10.2118/147869-MS

Rastegar, R., Jessen, K., & California, S. (2009). A Flow Based Lumping Approach for Compositional Reservoir Simulation. *SPE 119160*, (February), 2–4.

Ri, H., Rul, U., Hoov, R., Dv, L. Q., & a, B. S. T. (2011). Desing of Multiple Transverse Fracture Horizontal Wells in Shale Gas Reservoirs. *SPE International*, (1985), 14. http://doi.org/SPE 140555

Rosepiler, M. J. (1982). Calculation and significance of water saturations in low porosity shale gas sands. Retrieved from http://www.scopus.com/inward/record.url?eid=2-s2.0-0020222211&partnerID=40&md5=8c8b1021a5b068f5891d27627001c599

Samandarli, O., Mcdonald, B., Barzola, G., Murray, M., & Resources, P. N. (2014). Understanding Shale Performance : Performance Analysis Workflow with Analytical Models in Eagle Ford Shale Play. *SPE Unconventional Resources Conference*, (1998), 1–15,SPE–169004–MS.

Saputra, I. (2008). Shale Volume Calculation, *C*(March).

Schlumberger. (2016). Techlog, Reference manual.

Schmidt, A. W., Land, G., Kilgore, C., & Yunker, J. D. (1971). Applications of the Coriband Technique to Complex Lithologies. *SPWLA 12th Annual Symposium*.

Settari, a., & Walters, D. (2001). Advances in Coupled Geomechanical and Reservoir Modeling With Applications to Reservoir Compaction. *SPE Journal*, *6*(3), 14–17. http://doi.org/10.2118/74142-PA

Sierra, L., & Mayerhofer, M. (2014). Evaluating the Benefits of Zipper Fracs in

Unconventional Reservoirs. *SPE Unconventional Resources Conference*, (April), 1–3. http://doi.org/10.2118/168977-MS

Sondhi, N. (2013). Petrophysical Characterization of Eagle Ford Shale. *Journal of Chemical Information and Modeling*, *53*(9), 1689–1699. http://doi.org/10.1017/CBO9781107415324.004

Sone, H. (2012). Mechanical properties of shale gas reservoir rocks and its relation to the in-situ stress variation observed in shale gas reservoirs. *Vasa*, *128*(March), 1–247. http://doi.org/10.1017/CBO9781107415324.004

Stalgorova, E., & Mattar, L. (2012). Analytical Model for History Matching and Forecasting Production in Multifrac Composite Systems. *SPE Canadian Unconventional Resources*. Retrieved from https://www.onepetro.org/conference-paper/SPE-162516-MS

Stalgorova, E., & Mattar, L. (2013). Analytical Model for Unconventional Multifractured Composite Systems, (August).

Suliman, B., Meek, R., Hull, R., Bello, H., Portis, D., & Richmond, P. (2013). Variable Stimulated Reservoir Volume (SRV) Simulation: Eagle Ford Shale Case Study. *Spe 164546*, 13. http://doi.org/10.2118/164546-MS

Wattenbarger, Robert A; El-Banbi, Ahmed H; Villegas, Mauricio E; Maggard, J. B. (1998). Production Analysis of Linear flow Into Fractured Tight Gas Wells. *SPE Rocky Mountain Regional/Low-Permeability Reservoirs Symposium and Exhibition*. http://doi.org/10.2118/39931-MS

Whitson, C. H. (1983). Characterizing Hydrocarbon Plus Fractions. *Society of Petroleum Engineers Journal*, *23*(4), 683–694. http://doi.org/http://dx.doi.org/10.2118/12233-PA

Whitson, C. H., & Brulé, M. R. (2000). Heptane-Plus Characterization. In *Phase Behavior* (p. 233).

Workman, S. J. (2013). *Integrating depositional facies and sequence stratigraphy in characterizing unconventional reservoirs in the Cretaceous (Cenomanian-Turonian) Eagle Ford Shale, South Texas*. *GCAGS Transactions*.

Zeng, Z., & Grigg, R. (2006). A criterion for non-darcy flow in porous media. *Transport in Porous Media*, *63*(1), 57–69. http://doi.org/10.1111/j.1439-0523.2006.01169.x

Zhang, X., Holland, M., van der Zee, W., & Moos, D. (2014). Microseismic Estimates of Stimulated Rock Volume Using a Detection-Range Bias Correction: Theory and Case Study. *SPE Hydraulic Fracturing*. SPE 168580.

Appendix A: Black Oil Vs. Compositional Model

From section 3.5 it is clear that the effort required in compositional modeling is way higher than that in a black oil model. Black oil model in general is an oversimplified case of compositional model in which all phases are lumped into two phases: pseudo oil and pseudo gas.

The constitutive equations for the simulator are then simplified to 2 phase only instead of multiple phases. This oversimplification however takes away many properties which are critical for in-depth insights into the reservoir. Hence, a decision is made between these two methods based on the requirement and purpose of simulation.

To justify the effort put in the compositional model a comparative analysis of the black oil tables from the same composition and the equation of state model are compared. Results from the black oil model are summarized from figure A1 to figure A10. Standing-katz (Madrazo, 1960) correlation is used to predict the oil density.

It can be seen from the figure A1 the gas oil ratio (GOR) above dew point pressure is 4700 scf/ bbl and the GOR predicted from compositional model is ~ 5000 scf/bbl. Oil formation volume factor (figure A2) shows a sharp decline below dew point pressure. Oil viscosity shows a sharp change at 1200 psi (figure A3) which is not physical and can adverse effects on condensate blockage around the wellbore.

Oil density predicted by Standing-Katz does not match the oil densities measured from the PVT experiments (Madrazo, 1960). As there is no volume shift, these densities cannot be regressed without changing other parameters. On the other hand, volume shift allows to match the oil densities without having any effect on other parameters.

There are no insights available on the liquid dropout curves from the gas properties predicted by black oil model (Figure A6-A10) and the gas Z factor is also different from the experimental values. Condensate gas ratio for above and below dew point is replicated fairly and a history decent match can be obtained possibly on the fluid rates.

Also, there is no insights available on component wise production i.e. percentage of lighter fraction versus percentage of heavier fraction in production stream in black oil model. But, other physical properties required to get insights in reservoir depletion are not replicated and hence a compositional model is used for simulation studies in this thesis.

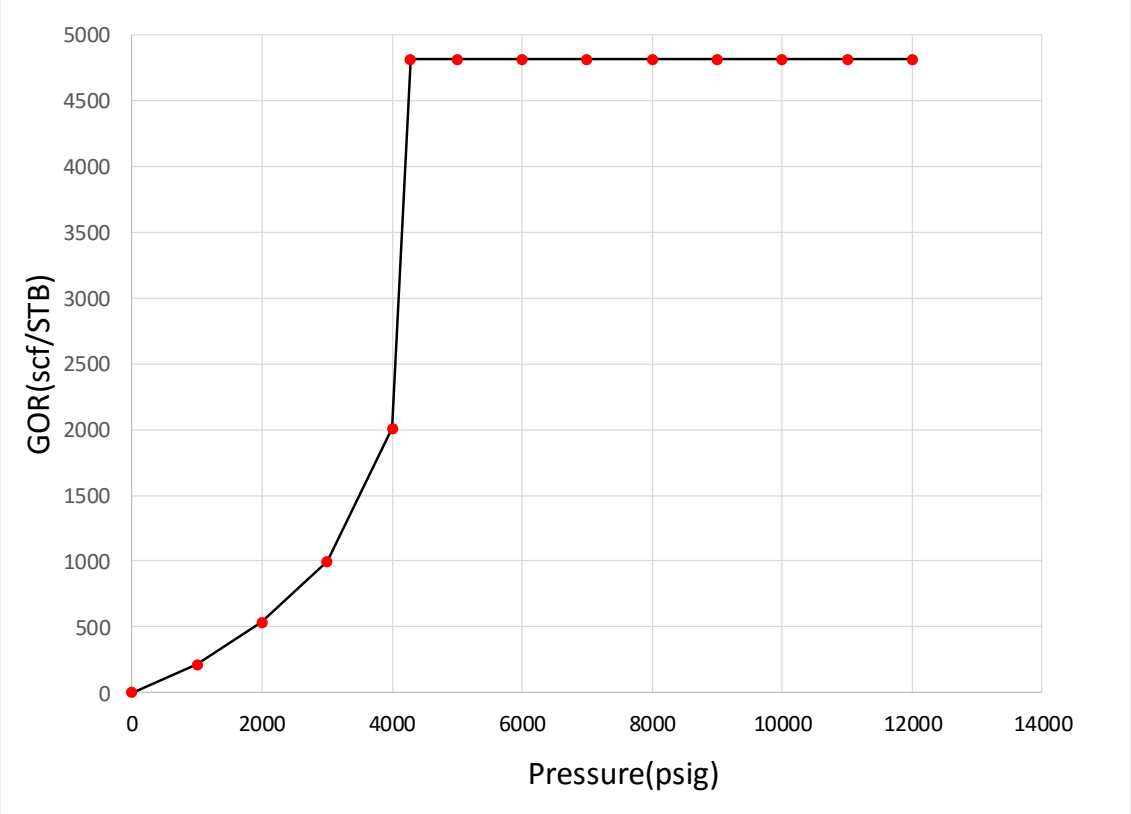

Figure A1. Gas oil ratio(GOR) trend below and above bubble point pressure. GOR trends are honored from black oil model.

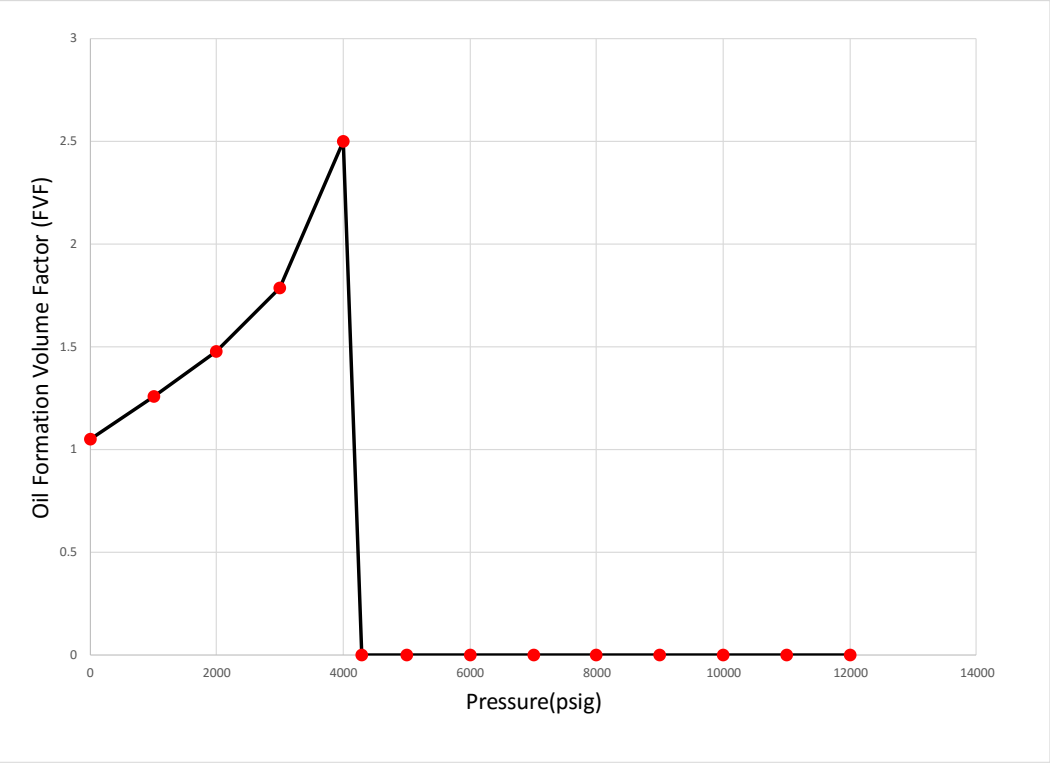

Figure A2. Oil Formation volume factor(FVF). Oil FVF trends are honored but absolute values differ.

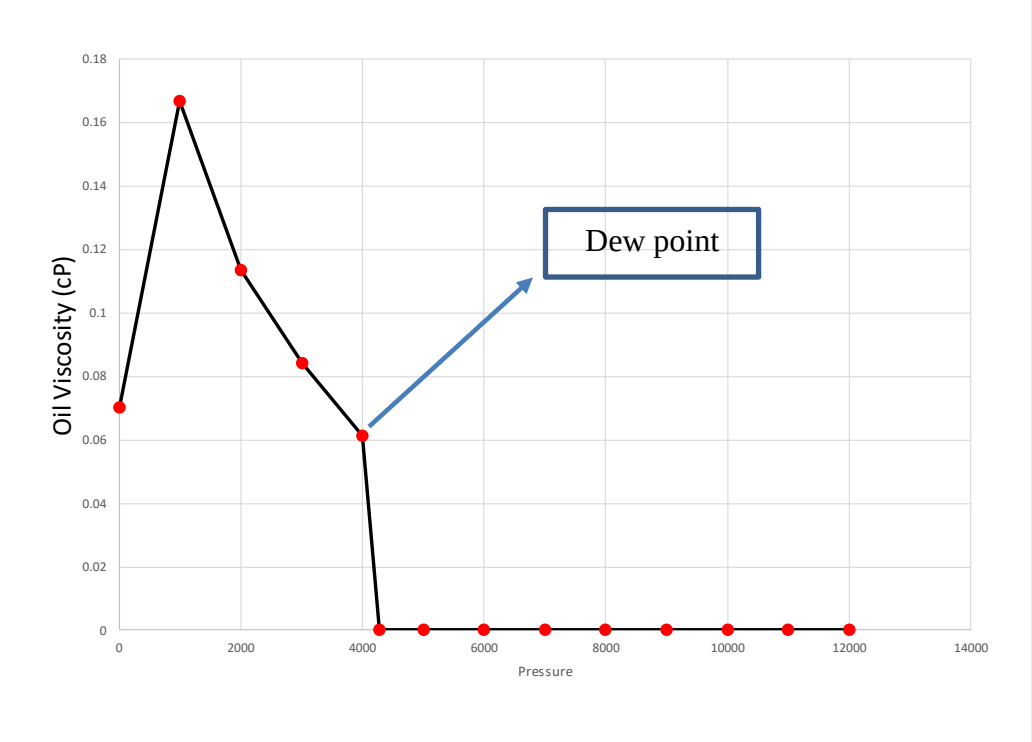

Figure A3. Oil viscosity trend with pressure. Oil viscosity shows sharp change which is not physical.

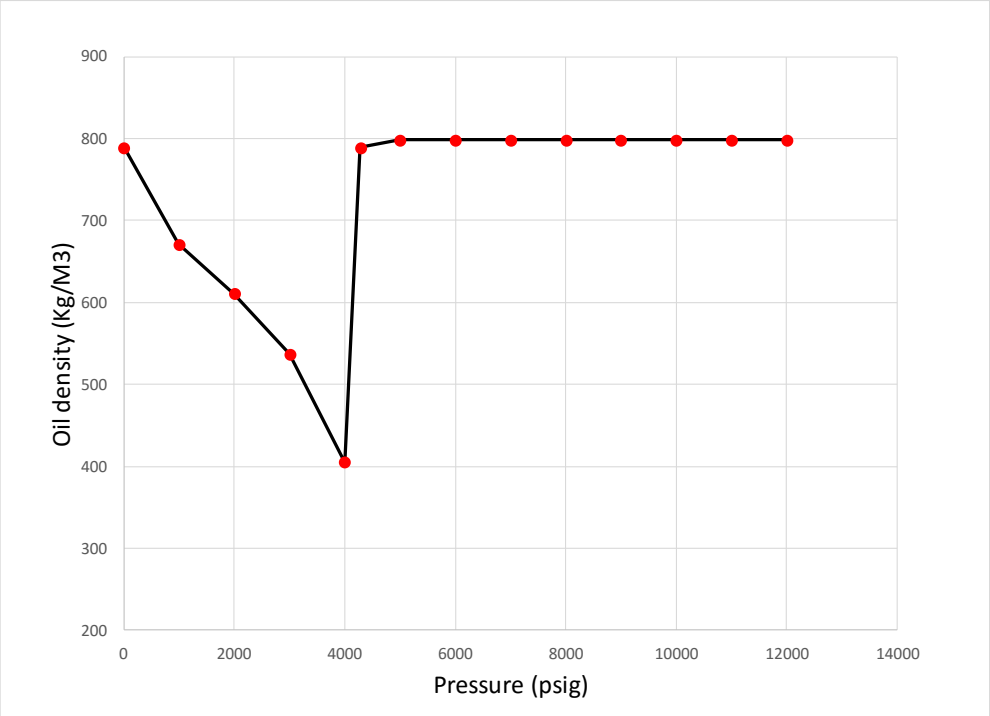

Figure A4. Oil density with pressure. Oil density trends are replicated but absolute values of oil viscosity measured from PVT experiments do not match. Oil densities cannot be matched in isolation in black oil model but same can be achieved in compositional model with the help of volume shift factor.

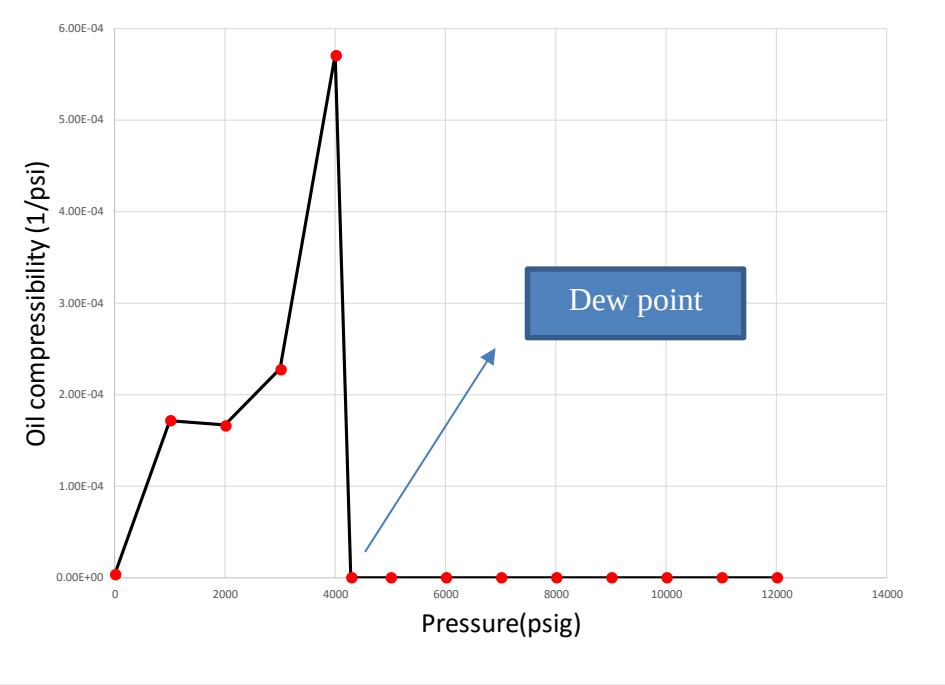

Figure A5. Oil compressibility with pressure. Oil compressibility shows sharp changes with pressure and trend is not truly replicated and not physical.

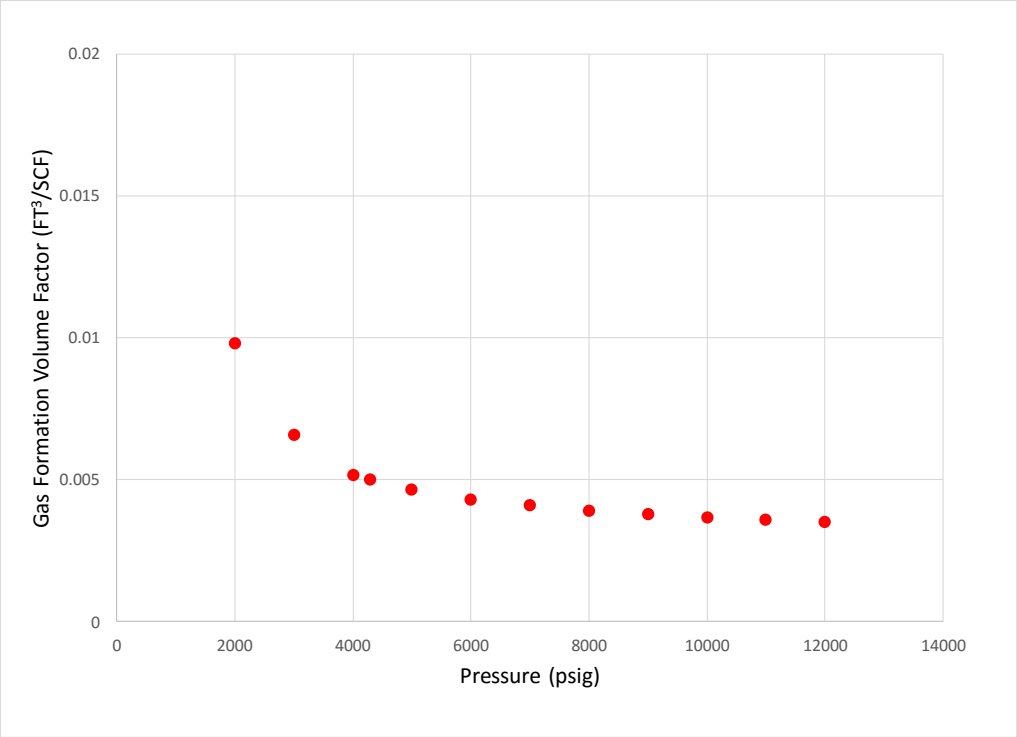

Figure A6. Gas formation volume factor (FVF). Gas FVF trend matches closely with the experimental values and can be used from the black oil model as well.

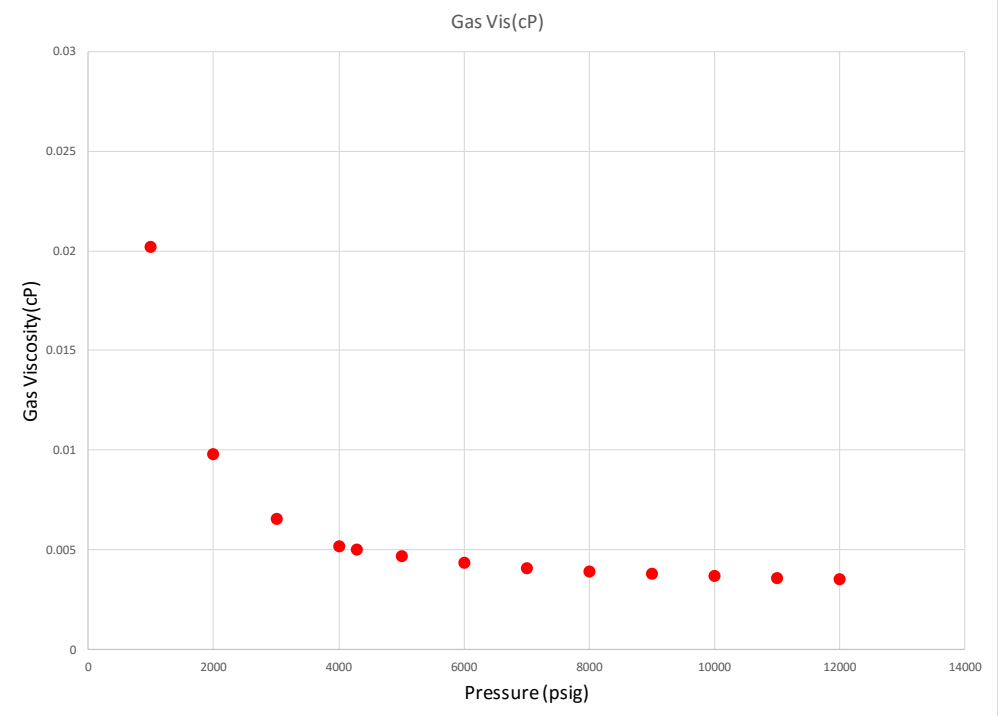

Figure A7. Gas viscosity with pressure. Gas viscosity trends are honored in black oil model but absolute values from equation of state model are different. This can be tuned further from choosing a different correlation for gas viscosity.

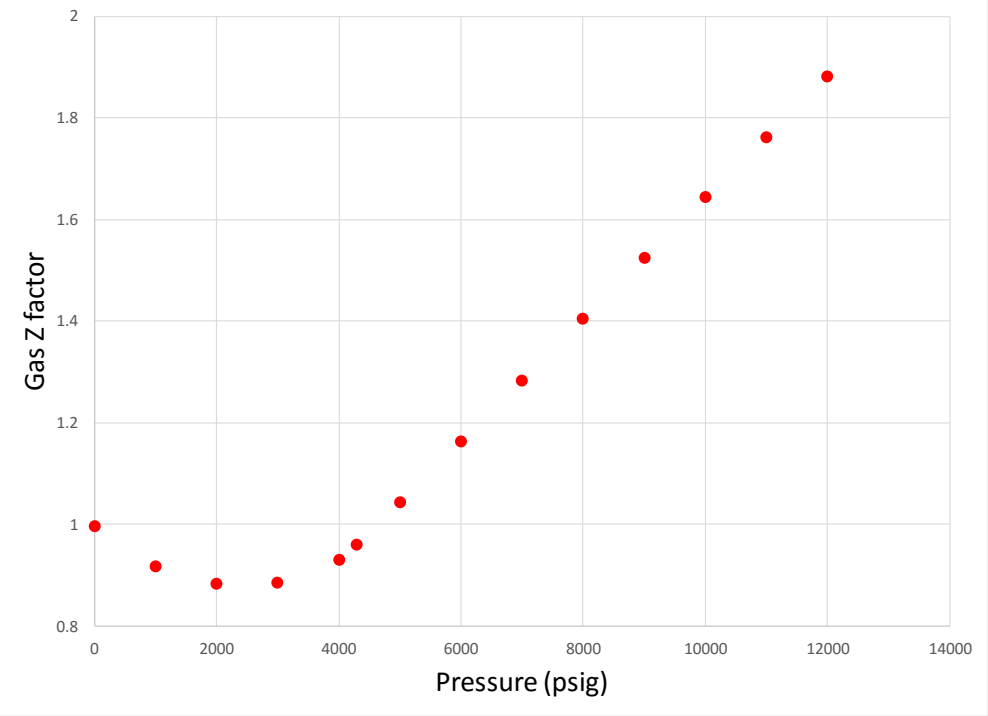

Figure A8. Gas Z factor trend with pressure. Z factor trend is honored but the absolute values of gas Z factor are different from the experimental values.

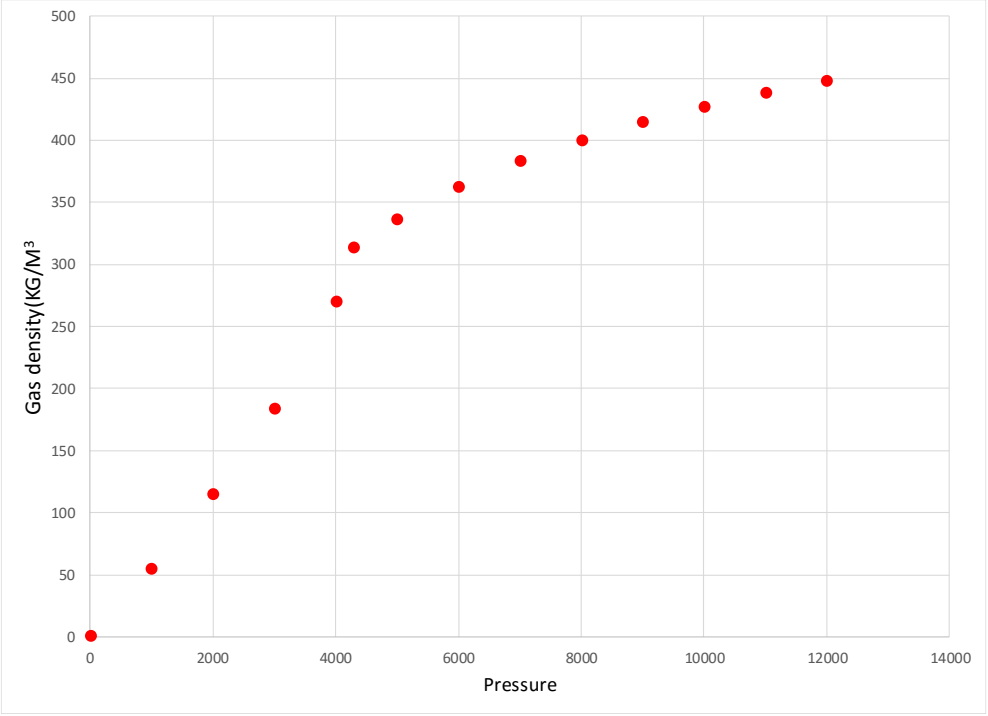

Figure A9. Gas Density with pressure. Density trend matches grossly with the equation of state (EOS) model but the absolute values do not match.

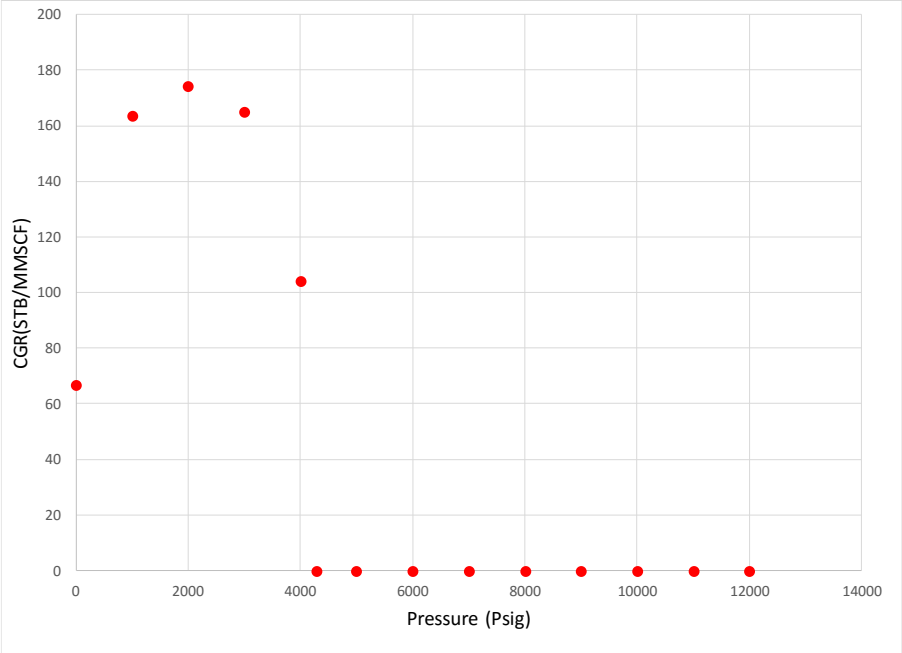

(a)

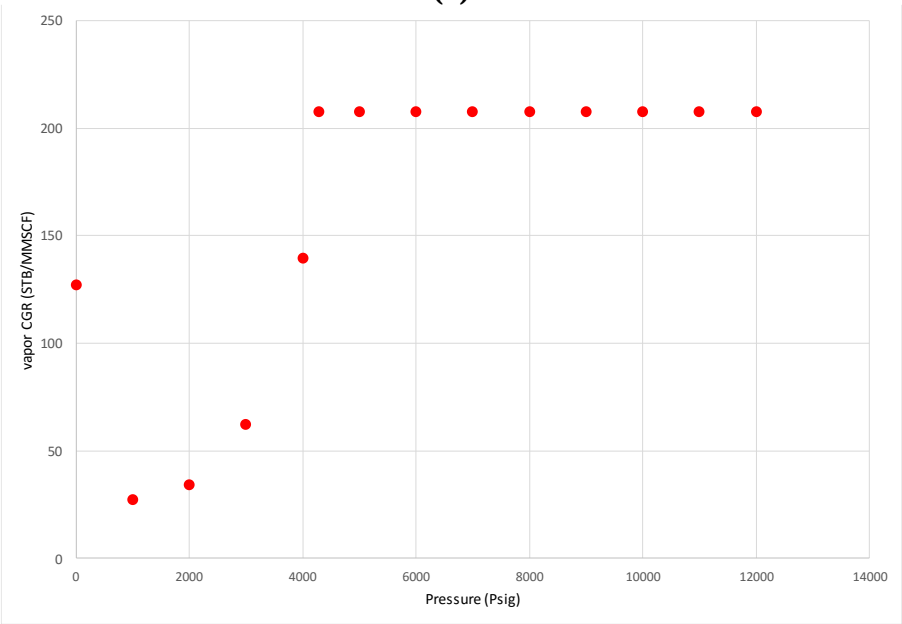

(b)

Figure A10. Condensate gas ratio with pressure. (a) vapor trend above the dew point and (b) is the trend below the dew point. The trends match closely with equation of state (EOS) model.

Appendix B: Surface to Bottomhole Pressures

For the history matching procedure during the simulation a match is obtained on surface production rates and bottomhole pressure. A robust equation of state (EOS) model ensures that the phase conversion from bottomhole to surface are honored however same cannot be said for the pressures.

Daily flowing tubing head pressures(FTHP) is available from daily production report but the surface pressures have to be converted into bottomhole pressures. To convert the surface pressures to bottomhole pressure a comparison is made between different correlations (figure B1).

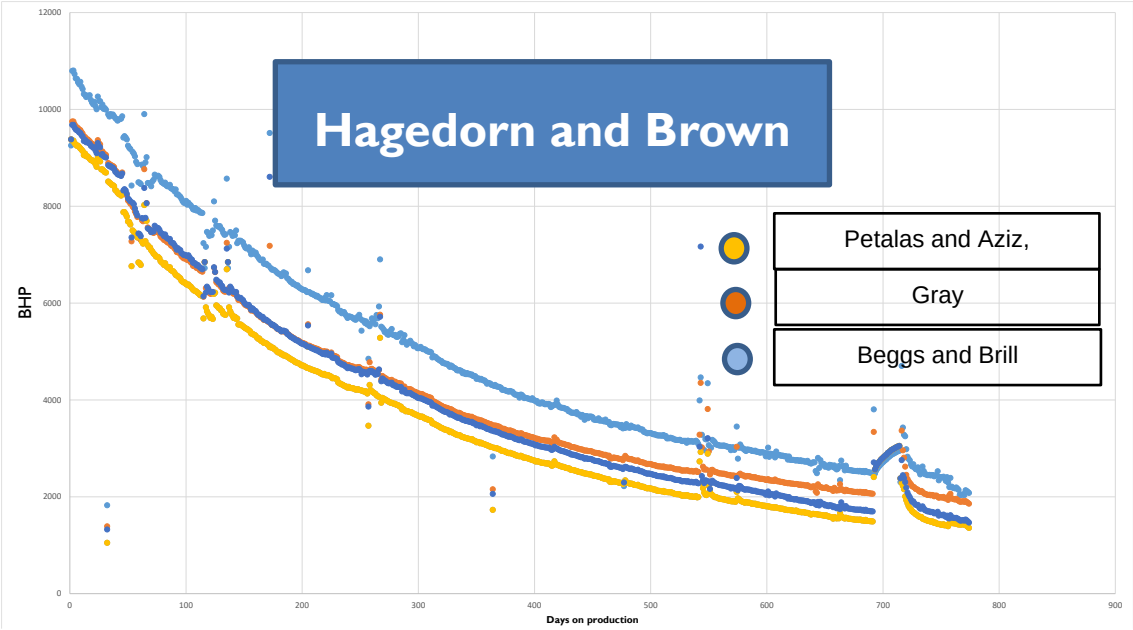

Figure B1. Surface pressure to bottomhole pressure correlation. On the Y axis is the bottomhole pressure calculated from surface pressure in psia and on the X axis is the days on production. It can be observed that except Beggs and Brill correlation all other methods produce similar results. Hagedorn and Brown is used in this thesis as it is more suitable for multiphase flow.

It can be observed from figure B1 that except Beggs and Brill, any other correlation yields the similar results. A detailed account of wellbore jeweler i.e. casing and tubing sizes, choke size etc. is not presented in this thesis due to data confidentiality.

As the fluid in the reservoir is a retrograde condensate, multiphase flow is expected in the wellbore for majority of the well life. Hence, in this thesis correlation Hagedorn and Brown is used which is considered as most accurate for calculating pressure drops in a two phase flow (Blasingame, 1988).